Università degli Studi di Pisa

Facoltà di Scienze M.F.N.

Measurement of $\mathcal{B}(\tau \to l\gamma\nu\bar{\nu},\ l = e, \mu)$ at *BaBar*

Dissertazione di Dottorato in Fisica - XXIII ciclo

Candidato:
Dr. Benjamin Oberhof

Relatore:
Prof. M. Giorgi, Dr. A. Lusiani

Coordinatore:
Prof. Kenichi Konishi

Contents

Introduction **1**

1 Radiative Leptonic τ decays in the Standard Model **3**

1.1 The effective lagrangian 3
1.2 The matrix element 4
1.3 The decay rate 5
1.4 Weak corrections 5
1.5 Radiative corrections 6
1.6 Integration and final result 8
1.7 The anomalous magnetic moment of the τ 12

2 The *BABAR* Experiment at SLAC **15**

2.1 The PeP-II e^+e^- Collider 15
2.1.1 Beam Parameters Measurements 17
2.1.2 PeP-II performances 18
2.2 The *BABAR* Detector 19
2.3 The Silicon Vertex Tracker 21
2.4 The Drift Chamber 26
2.5 Detector of internally reflected Čherenkov radiation 30
2.6 Electromagnetic Calorimeter 34
2.7 Instrumented Flux Return 38
2.8 The *BABAR* Trigger System 42

3 Event Preselection and Particle Identification **45**

3.1 Analysis Overview 45
3.2 Data and MC Samples 45
3.3 Charged Track Reconstruction 49
3.4 Photon Reconstruction 50
3.5 $e^+e^- \to \tau^+\tau^-$ Candidates 51
3.5.1 Trigger and Background Filters 51
3.5.2 Topology 52
3.6 Particle Identification 54
3.6.1 Electron Identification 54
3.6.2 Muon Identification 56
3.6.3 PID Tweaking 60
3.7 Event Reconstruction 61

3.8 MC Correction 65

4 Selection and Background Estimation **70**
4.1 Optimization strategy 70
4.2 Selection of $\tau \to \mu\gamma\nu\bar{\nu}$ 72
4.2.1 Kinematics and backgrounds 72
4.2.2 Selection 72
4.3 Selection of $\tau \to e\gamma\nu\bar{\nu}$ 76
4.3.1 Kinematics and backgrounds 76
4.3.2 Selection 77
4.4 Standard Figure of Merit 82
4.5 Energy cut-off and efficiency correction 82

5 Systematic Errors and Cross Checks **85**
5.1 Signal efficiency 85
5.2 Background estimation 88
5.3 Luminosity and cross section 90
5.4 Summary 91

6 Results **92**
6.1 The branching fractions for $\tau \to l\gamma\nu\bar{\nu}$ 92
6.2 Cross Checks 96
6.2.1 $\tau \to \mu\gamma\nu\bar{\nu}$ 96
6.2.2 $\tau \to e\gamma\nu\bar{\nu}$ 99
6.3 The anomalous magnetic moment of the τ 103

Conclusion **105**

A Analytic expression of the branching fraction **107**

B The anomalous magnetic moment of the τ lepton **110**
B.1 The anomalous magnetic moment 110
B.2 a_τ in the Standard Model 111
B.2.1 QED contribution 111
B.2.2 Electroweak contribution 113
B.2.3 QCD 113
B.2.4 Summary 113

C Radiation zeros in $\tau \to l\gamma\nu\bar{\nu}$ decays **115**

Introduction

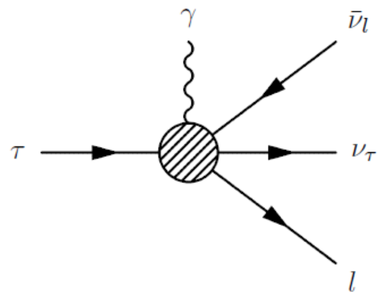

Figure 1: Radiative τ decay into a charged lepton.

The Standard Model (SM) of particle physics has been extensively tested at particle accelerators in the last decades and almost all present experimental observations are consistent with SM expectations at the current level of precision. There is however a large number of rare processes which are largely unexplored and which represent an interesting opportunity to test the electro-weak (EW) theory at loop level and search for new physics (NP) effects. τ physics, in particular, thanks to the high statistics recorded in the last 15 years by the B-factories offer an clean and interesting environment to study SM interactions at next-to-leading orders.

Leptonic radiative τ decays, in particular, are poorly known experimentally; up to date the branching fraction of the $\tau \to \mu\gamma\nu\nu$ decay has been measured by the CLEO and OPAL collaborations [1]-[2] with a total relative uncertainty of about 10% on both channels for the most precise measurement, while the branching fraction for $\tau \to e\gamma\nu\nu$ has been measured only once with a total error of the same magnitude. The measured values are reported in table . The most recent measurement by CLEO has been performed with an integrated luminosity about 2 orders of magnitude lower of that recorded by *BABAR* and, consequently, a new precision measurement is at our reach. Besides the interest for a precise determination of the branching fractions these decays have been studied since a long time because the phase space distribution of their decay products is sensitive to the Lorentz structure of the τ decay vertex. Furthermore, some recent theoretical work [3], points out that, with the high statistics recorded by B-factories one could be sensitive to the the anomalous magnetic moment of the τ which represents a very important test for the standard model and which experimental precision is currently more than 3 orders of magnitude worse than the theoretical value.

In chapter 1 we will review the calculation of the branching fraction (BF) in the SM at leading order (LO) and then, following [5], we will show how to include higher order (HO)

	$\tau \to \mu\gamma\nu\nu$	$\tau \to e\gamma\nu\nu$	Luminosity (fb^{-}1)
CLEO*	$(3.61 \pm 0.16 \pm 0.35) \cdot 10^{-3}$	$(1.75 \pm 0.06 \pm 0.17) \cdot 10^{-2}$	4.68 fb^{-1}
OPAL**	$(3.0 \pm 0.4 \pm 0.5) \cdot 10^{-3}$	–	130 pb^{-1}

Table 1: Experimental status for the determination of the branching fractions of radiative leptonic τ decays. The first quoted error is statistical while the second is systematic. *The CLEO collaboration considers a 10 MeV lower cut-off on the photon energy in the τ rest frame. **The OPAL collaboration considers a 20 MeV in the same reference frame.

radiative corrections. Later we will show how one can infer on the anomalous magnetic moment of the τ lepton from the measurement of the differential decay rate of $\tau \to l\gamma\nu\bar{\nu}$ decays. Chapter 2 contains a description of the B-factory PEP-II and the *BABAR* detector. In chapter 3 we will show how charged and neutral candidates are reconstructed in the *BABAR* detector, how charged candidates are associated to physical particles and how to define a suitable data sample for our analysis. In chapter 4 we show how the signal candidates are selected and evaluate the background contribution to the final sample, while in chapter 5 we will analyze the systematic contributions to our result. The results of the analysis are finally shown in chapter 6 along with some cross-check and hypothesis tests.

Chapter 1

Radiative Leptonic τ decays in the Standard Model

In this section, we will first show the result for the τ leptonic radiative decay rate in the Standard Model (SM) at tree level and then we will show how the effect of next-to-leading order (NLO) QED radiative corrections can be included in the calculation. Later we will show how one can infer on the anomalous magnetic moment of the τ lepton using the effective lagrangian approach.

1.1 The effective lagrangian

The Feynman diagram for the radiative decay of a τ in an electron or muon is given in figure 1.1.

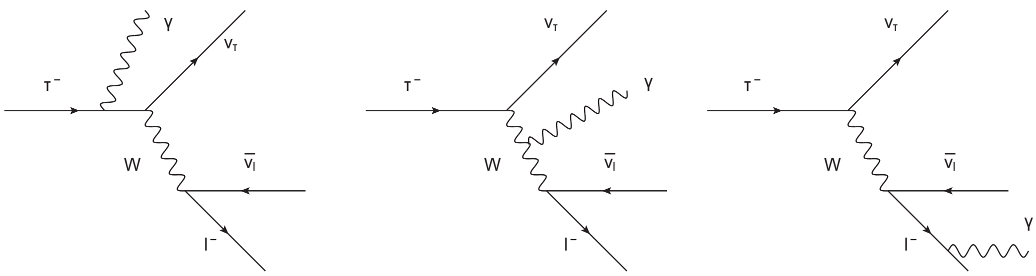

Figure 1.1: Standard model amplitude for $\tau \to l\nu\bar{\nu}\gamma$ in the unitary gauge.

To compute the decay rate at LO in electroweak (EW) theory we can use an effective lagrangian which is given by the sum of a Fermi effective coupling term to which we add the QED lagrangian

$$\mathcal{L} = \mathcal{L}_{Fermi} + \mathcal{L}_{QED} \tag{1.1}$$

since the center of mass energy m_τ is much lower than the weak scale M_W. The QED part of the lagrangian, in the Feynman gauge, is given by

$$\mathcal{L}_{QED} = -\frac{1}{4}F_{\mu\nu}F^{\mu\nu} - \frac{1}{2}(\partial_\mu A^\mu)^2 + \bar{\tau}(i\partial - m_\tau)\tau + \bar{l}(i\partial - m_l)l - e\bar{\tau}\gamma^\mu\tau A_\mu - e\bar{l}\gamma^\mu l A_\mu \tag{1.2}$$

while the Fermi part can be written, as usual, as

$$\mathcal{L}_{Fermi} = -\frac{G_F}{\sqrt{2}}[\bar{\nu}_\tau \gamma^\mu (1-\gamma^5)\tau \cdot \bar{l}\gamma_\mu (1-\gamma^5)\nu_l] \tag{1.3}$$

where G_F is the Fermi constant $G_F = 1.6637(1) \cdot 10^{-5}\mathrm{GeV}^2$. The Fermi constant G_F is defined from the muon lifetime [15] as

$$\frac{1}{\tau_\mu} = \frac{G_F^2 m_\mu^5}{192\pi^3} f(\frac{m_e^2}{m_\mu^2})(1+\delta_{mu}) \tag{1.4}$$

where $f(x) = 1 - 8x - 12x^2 \ln x + 8x^3 - x^4$ is a phase-space factor and $C(m_e)$ accounts for higher order QED corrections.

1.2 The matrix element

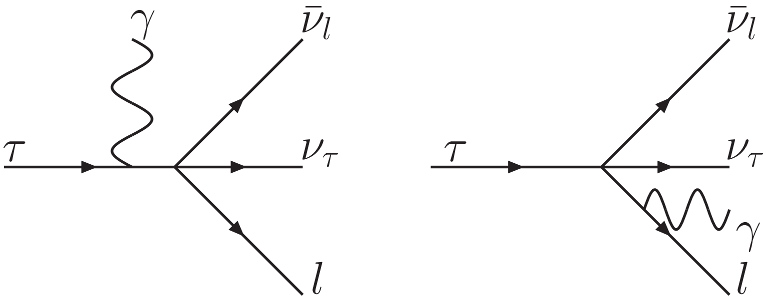

Figure 1.2: The two Feynman diagrams contributing to the radiative leptonic τ decay in the effective lagrangian approach defined by equation 1.1.

From the lagrangian of the previous section one can write the amplitude for Fermi the decay as

$$-\frac{G_F}{\sqrt{2}}\bar{u}_{\nu_\tau}[\gamma^\mu(1-\gamma^5)]u_\tau \bar{u}_l[\gamma^\mu(1-\gamma^5)]v_{\nu_l} \tag{1.5}$$

interchanging the τ and $\bar{\nu}_l$ spinors, this becomes

$$+\frac{G_F}{\sqrt{2}}\bar{u}_{\nu_\tau}[\gamma^\mu(1-\gamma^5)]v_{\nu_l} \bar{u}_l[\gamma^\mu(1-\gamma^5)]u_\tau. \tag{1.6}$$

In this way we separated the charged and neutral lepton parts, simplifying later calculations. Now, using Feynman rules we can include the outgoing photon and compute the matrix element $i\mathcal{M} = i\mathcal{M}_1 + i\mathcal{M}_2$ which corresponds to the two graphs in fig 1.2 (a) and (b) respectively

$$\mathcal{M}_1 = \frac{G_F}{\sqrt{2}}\bar{u}_{\nu_\tau}[\gamma^\mu(1-\gamma^5)]v_{\nu_l}\bar{u}_l[\gamma^\mu(1-\gamma^5)\frac{p_1 - k + m_\tau}{(p_1-k)^2 - m_\tau^2}(-ie\gamma^\rho)]u_\tau \epsilon_\rho^\dagger(k) \tag{1.7}$$

and

$$\mathcal{M}_2 = \frac{G_F}{\sqrt{2}}\bar{u}_{\nu_\tau}[\gamma^\mu(1-\gamma^5)]v_{\nu_l}\bar{u}_l[\frac{p_2 - k + m_\tau}{(p_2-k)^2 - m_\tau^2}(-ie\gamma^\rho)\gamma^\mu(1-\gamma^5)]u_\tau \epsilon_\rho^\dagger(k). \tag{1.8}$$

1.3 The decay rate

Using the amplitude given in the previous section, the SM leading-order (LO) prediction for the differential decay rate of $\tau \to l\nu\bar{\nu}\gamma$ for a polarized τ, in the τ rest frame, can be written as [5]

$$\begin{aligned}\frac{d^6_{LO}}{dxdyd\Omega_l d\Omega_\gamma} =& \frac{\alpha G_F^2 m_\tau^5}{(4\pi)^6} \\ & x\beta[G_{LO}(x,y,c) + x\beta\hat{n}\cdot\hat{p}_l J_{LO}(x,y,c) + y\hat{n}\cdot\hat{p}_\gamma K_{LO}(x,y,c)]\end{aligned} \tag{1.9}$$

where $G_F = 1.1663787(6)\cdot 10^{-5}$ GeV^2 is the Fermi coupling constant, m_τ, m_μ, m_e are the τ, μ and electron masses respectively and $\alpha = 1/137.035999174(35)$ is the fine-structure constant. Also $x = E_l/m_\tau$, $y = 2E_\gamma/m_\tau$ and $\beta = |\vec{p_l}|/E_l$, where E_l, p_l and E_γ, p_γ are the energies and momenta of lepton and photon. The final charged lepton and photon are emitted at solid angles Ω_l and Ω_γ with respect to the τ polarization $\hat{n}$, respectively, with momenta p_l and p_γ, and $c = \cos\theta$ is the cosine of the angle between p_l and p_γ. The formula for the radiative decay of a polarized τ^+ can be obtained by inverting the signs in front of the scalar products $\hat{n}\cdot\hat{p}_l$ and $\hat{n}\cdot\hat{p}_\gamma$. The function $G_{LO} = (4/3yz^2)g_{LO}(x,y,z)$, and analogously J_{LO} and K_{LO}, are long polynomials and are given in the appendix. Summing over the initial τ spin states and averaging over the final state lepton and photon spins, equation 1.9 simplifies to

$$\frac{d\Gamma}{dxdyd\cos\theta} = \frac{\alpha G_F^2 m_\tau^5}{2(4\pi)^6} G_0 y\sqrt{x^2-4r^2} \tag{1.10}$$

To get the total rate one has to perform the following integration over phase space

$$\Gamma = \int_{2r}^{1+r^2} dx \int_{-1}^{1} d\cos\theta \int_{y_{min}}^{y_{max}(x,\theta)} dy \frac{d\Gamma}{dxdyd\cos\theta} \tag{1.11}$$

numerical integration has been used in [4] to calculate $\Gamma(\tau \to l\gamma\nu\bar{\nu})/\Gamma_{tot}$, the results, shown in table 1.3 are in agreement with the PDG values in [15].

	Theory	PDG
$\tau \to \mu\gamma\nu\bar{\nu}$	0.36	0.36 ± 0.04
$\tau \to e\gamma\nu\bar{\nu}$	1.84	1.75 ± 0.18

Table 1.1: The branching fraction, as obtained from equation 1.10 compared to the value currently reported by the Particle Data Group (PDG) [15].

1.4 Weak corrections

In our effective lagrangian approach we have neglected the contribution corresponding to the emission of a real photon from the intermediate vector boson as well as the propagator correction due to the finite mass of W boson. Including this further contributions the differential decay rate becomes

$$\frac{d^6_{LO}}{dxdyd\Omega_l d\Omega_\gamma} = \frac{\alpha G_F^2 m_\tau^5}{(4\pi)^6} \frac{x\beta}{1+\delta W(m_\mu, m_e)}[G(x,y,c) + x\beta\hat{n}\cdot\hat{p}_l J(x,y,c) + y\hat{n}\cdot\hat{p}_\gamma K(x,y,c)] \tag{1.12}$$

$\delta W(m_\mu, m_e)$ is the tree-level correction induced by the W propagator [9]

$$\delta W(M,m) = \frac{3}{5} r_W^2 \frac{(1-r^2)^5}{F(r^2)} + \mathcal{O}(r_W^4) \tag{1.13}$$

with $r_W = m_\tau/M_W$, $r = m_l/m_\tau$ and

$$F(t) = 1 - 8t + 8t^3 - t^4 - 12t^2 \ln t. \tag{1.14}$$

and

$$G(x,y,c) = \frac{4}{3yz^2}[g_{LO}(x,y,z) + r_W^2 g_W(x,y,z) + \mathcal{O}(r_W^4)] \tag{1.15}$$

where $z = xy(1-c\beta)/2$. The leading contribution to $\delta W(M,m)$ is independent of the flavor of the final state lepton and is given by $(3/5)(m_\tau/M_W)^2 \simeq 3\times 10^{-4}$. The functions g_{LO}, j_{LO}, and k_{LO}, arise from the pure Fermi V-A interaction, whereas g_W, j_W, and k_W are the contributions for the emission of a photon from the W-boson.

1.5 Radiative corrections

As shown by Sirlin [10], to leading order in G_F but to all orders in α, the radiative corrections to muon decay are finite in the Fermi V-A theory. Since this special feature holds also for taus decaying into leptons, all NLO corrections to the radiative τ decay can be calculated in the Fermi theory, i.e. collapsing the weak decay, mediated by the W-boson, to an effective four-fermion interaction. This is sufficient for the desired level of precision: pure EW NLO corrections are expected to be of $\mathcal{O}(\alpha m_\tau^2/M_W^2)$, which are subleading with respect to two-loop QED corrections of $\mathcal{O}(\alpha^2)$. NLO corrections originate either by real photon emission and one-loop virtual corrections.

Since this contributions will be calculated in the Fermi theory in which the weak decay mediated by the W boson is collapsed to a four fermion effective coupling, a virtual photon can be exchanged only between charged fermions as shown in fig. 1.3.

The different contributions can briefly further subdivided in 4 classes of diagrams involving virtual photons (fig. 1.3):

- QED-vertex corrections (Fig. 1.3(A)), which are ultraviolet divergent(UV)
- fermion self-energies (Fig. 1.3(C)), UV divergent,
- weak-vertex correction (Fig. 1.3(B)), UV divergent,

- boxes (Fig. 1.3(D)), UV finite but infrared divergent (IR).

diagrams involving real photons

- bremsstrahlung diagrams, UV finite but IR divegent (Fig. 1.4)

and

- couterterm diagrams

to assure renormalization.

The calculation of the virtual diagrams proceeds dividing each amplitude into the neutrino and charged lepton sector, and isolating the loop integral. In order to regularize the UV divergences one can use dimensional regularization, so that the integration is performed in D dimensions and the result expanded around D = 4 using the parameter $\epsilon = 4 - D$. To preserve dimensions, a mass scale μ is introduced. After regularization, the loop integral are calculated by the Passarino-Veltman reduction.

The renormalization of the QED part of the Lagrangian is done in the on-shell scheme. In general, the Fermi interaction is not renormalizable, however as was demonstrated by Berman and Sirlin that in the special case of the tau decay the mass and wave function renormalization is enough to cancel the UV divergences arising from the weak vertex corrections. After renormalization and the introduction of the counterterm diagrams, one adds the corresponding self-energy counterterm in order to cancel the UV divergence. Finally the infrared divergences (IR) arising from the diagrams with a virtual photon, cancel with those arising from the associated soft bremsstrahlung, i.e. the real double radiative decay.

At next-to-leading-order in QED the differential decay rate for $\tau \to l\nu\bar{\nu}\gamma$ can be written as

$$\begin{aligned}\frac{d^6_{LO}}{dx dy d\Omega_l d\Omega_\gamma} =& \frac{\alpha G_F^2 m_\tau^5}{(4\pi)^6}\frac{x\beta}{1+\delta W(m_\mu, m_e)} \\ & [G(x,y,c) + x\beta\hat{n}\cdot\hat{p}_l J(x,y,c) + y\hat{n}\cdot\hat{p}_\gamma K(x,y,c) + \\ & + yx\beta\hat{n}\cdot(\hat{p}_l \times \hat{p}_\gamma) L(x,y,c)]\end{aligned} \tag{1.16}$$

The function $G(x,y,c)$, and similarly J and K, this time can be written as

$$G(x,y,c) = \frac{4}{3yz^2}[g_{LO}(x,y,z) + \frac{\alpha}{\pi} g_{NLO}(x,y,z;y_{min}) + r_W^2 g_W(x,y,z)] \tag{1.17}$$

where $g_{LO}(x,y,z)$ and $g_W(x,y,z)$ are the usual tree-level contributions, already described before, and $g_{NLO}(x,y,z;y_min)$ contains both virtual and real QED corrections.

The function $L(x,y,z)$, is purely induced by loop corrections and thus is of $\mathcal{O}(\alpha/\pi)$. $L(x,y,z)$ is of the form $\sum_n P_n(x,y,z) Im[In(x,y,z)]$, where P_n are polynomials in x, y, z and $In(x,y,z)$ are scalar integrals whose imaginary part is different from zero.

1.6 Integration and final result

To get the numerical values for the branching fractions one has to integrate equation 1.16. The kinematic limits for x, c, and y are given by

$$2r \leq x \leq 1 + r^2 \tag{1.18}$$

$$-1 \leq c \leq 1 \tag{1.19}$$

$$0 < y \leq y_{max}(x, c) \tag{1.20}$$

where the maximum normalized photon energy is

$$y_{max}(x, c) = \frac{2(1 + r^2 - x)}{2 - x + cx\beta} \tag{1.21}$$

however, every experimental setup has a minimum photon energy E_{min}

$$E_{\gamma,min} = y_{min}(m_\tau/2) \tag{1.22}$$

below which photons are not detected. As the constraint $y_{min} < y_{max}(x, c)$, necessary to measure radiative decays, leads to the bound $c < c_{max}(x)$, with

$$c_{max}(x) = \frac{2(1 + r^2 - x) - (2 - x)y_{min}}{x\beta y_{min}} \tag{1.23}$$

the effective kinematic ranges of x, c, and $y > y_{min}$ are

$$2r \leq x \leq 1 + r^2 \tag{1.24}$$

$$-1 \leq c \leq min[1, c_{max}(x)] \tag{1.25}$$

$$y_{min} \leq y \leq y_{max}(x, c) \tag{1.26}$$

We note that the terms in G, J, and K proportional to r^2 cannot be neglected in the integrated decay rate. Indeed, the functions multiplying these r^2 terms generate a singular behavior in the $r \to 0$ limit after the integration over $c = cos\theta$: terms proportional to r^2/z^2 in G (or J, K) lead to a non-vanishing contribution to the integrated decay rate since

$$\int dc \frac{1}{z^2} \sim \frac{1}{z} \tag{1.27}$$

is evaluated at the integration limit $c \to 1$ where

$$z \to xy(1 - \beta)/2 \to r^2(y/x) \text{ for } x >> 2r. \tag{1.28}$$

If the initial τ is not polarized, equation 1.16 simplifies to

$$\frac{d^3}{dxdcdy} = \frac{\alpha G_F^2 m_\tau^5}{(4\pi)^6} \frac{8\pi^2 x\beta}{1 + \delta_W(m_\mu, m_e)} G(x, y, c) \tag{1.29}$$

Integrating equation 1.29 over the kinematic ranges defined before and dividing the result by the τ total width Γ_τ one obtains the branching ratios of the radiative decays for a given threshold y_{min}.

These branching ratios contain mass singularities (and $\ln y_{min}$), but their presence does not contradict the Kinoshita-Lee-Nauenberg theorem [11], which applies only to total decay rates. The branching ratio for radiative tau decays at LO, with a minimum detected photon energy $E_{min} = 10$ MeV, are reported in 1.2 and compared with current experimental values.

	Theory	Experiment
$\tau \to e\gamma\nu\nu$	1.84×10^{-2}	$(1.75 \pm 0.06 \pm 0.17) \times 10^{-2}$
$\tau \to \mu\gamma\nu\nu$	3.67×10^{-3}	$(3.61 \pm 0.16 \pm 0.35) \times 10^{-3}$

Table 1.2: Branching ratios at LO for radiative tau decays for a photon energy threshold $E_{min} = 10$ MeV. Theoretical values are taken from [5]. The experimental values were measured by the CLEO Collaboration, where the first error is statistical and the second one is systematic [1].

	$\Gamma_{\tau\to l\gamma\nu\nu,LO}/\Gamma_{tot}$	$\Delta\Gamma_{\tau\to l\gamma\nu\nu,NLO}/\Gamma_{tot}$	Ratio
$\tau \to e\gamma\nu\nu$	1.836×10^{-2}	-1.83×10^{-3}	10%
$\tau \to \mu\gamma\nu\nu$	3.67×10^{-3}	-9.1×10^{-5}	2.5%

Table 1.3: Contributions to the branching ratios given by the NLO correction $(\alpha/\pi)g_{NLO}$, and ratios to the LO.

	$\Gamma_{\tau\to l\gamma\nu\nu,LO}/\Gamma_{tot}$	$\Delta\Gamma_{\tau\to l\gamma\nu\nu,W}/\Gamma_{tot}$	Ratio
$\tau \to e\gamma\nu\nu$	1.836×10^{-2}	5.7×10^{-6}	3×10^{-4}
$\tau \to \mu\gamma\nu\nu$	3.67×10^{-3}	1.2×10^{-6}	3×10^{-4}

Table 1.4: Contributions to the branching ratios given by the W-boson $r_W^2 g_W$ and ratios to the LO.

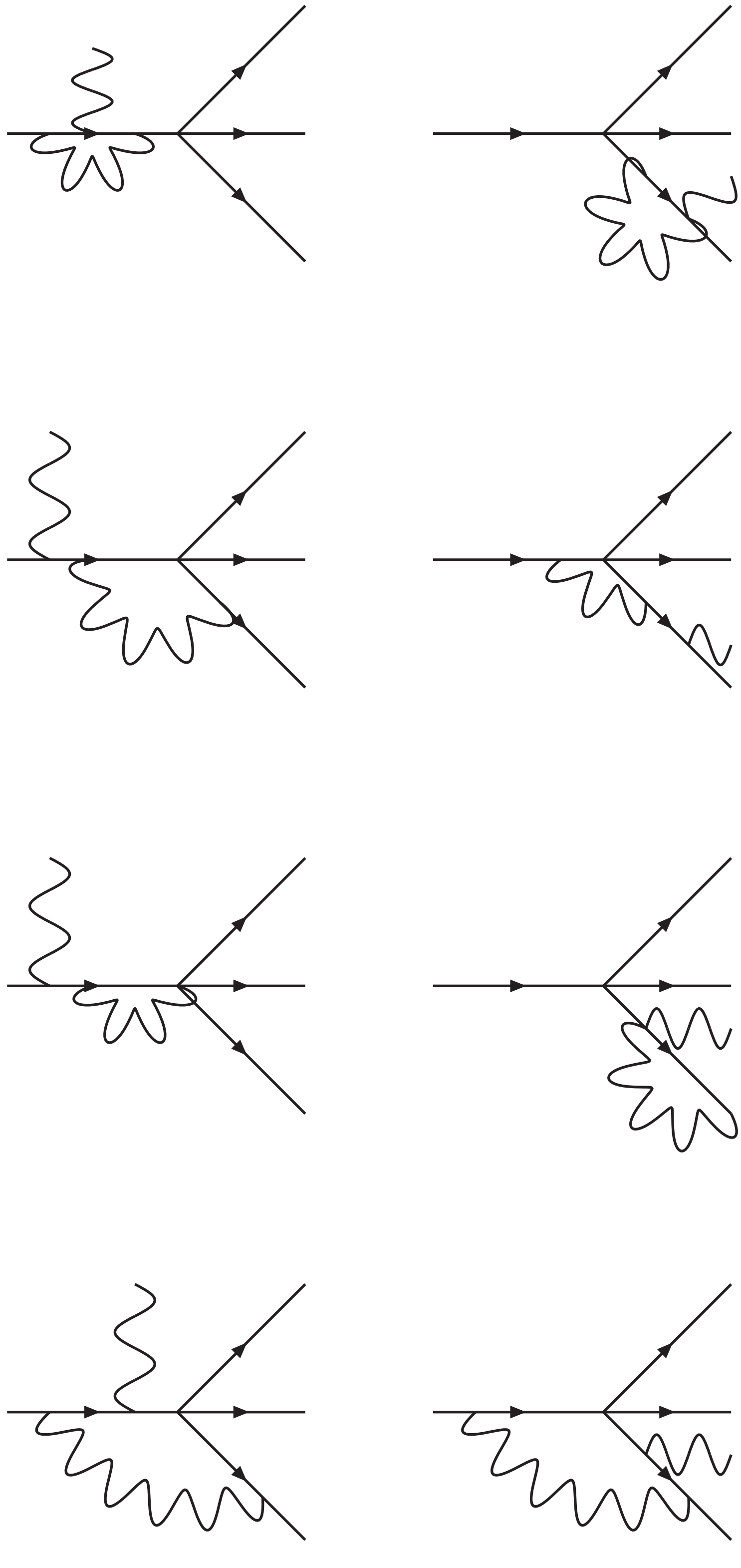

Figure 1.3: One loop QED contributions to $\tau \to l\nu\bar{\nu}\gamma$. From top to bottom, QED triangles (first row), weak triangles (second row), self-energies (third row) and boxes (fourth row).

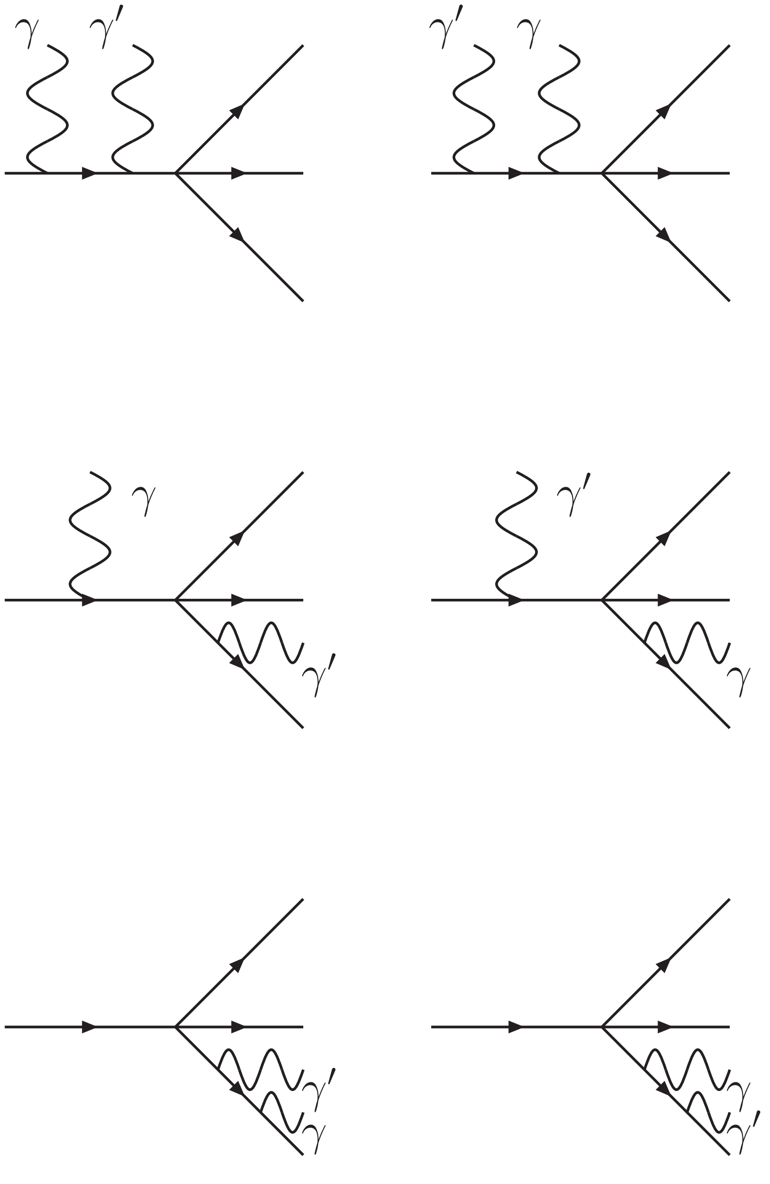

Figure 1.4: Real NLO contributions to $\tau \to l\nu\bar{\nu}\gamma$ from the emission of a second soft photon with $E^* < E^*_{min}$.

1.7 The anomalous magnetic moment of the τ

The possibility to set bounds on a_τ from radiative leptonic τ decays was suggested long time ago by [12]. The basic idea is to take advantage of the radiation zero of the differential decay rate at LO which occurs when, in the τ rest frame, the lepton and the photon are emitted back-to-back, and the lepton has maximal energy. Since a non-standard contribution to a_τ spoils this radiation zero, precise measurements of this phase-space region could be used to set bounds on its value. However, this method is only sensitive to large values of a_τ since at the radiation zero the dependence on non-standard a_τ contributions is quadratic.

An effective lagrangian approach to study τ dipole moments was first introduced by Bernreuther et al. [13]. At B-factories the energy scale $\sqrt{s} \sim m_\tau$ involved in radiative τ decays allows to study the τ dipole moments introducing, beside the SM Lagrangian $\mathcal{L}_{SM}$, two new effective terms of the form

$$\mathcal{L}_{eff} = \mathcal{L}_{SM} + c_a \frac{e}{4\Lambda} O_a - c_d \frac{i}{2\Lambda} O_d \tag{1.30}$$

where e is the electron charge, c_a and c_d are the effective couplings, Λ defines the physics scale and the operators $O_{a,d}$ are defined as

$$\begin{aligned} O_a &= \bar{\tau}\sigma_{\mu\nu}\tau F^{\mu\nu} && (1.31)\\ O_d &= \bar{\tau}\sigma_{\mu\nu}\gamma^5\tau F^{\mu\nu}. && (1.32) \end{aligned}$$

The scale Λ represents the energy where any kind of physics which is not described by $\mathcal{L}_{SM}$ generates a contribution to the τ electric or magnetic dipole moment and is therefore larger at least than the electroweak scale, i.e. $\Lambda > M_Z$. For simplicity we assume the scale Λ to be equal for both operators $O_{a,d}$, knowing that actually the scale for the EDM is much higher than that for the $g-2$. The contributions from the two effective operators $O_{a,d}$ to the electromagnetic form factors are the same for $q^2 = 0$ as for $q^2 \neq 0$.

This is due to the fact that only higher dimensional operators would give rise to a difference between these two cases, which means that such contributions are suppressed by higher powers of q^2/Λ^2 [14]. In this case, q^2 may be of the order of m_τ^2 while Λ is certainly higher than M_Z and we can safely neglect contributions from higher dimensional operators. Of course, the requirement that $q^2 << \Lambda^2$ is the fundamental hypothesis of our effective Lagrangian approach. Obviously the two operators O_a, O_d are not gauge invariant under the gauge group $\mathrm{SU}(2)_L \times \mathrm{U}(1)_Y$ but it can be shown that they can be recovered from six dimensional gauge invariant operators [14],

$$\begin{aligned} O_B &= \frac{C^{33}_{eB\phi}}{2\Lambda^2}(\bar{l}_L\sigma^{\mu\nu}\tau_R)\phi B_{\mu\nu} + h.c. && (1.33)\\ O_W &= \frac{C^{33}_{eW}}{2\Lambda^2}(\bar{l}_L\sigma^{\mu\nu}\tau_R)T^a\phi W^a_{\mu\nu} + h.c. && (1.34) \end{aligned}$$

after spontaneous symmetry breaking. Here $l = (\nu_L; \tau_L)$ is the tau leptonic doublet, ϕ is the Higgs doublet, $B_{\mu\nu}$ and $W_{\mu\nu}$ are the field strength tensors, and T^a the generators of $\mathrm{SU2})_L$. For our phenomenological study however it is simpler to adopt the effective

Lagrangian of equation 1.30. The effective Lagrangian $\mathcal{L}_{eff}$ 1.30 gives the following predictions for the tau dipole moments

$$a_\tau = \frac{\alpha}{2\pi} + c_a \frac{m_\tau}{\Lambda} + ... \quad (1.35)$$

$$d_\tau = c_d \frac{1}{\Lambda} + ... \quad (1.36)$$

where the dots indicate higher-order contributions not relevant for our discussion (note, in (1.49), that d_τ has no QED contribution). We then define the parameters

$$\tilde{a}_\tau = c_a \frac{m_\tau}{\Lambda} \quad (1.37)$$

$$\tilde{d}_\tau = = c_d \frac{1}{\Lambda} \quad (1.38)$$

To measure $\tilde{a}_\tau$ and $\tilde{d}_\tau$ with a precision of $O(10^{-3})$ it is necessary to include in the decay rate prediction for the processes the radiative corrections at next-to-leading order (NLO) in QED and the non-negligible contribution from the W-boson propagator.

The operators O_a and O_d in the effective lagrangian generate additional contributions to the differential decay rate. They can be summarized in the shift

$$G(x, y, c) \longrightarrow G(x, y, c) + Re(\tilde{a}_\tau) G_a(x, y, c) + m_\tau Im(\tilde{d}_\tau) G_d(x, y, c) \quad (1.39)$$

and similarly for J and K. Moreover, inside the squared bracket there is the comparison of an additional term

$$xy\beta \hat{p}_l \cdot (\hat{p}_\gamma \times \hat{n}) L(x, y, c) \quad (1.40)$$

All the new contributions induced by effective operators are reported in the appendix. Tiny terms of $\mathcal{O}(\tilde{a}_\tau^2)$ and $\mathcal{O}(\tilde{d}_\tau^2)$ were neglected since, by construction, sub-leading.

Taking advantage of the shift in the phase space distribution introduced by the new effective terms one could, in principle, extract $\tilde{a}_\tau$ and $\tilde{d}_\tau$ from a precise fit to the phase space distributions of the lepton-photon pair or make an integrated measurement of the branching fraction in the phase space region around the "radiation zero" as suggested by [12] et al.

Figure 1.5 shows as example the two dimensional distribution in $\cos\theta_{l\gamma}$ versus $2E_l^*/m_\tau$ for $\tau \to e\gamma\nu\bar{\nu}$ in the τ rest frame.

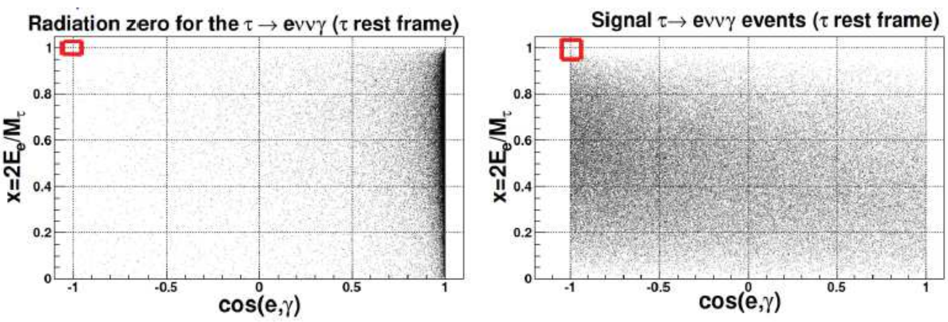

Figure 1.5: Distribution of $x = 2E_l/m_\tau$ versus $\cos\theta_{l\gamma}$ in the τ rest frame for $G(x, y, c)$ (at NLO) and $G_a(x, y, c)$ as defined in A. Figure taken from [16].

Chapter 2

The *BABAR* Experiment at SLAC

BABAR [33]is a 4π detector, operating at the interaction region of the PeP-II asymmetric e^+e^- collider [44]. The *BABAR* experiment was designed and built by a large international collaboration in order to provide the cleanest environment possible for the reconstruction and study of rare processes involving heavy flavors: the physics program consisting in the study of CP-violation in B systems, bottom and charm decays, τ physics, and search for rare processes. The detecting period for *BABAR* is now over and the detector and storage ring are going through their decommissioning and dismantling period.

In this chapter we will describe the main features and performances of PeP-II and *BABAR*.

2.1 The PeP-II e^+e^- Collider

PeP-II is an asymmetric e^+e^- collider optimized for CP-Violation studies in B sector that has stopped its operations in April 2008. It was most of the time producing events around the $\Upsilon(4S)$ resonance corresponding to a center of mass (CM) energy of $\sqrt{s} = 10.58\,\mathrm{GeV}$, in the last period of data-taking an energy scan towards lower energies has been performed studying region of the other vector resonances of the Υ system, in Fig. 2.1 the resonance system is shown.

The effective cross section for $\Upsilon(4S)$ at $\sqrt{s} = 10.58\,\mathrm{GeV}$ is about 1.05 nb, this cross section is about one third lower than the peak cross section due to the beam energy spread (i.e. about 3-6 MeV), and initial state radiation. A B-factory is also a τ-factory producing almost the same number of τ-pairs as $B\bar{B}$ pairs, the cross section for τ-pair production being $\sigma_{\tau\tau} = 0.92$ nb, making *BABAR* one of most suitable experiments to study rare τ decay processes. The other main physics processes happening at PeP-II interaction region are light quark pair production ($u\bar{u}$, $d\bar{d}$, $s\bar{s}$), commonly referred as uds processes, charm couple production, di-muon production, and BhaBha scattering. In Tab. 2.1 the effective cross for all the main processes is reported, the BhaBha cross section is divergent at small angles and the reported value considers the Bhabha falling into the detector acceptance, which means tracks with polar angles, measured in the laboratory frame, comprised between 18° and 131°.

About 10% of data were taken with a CM energy 40 MeV lower than the $\Upsilon(4S)$ peak, these off-peak data, may be used to study in detail all the physics processes not involving B meson decays, since the energy is under production threshold for B-pair production.

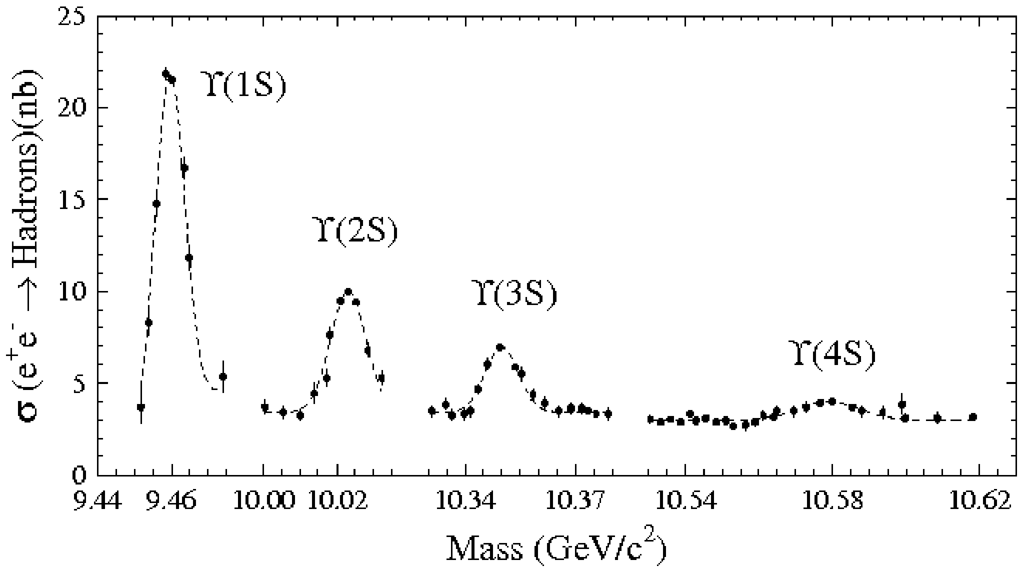

Figure 2.1: Cross section as a function of the CM energy for the first four S-wave Υ resonances. The larger width for the $4s$ resonance is due to the fact that it is the only one above threshold for $B\bar{B}$ production

Table 2.1: Effective cross section for the main physics processes at PeP-II interaction region around $\Upsilon(4S)$. Bhabha angular differential cross section is integrated between 18° and 131° in the laboratory frame.

Process	σ(nb)
$\tau\tau$	0.92
$B\bar{B}$	1.05 (peak $\sim$ 3.6)
uds	2.09
$c\bar{c}$	1.35
BhaBha	25.5
$\mu\mu$	1.16

The off-peak data are particularly interesting for the study of rare processes, as LFV in τ decays, where the understanding of all the background contribution is crucial for the estimation of the UL.

PeP-II is an asymmetric e^+e^- collider. The electron beam, circulating in the *High Energy Ring* (HER), has an energy of 9.0 GeV and collides with a 3.1 GeV positron beam, circulating in the *Low Energy Ring* (LER), resulting in a boost for the CM of $\beta\gamma \sim 0.56$ in the laboratory frame. The choice of a boosted CM made it possible for BABAR to distinguish the decay vertexes of the B's produced in $\Upsilon(4S)$ decays, permitting to study time-dependent CPV in the B system. A schematics of the PeP-II layout is shown in Fig. 2.2, and accelerator parameters are reported in Tab. 2.2.

Electrons and positrons are injected in the two rings at the collider energies by after being accelerated in the 3 Km long linear accelerator (LINAC) and accumulated in the

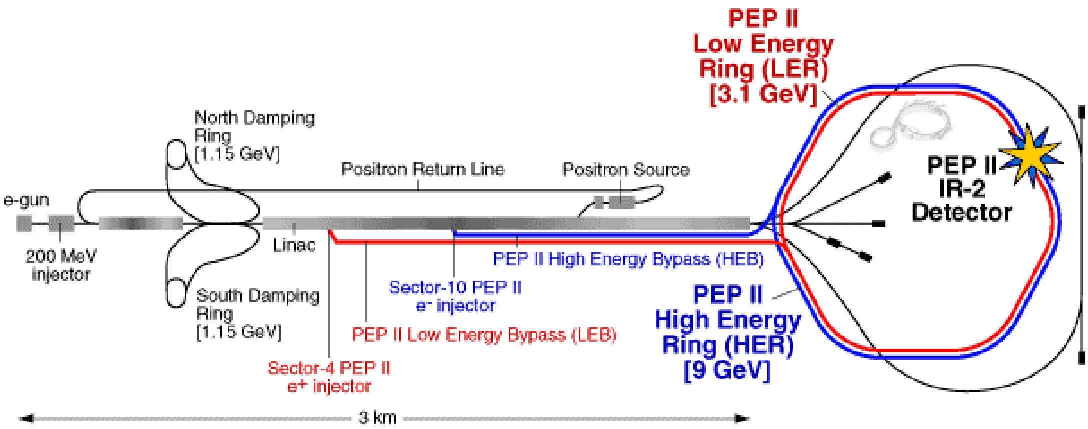

Figure 2.2: Overview of the PeP-II accelerator

Table 2.2: PeP-II accelerator parameters

Parameter	Design	August 2007
Energy HER/LER (GeV)	9.0/3.1	9.0/3.1
Current HER/LER (A)	0.75/2.15	1.87/2.90
Bunch length (mm)	15	11 – 12
Peak Luminosity (10^{33}cm^{-2}s^{-1})	3.0	12.0
Integrated Luminosity (fb^{-1}month^{-1})	3.3	20

PeP-II 2.2 Km long rings.In proximity of the interaction region, the beams are focused by four quadrupole magnets (Q1, Q2, Q3, Q4 as shown in Fig. 2.6) , and a pair of samarium-cobalt permanent dipoles (B1) located at ± 21 cm from the interaction point (IP) which permit to the particle bunches to collide head-on. The B1 dipoles and Q1 quadrupoles operates inside the field of the *BABAR* superconducting solenoid, while the other quadrupoles are located outside the field.

The interaction region is enclosed in a water-cooled beam pipe made of two thin layers of beryllium with a water channel in between, with the outer radius is about 28 mm. To attenuate synchrotron radiation, the inner surface of the beam pipe is gold-plated. The total thickness of the beam pipe section, at normal incidence, corresponds to 1.06% radiation lengths.

The *BABAR* apparatus is installed around the beam pipe at the interaction region.

2.1.1 Beam Parameters Measurements

Two machine parameters are critical for the study of rare processes as LFV in τ decays: the luminosity and the energy of the two beams. A good luminosity measurement is crucial in order to be able to have a good estimation of the actual number of τ-pair produced, on the other hand a small beam energy spread, in absence of radiation in the initial state or in the decay, permit to have a smaller spread in the energy of produced τ's resulting in a higher sensitivity to neutrino-less decay.

Luminosity Monitoring

PeP-II and *BABAR* have different and independent ways to measure the machine luminosity. PeP-II uses an high rate sampling of BhaBha scattering during on-line operations, *BABAR* derives the absolute luminosity off-line from QED processes, primarily by using e^+e^- scattering, and $\mu^+\mu^-$ pair production. The best estimate of the relative error on luminosity is 0.8% for data taken before Summer 2003 and 0.5% for the remaining data [45].

Beam Energy

The mean energies of the two beams are calculated from the total bending strength and the beam orbits, including the effects of off-axis fields and steering magnets. The systematic uncertainty on the calculation of the absolute energies of the beam is estimated to be $5 - 10\,\mathrm{MeV}$ for PeP-II, while the relative energy setting is known with a $1\,\mathrm{MeV}$ precision. The energy spread is different in LER and HER being $2.3\,\mathrm{MeV}$ and $5.5\,\mathrm{MeV}$ respectively. In order to record data close to $\Upsilon(4S)$ peak the observed ratio between $B\bar{B}$ and lepton pair production is monitored online, with a 2.5% change in the $B\bar{B}$ rate corresponding to a 2 MeV change in the CM energy at the resonance peak. Unfortunately in this way it is not possible to know the sign of the energy change. To know the absolute error for the beam energy, momentum of fully reconstructed B mesons constrained with the known B meson mass are used. An absolute error of $1.1\,\mathrm{MeV}$ is obtained for $1\,\mathrm{fb}^{-1}$, this error is equally limited by the error on B meson mass and detector resolution.

2.1.2 PeP-II performances

PeP-II started to deliver data to *BABAR* detector in 1999 and as already mentioned ended its operational period April 2008, recording a total integrated luminosity of 531 fb^{-1} including about 54 fb^{-1} off-peak data, 433 fb^{-1} recorded on-peak, and 44 fb^{-1} collected at other resonances (namely $\Upsilon(3S)$ and $\Upsilon(2S)$). *BABAR* recorded luminosity is shown in Fig. 2.3.

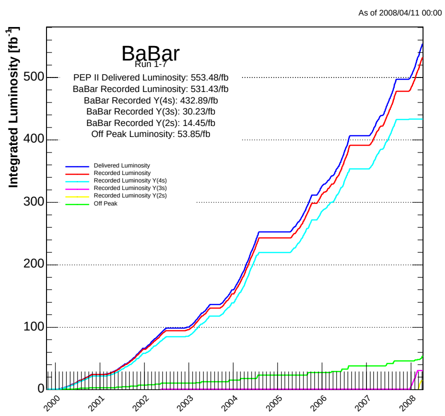

Figure 2.3: Luminosity recorded by *BABAR* detector.

As can be seen in Tab. 2.2, PeP-II surpassed its design performances, both in term of instantaneous luminosity (by a factor 4) and daily integrated luminosity (by a factor 6)[44]-[46]. The increase in instantaneous luminosity is mainly due to the increase in beam currents and improved focusing and a better control of beam orbits. A major improvement in PeP-II operation has been achieved between December 2003 and March 2004 with the implementation of a new procedure called *trickle injection*. Before the implementation of *trickle injection* PeP-II operated in series of 40-minute fills during which the colliding beams coasted: it took three to five minutes to replenish the rings between two fills, and during the filling time, the *BABAR* data acquisition system had to be turned off for detector safety due to the high backgrounds caused by the injection.

The *trickle injection* on the other hand permitted a virtually uninterrupted data-taking period with the LINAC continuously injecting new particles with small injection at small rates (up to 10Hz in the HER and 20Hz in the LER). This novel method of injection allows an increase in the integrated luminosity between 20% and 30%, (Fig.2.4 moreover the continuous injection made the beam more stable making easier machine operation and a very important overall reduction of beam losses. After a beam loss approximately 15 minutes are needed to refill the ring with no data taking possible for detector safety reason.

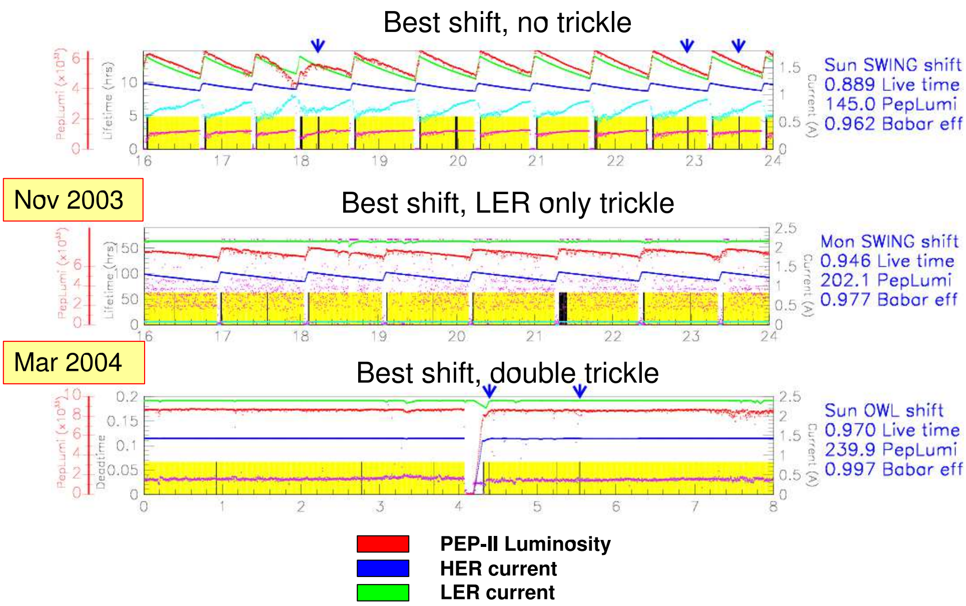

Figure 2.4: Comparison between the best 8-hour period of data-taking for three different period of data taking. Top panel: no trickle, middle panel: trickle only in LER, bottom panel: trickle on both LER and HER.

2.2 The *BABAR* Detector

The *BABAR* detector was designed and optimized to study CPV in the B meson systems, nonetheless it is well suited for the study of rare processes such as LFV τ decays. To achieve the goals of performing accurate event reconstruction there are many features needed:

- a large and uniform acceptance, in particular down to small polar angles relative to the boost direction, to avoid particle losses. Although the boost is small this generate an asymmetric detector design even in the innermost tracking systems like for the SVT;

- excellent detection efficiencies for charged particles down to very small momenta, threshold being about 60 MeV/c;

- good vertex reconstruction and precise momentum measurement resolution, uniform in the kinematic range comprised between 60 MeV/c and 4 GeV/c;

- identification of electrons and muons over a wide range of momentum, great $\pi - \mu$ separation even at low momenta using information both from inner trackers and dedicated particle identification sub-detector;

- highly efficient, selective trigger system with redundancy so as to avoid significant signal losses and systematic uncertainties.

Other technical issues have been addressed in order to handle high collision rates and the machine induced backgrounds and radiation doses

- low noise electronics and data acquisition system both flexible and stable;

- an on-line computing and network system that can control, process, and store the expected high volume of data;

- detector components that can tolerate significant doses of radiation and operate under high background condition.

The *BABAR* detector (Fig. 2.6) has been designed and built by a large international collaboration of international institution from twelve different countries that shared the responsibilities of designing and building the various subdetectors. Details on the subsystems constituting the *BABAR* detector will be given in the next sections.

An overview of the polar (θ) angle coverage for the different sub-detector, their segmentation, and performance is given in Tab. 2.3. The *BABAR* detector is constituted by nested sub-detector: inside superconducting magnet, which produces an axial 1.5 T field, going from the innermost to the outermost detector, lay a five-layer silicon vertex tracker (SVT), a drift chamber (DCH) for charged particle detection and momenta measurement, a ring-imaging Čerenkov detector (DIRC), for charged particle identification, and a CsI(Tl) crystal electromagnetic calorimeter (EMC), for electron and photon momenta measurement and identification. Given the asymmetric design of PEP-II the EMC is designed asymmetrically, with an end-cap extending its coverage downstream of the HER, where many of the collision products emerge. Outside of the magnet field, the instrumented flux return (IFR) is composed of 18 layers of steel, which increase thickness

Table 2.3: Overview of coverage, segmentation and performance of *BABAR* sub-detectors. C, B, and F notations indicate central barrel, backward and forward sectors respectively. All performance reported consider $1\,\mathrm{GeV}/c$ particle except when otherwise specified.

System	θ coverage ($^\circ$)	Channels	Layers	Segmentation	Performance
SVT	[20.1, 150.2]	150 K	5	50-100 μm $r-\Phi$	$\sigma_{d_0} = 55\mu m$
				100-200 μm z	$\sigma_{z_0} = 65\mu m$
DCH	[17.2, 152.6]	7104	40	6-8 mm	$\sigma_{\Phi} = 1$ mrad
				drift distance	$\sigma_{tg(\lambda)} = 0.001$
					$\sigma_{P_t}/P_t = 0.47\%$
					$\sigma(dE/dx) = 7.5\%$
DIRC	[25.5, 141.4]	10752	1	$35 \times 17mm^2$	$\sigma_{\theta_C} = 2.5$ mrad
				$r\Delta\Phi \times \Delta r$	per track
EMC-C	[27.1, 140.8]	2×5760	1	$47 \times 47mm^2$	$\sigma_E/E = 3.0\%$
EMC-F	[15.8, 27.1]	2×820	1	$47 \times 47mm^2$	$\sigma_{\Phi,\theta} = 3.9\%$ mrad
IFR-C	[47, 123]	22K+2K	19+2	20-38 mm	90% μ efficiency
IFR-F	[20, 47]	14.5K	18	28-38 mm	6-8% π mis-id
IFR-B	[123, 154]	14.5K	18	28-38 mm	(1.5-3.0 GeV/c)

moving outwards, with in between 19 planes of resistive plate chambers (RPCs) or limited streamer tubes (LSTs). IFR allows muon identification and in particular helps π/μ separation.

The average momentum of particles in $\tau \to l\gamma\nu\bar{\nu}$ around $1\,\mathrm{GeV}/c$, the errors on the tracking resolution is dominated by Coulomb multiple scattering, rather than the intrinsic tracking resolution. Thus particular care was given to keep the material, in the active region of the detector, to a minimum. Fig.2.5 shows the material in unit of radiation length for each sub-detector, each curve represents the radiation length transversed before the particle reach the first active layer of a particular sub-detector. During the whole data-taking period for the *BABAR* detector many efforts were made to get the subsystem to work beyond their design performance. In particular novel software recipes were implemented to improve tracking and particle identification capabilities, which are crucial to the measurement we are going to perform. In the following sections we will describe the general performances of the sub-detectors, while an in-depth description of the software methods adopted for this particular analysis will be described in Chap 3.

2.3 The Silicon Vertex Tracker

The SVT provides precise measurement of the decay vertexes and of the charged particle trajectories in the region near the interaction point. The mean vertex resolution along the z-axis for a B meson decay is less than 80 μm, making it possible to undergo precision measurement of time-dependent CP asymmetry; a 100 μm resolution in the $x-y$ transverse plane is necessary to reconstruct the decays of the τ leptons.

The choice of five layers of double-sided silicon strip sensors allow a complete tracking reconstruction even in the absence of DCH informations. The SVT also provides the only mean for tracking particles with low transverse momenta (p_T) with momenta that cannot

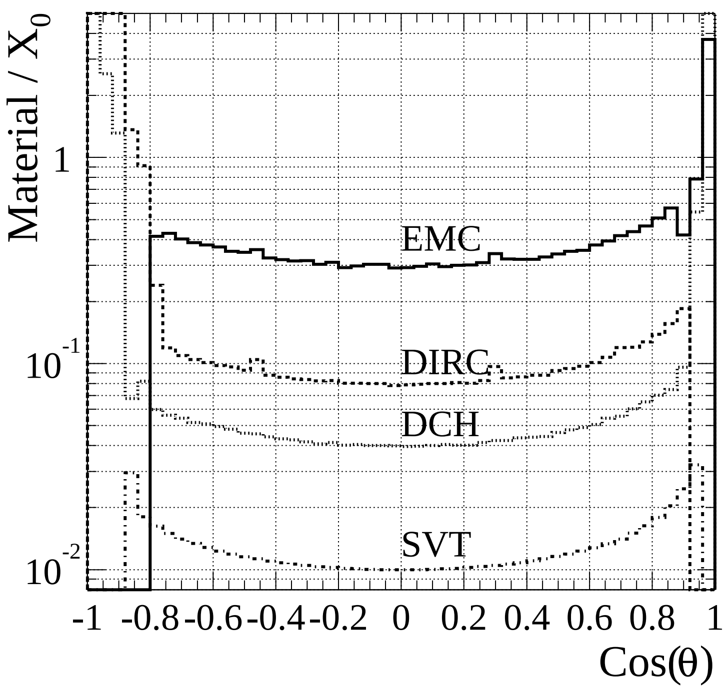

Figure 2.5: Overview of the material in front of each sub-detector, in units of radiation length, as a function of polar angle

be measured in the drift chamber, like soft pions coming from D^* decays, and for particle produced in high multiplicity τ decays.

The SVT provides also useful information for particle identification for both low and high momentum tracks. For low momenta (less than 300 MeV/c) the SVT dE/dx measurement is the only information available; when the momentum of the track is more than 500 MeV/c, the DIRC uses the tracking informations from the SVT to achieve its resolution on the Čerenkov angle measurement.

The five layers of SVT are built of of 300μm thick, double-sided microstrip detectors [47]. The total active silicon area is 0.96 m^2 and the material traversed by particles moving normally with respect to the detector is 4%. The geometrical acceptance is 90%.

The active part of the detector consists of high resistivity n^- bulk implanted with p^+ strips on one side, and orthogonally-oriented n^+ strips on the other side. The detectors are operated in reverse mode at full depletion with bias voltages lying in $25-35$ V range. The strip readout pitch is different among the layers and varies from minimum of 50 μm up to a maximum of 210 μm.

The detectors and the readout electronics are assembled in mechanical units called *modules*. The three inner layers have "cylindrical" shape and are composed of six modules each. They are placed around the interaction region, with radial distance of 3.3, 4.0, and 5.9 cm from the beam axis (Fig. 2.7). The detectors in the outer two layers, composed of 16 (the fourth) and 18 (fifth) modules have been assembled to reduce the incident angles of particles coming from the interaction region, the layers have distinctive arc-shapes, and the barrel modules are placed at radii of 122.7 and 14.6 cm from the beam axis, as well shown in Fig. 2.7. Full azimuthal coverage is obtained by partially overlapping

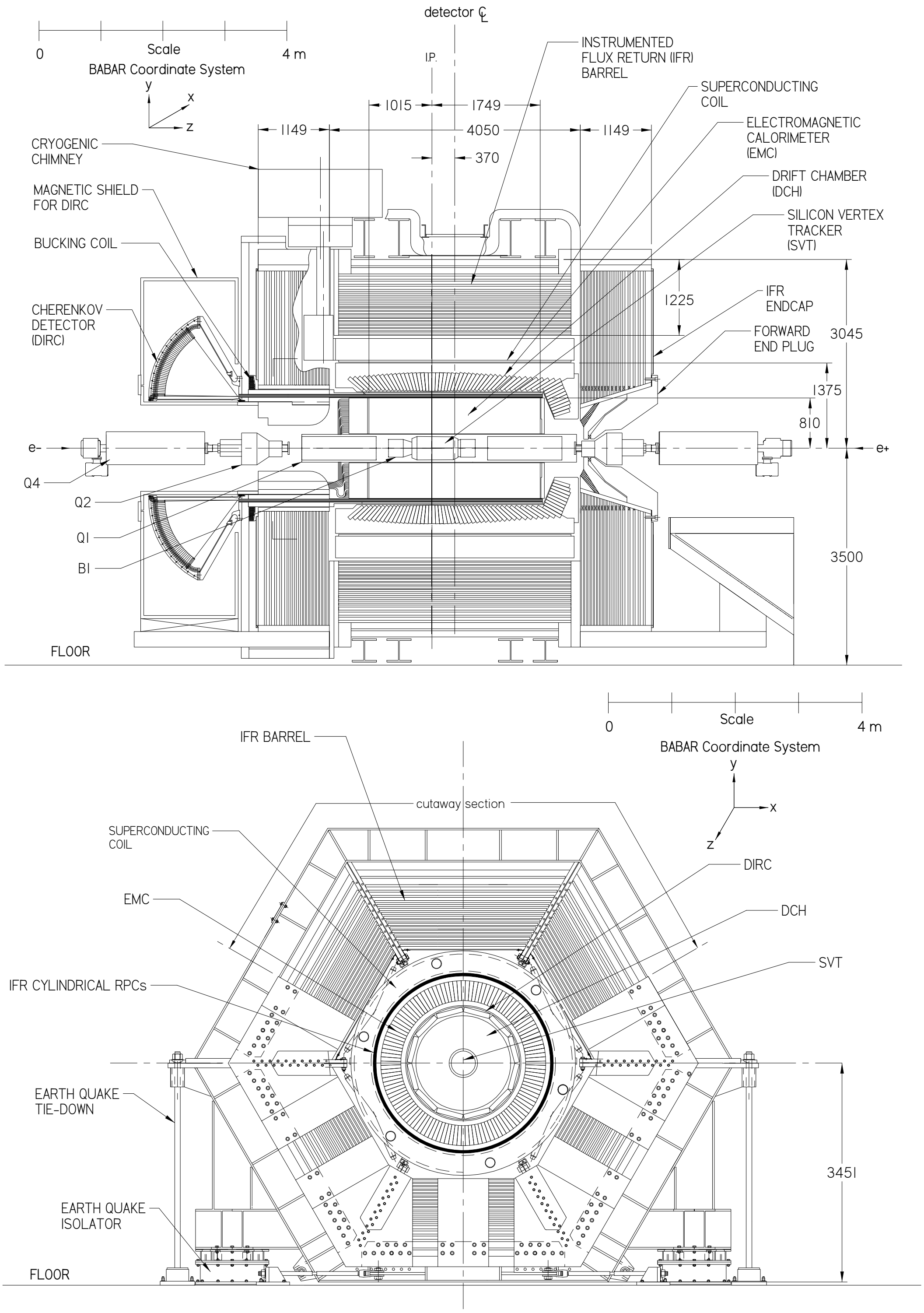

Figure 2.6: Lateral (top panel) and front (bottom panel) views of the *BABAR* detector.

the adjacent modules, the modules are either tilted in the Φ plane by 5° (layers 1-3) or staggered (layers 4-5). The overlap is also advantageous for alignment purposes. The polar angle coverage is $20.1^\circ < \theta_{LAB} < 150.2^\circ$.

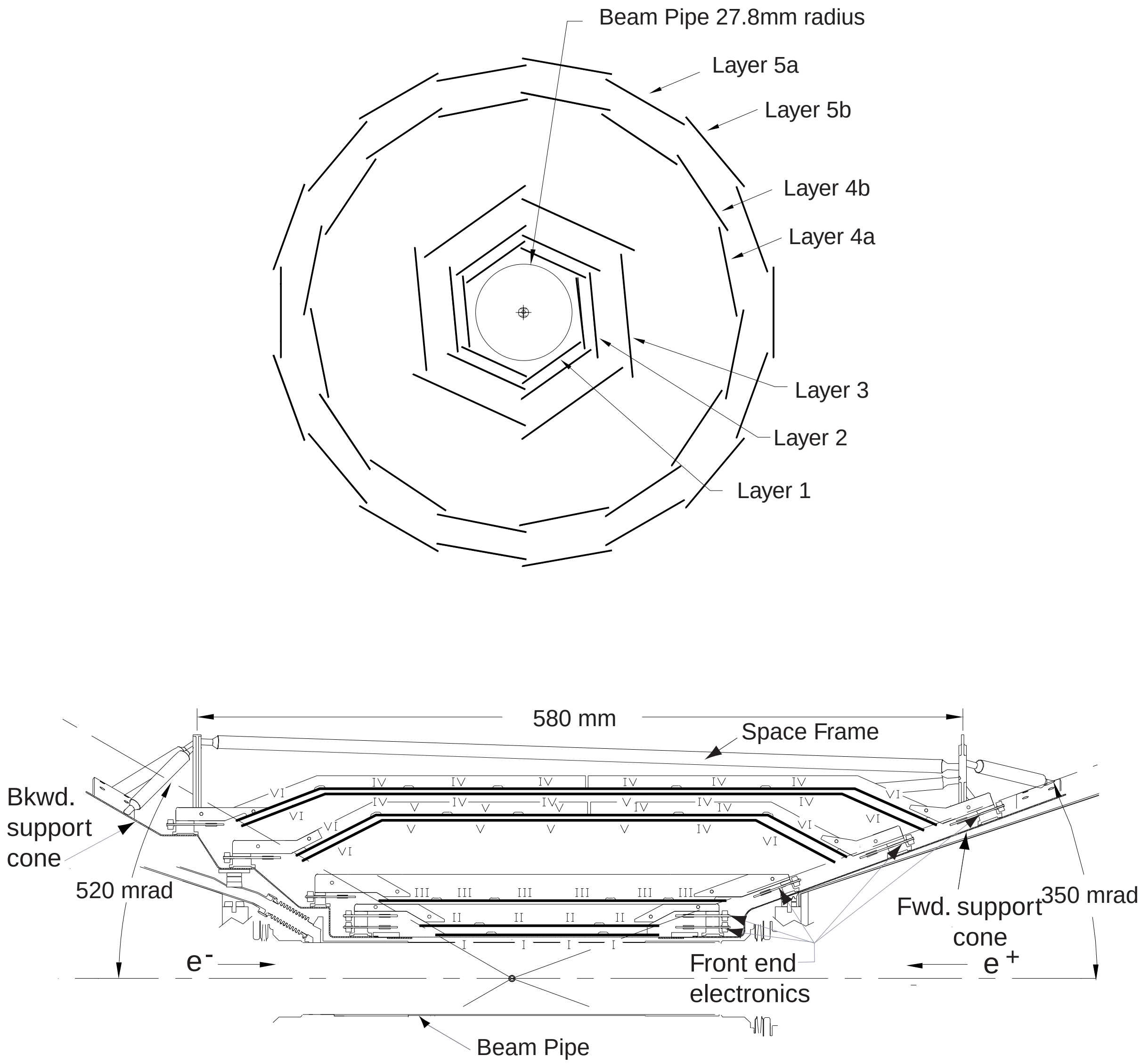

Figure 2.7: Front (top) and lateral (bottom) view of the SVT layout.

Performances

Hit efficiency and resolution

The overall efficiency for the SVT detector, after excluding the only 5 defective readout section out of the 208 constituting the detector is measured to be about 96%.

Fig. 2.8 shows the spatial hit resolution in z and $r - \Phi$ for the five SVT layers, as a function of the track angle of incidence on the silicon wafer plane . The resolution is determined by looking at the distance of the hit in the wafer plane and the reconstructed track trajectory of high momentum tracks. The uncertainty contribution is subtracted to obtain the hit resolution, which varies between $15 - 50$ μm.

Tracking efficiency and track parameter resolution In order to estimate the track detection efficiency the pion spectrum obtained from data is compared with its MC

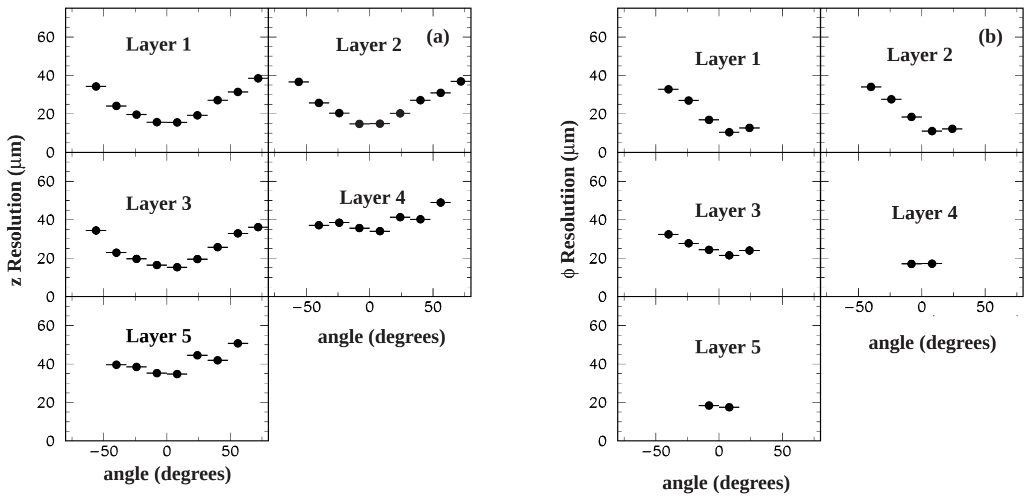

Figure 2.8: SVT hit resolution in z (left) and Φ (right) coordinates in μm.

prediction [33]. Efficiency is estimated to be 20% for particles with momenta up to 50 MeV/c, rapidly increasing to over 80% at 70 MeV/c.

The tracks can be identified by five parameters (d_0,Φ_0, ω,z_0, and $tg(\lambda)$), determined at the track point of closest approach (POCA) to the z axis, and the error matrix associated to the five parameters. d_0 and z_0 are the distances from the interaction region in the (x, y) plane and z axis respectively. Φ_0 is the angle between transverse component of the vector tangent to the track and the x axis. λ is the angle between the vector tangent to the track and the transverse plane. ω is the curvature of the track, this quantity is signed, and incorporates the information on the charge of the track. All parameters, except ω, have errors dominated by SVT intrinsic resolution, while p_T resolution and hence the error on ω is dominated by DCH resolution. Fig. 2.9 shows the resolution for all parameters determined from calibrations using cosmic rays with transverse momenta above 3 GeV/c. In Fig. 2.10 [48] d_0 and z_0 resolutions are shown as a function of p_T.

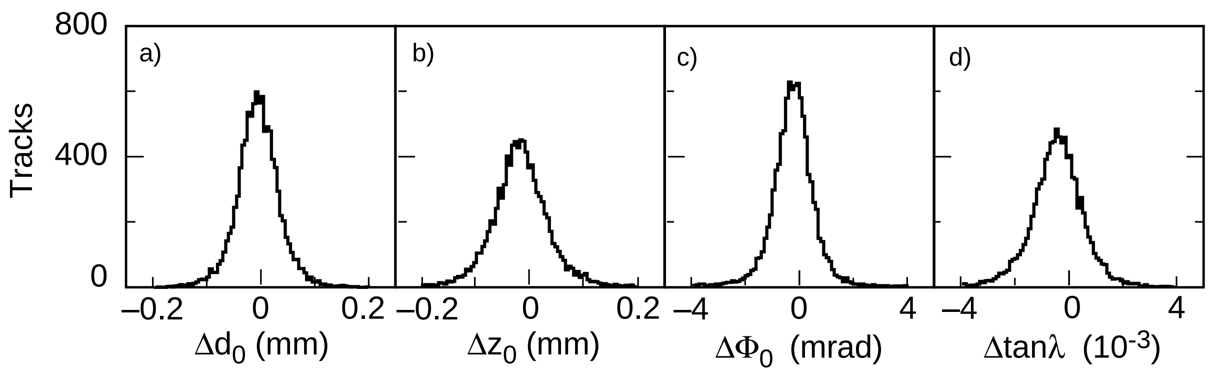

Figure 2.9: Distribution of the differences between the fitted cosmic tracks in the two halves of the SVT.

In order to study the parameter resolution online, the tracks present in the detectors are fitted to the same vertex , and d_0 and z_0 are calculated with respect to the common

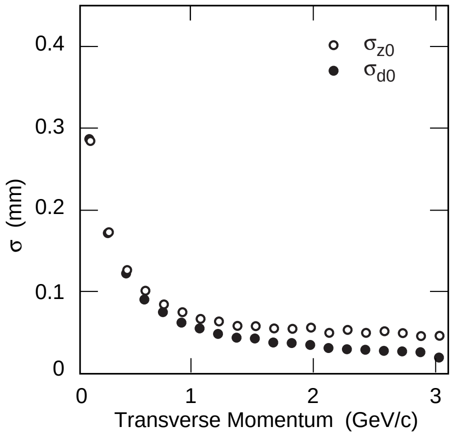

Figure 2.10: Impact parameter resolution in high multiplicity hadron decay as a function of transverse momentum, both in the transverse plane and along the z-axis.

vertex. The contribution from the vertex error are accumulated and fitted for, and removed from the resolution errors. Resolution for d_0 and z_0 are estimated to be 25 μm and 40μm respectively, in good agreement with the cosmic ray expectations.

Particles of low momentum can only be identified through dE/dx in silicon. The particle ID information for those tracks rely only comes from the measurement of the specific ionization loss dE/dx obtained looking at the total charge deposited in the active silicon region. The measurement can be reliably made for tracks with at least 4 hits in the SVT. The SVT dE/dx distribution is shown in Fig. 2.11 [49]. The resolution achieved is about 14% for minimum ionizing particles (MIP), and a 2σ separation between kaon and pions for tracks with momenta up to 500 MeV/c.

2.4 The Drift Chamber

The main tracking sub-system is the DCH chamber, that allows the reconstruction of the tracks with transverse momenta above $p_T \sim 200$ MeV/c, providing the measurement of the curvature of the particle's trajectory inside the 1.5 T magnetic field generated by the superconducting *BABAR* solenoid. The DCH is designed also to measure the coordinate along z-axis, with a $\sim$ 1 mm resolution. The good resolution in the longitudinal coordinate is needed to match properly SVT and DCH tracks and projecting the track to the DIRC and EMC.

For tracks with low momenta the DCH provides information over dE/dx which can be used for particle ID purposes, allowing a good K/π separation for transverse momenta up to $\sim$ 700 MeV/c, the DCH particle ID capabilities are complementary to the DIRC in barrel region, while it is the only mean of particle ID in the backward and forward direction where DIRC coverage is incomplete.

The DCH provides also real-time information used in the charged particle trigger as described in Sec.2.8

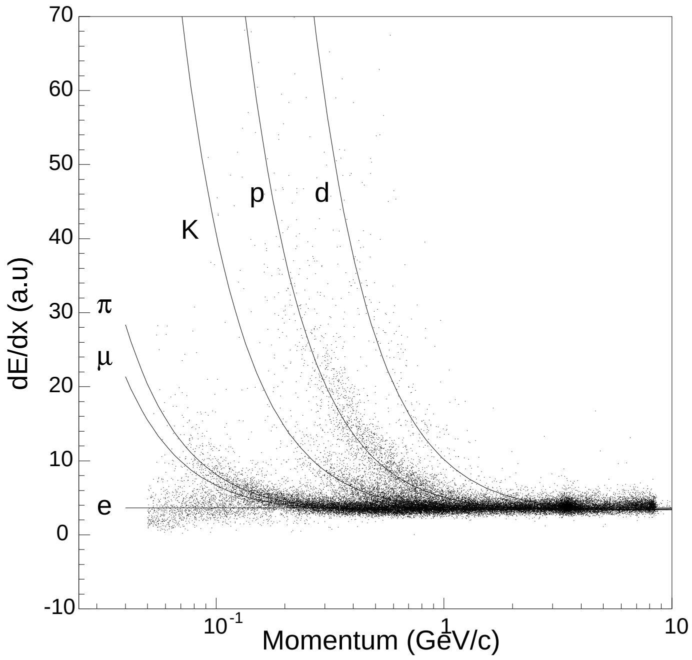

Figure 2.11: Ionization energy loss measured in the SVT as function of track momentum. Vertical scale is arbitrary

Detector Layout

The DCH design is illustrated in Fig.2.12, it consists of a 280 cm-long cylinder located outside the PEP-II support tube [50]. The inner radius is 23.6 cm and the outer is 80.9 cm. The tracking volume was designed with the center of the DCH being displaced by 36.7 cm in the forward direction, to cope with the PeP-II asymmetric boost, thus increasing the acceptance for charged particle going forward.

The drift systems consist of 7104 hexagonal cells, arranged in 40 concentric layers. Each cell consist of one sensitive wire and six field wires, as shown in Fig. 2.13. The field wires are at ground potential while high positive voltage is applied to the sensitive wires. The layers are grouped in 4 super layers, shown in Fig. 2.13. Super layers are also used for a quick local segment finding in the first step in L1 trigger pattern recognition. In order to be able to measure the z position of the hit two different types of wire were used: the type A, parallel to the z-axis, provides the position in $x - y$ plane, while the longitudinal position is obtained with wires placed at small angles with respect to the z-axis.

Low mass materials and reduced thickness has been chosen in the design to limit the effect of Coulomb multiple scattering on the momentum measurement of low p_T particles. The 40 layers provide up to 40 position measurements for particles with $p_T > 180\,\mathrm{MeV}/c$. The material within the chamber has been minimized (0.2% X_0) using low-mass field wires and an helium based gas mixtures. The gas mixture is reported in Tab.2.4. A resolution of around 7% has been achieved also for $\mathrm{d}E/\mathrm{d}x$ using the helium-isobutane mixture. The inner wall has been kept thin (0.28% X_0) in order to maintain high precision in the p_T resolution and minimize backgrounds due to photon conversion. The outer wall is thicker (0.6% X_0), but still thin enough to not impair EMC and DIRC performances.

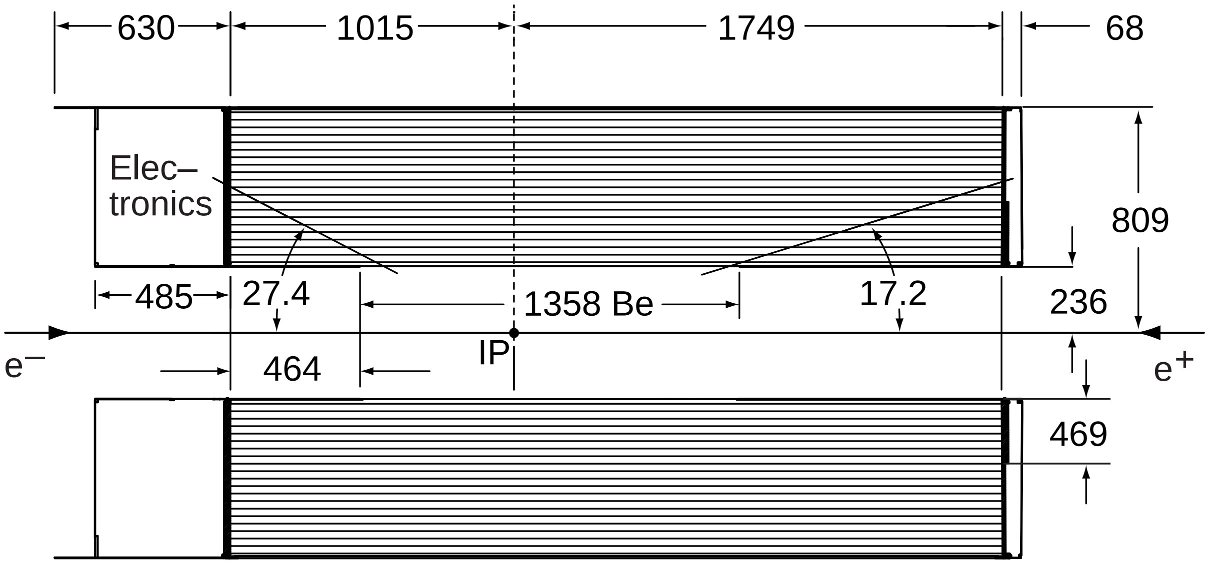

Figure 2.12: DCH layout, the asymmetric position of the center of the chamber is clearly visible.

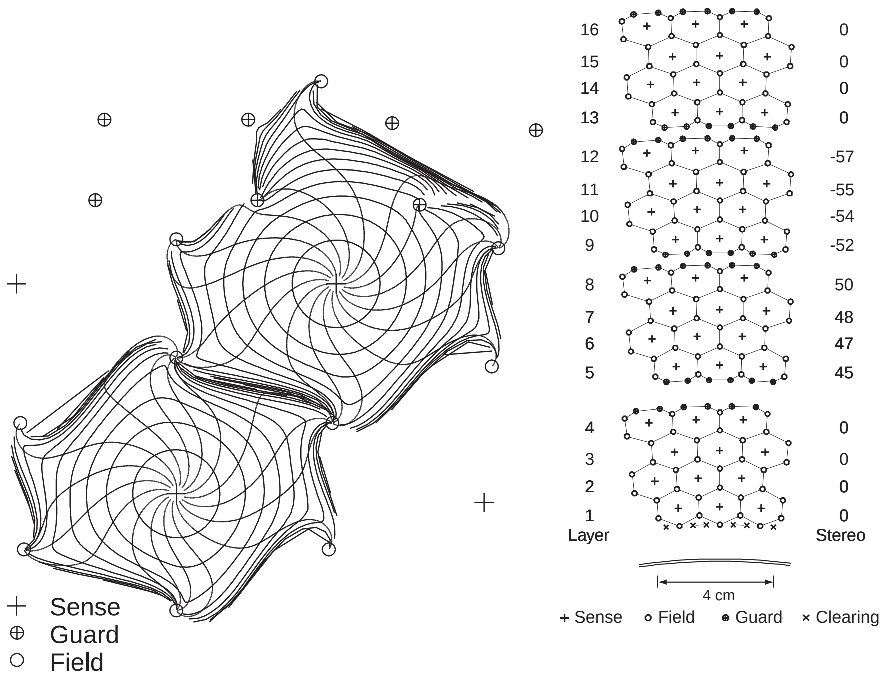

Figure 2.13: DCH cell layout (left) and superlayer structure (right)

Detector Performances

Tracking efficiency and resolution

DCH reconstruction efficiency has been measured using control samples of multi-track events. The absolute drift chamber tracking efficiency is determined as the fraction of all tracks detected in SVT which are also reconstructed in DCH, since the two sub-detectors can actually reconstruct tracks independently. At the design voltage of 1960V the mean

Table 2.4: DCH gas admixture properties at atmospheric pressure and 20°C

Parameter	Value
Mixture H2:C_4H_{10}	80:20
Radiation Length	807 m
Primary Ions (MIP)	21.2/cm
Drift velocity	22μm/ns
Avalanche gain	3×10^4
Lorentz angle	32°
dE/dx Resolution	6.9%

reconstruction efficiency is 98±1% [33]. Due to aging and radiation damage the operating voltage was lowered during later period of data-taking, resulting in an efficiency drop of 2% in efficiency. The dependence of tracking efficiency on polar angle and momentum is shown in Fig. 2.14.

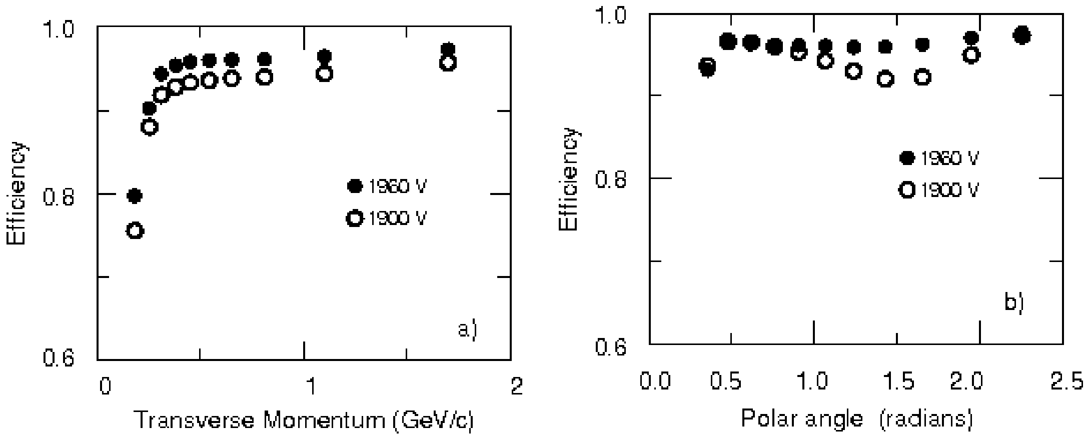

Figure 2.14: Tracking efficiency as a function of transverse momentum (left) and polar angle (right)

The transverse momentum resolution is related to the track curvature (ω) in the magnetic field, and it is measured by studying cosmic ray events [51]. The data are well fitted by a linear function

$$\frac{\sigma_{p_T}}{p_T} = (0.13 \pm 0.01) \cdot p_t\% + (0.45 \pm 0.03)\% \tag{2.1}$$

where p_T is measured in GeV/c. The contribution proportional to p_T comes from finite spatial measurement resolution, and dominates at high p_T. The constant term dominates at low p_T and is due to multiple scattering in the material.

dE/dx resolution

The specific ionization loss for charged particles is derived by measuring the charge deposited by the traversing particle in each drift cell, by making ad average from the lowest 80% energy deposits measured. In Fig. 2.15 the distribution of the reconstructed dE/dx

from the drift chamber as a function of the particle momentum. The superimposed Bethe-Bloch curves have been determined using different control samples for each particle specie. The resolution achieved for dE/dx measurement is 7.5%, as shown in Fig. 2.15, limited by the number of samplings and the Landau fluctuation. A 3 σ K/π separation can be achieved for momenta up to 700 MeV/c [51].

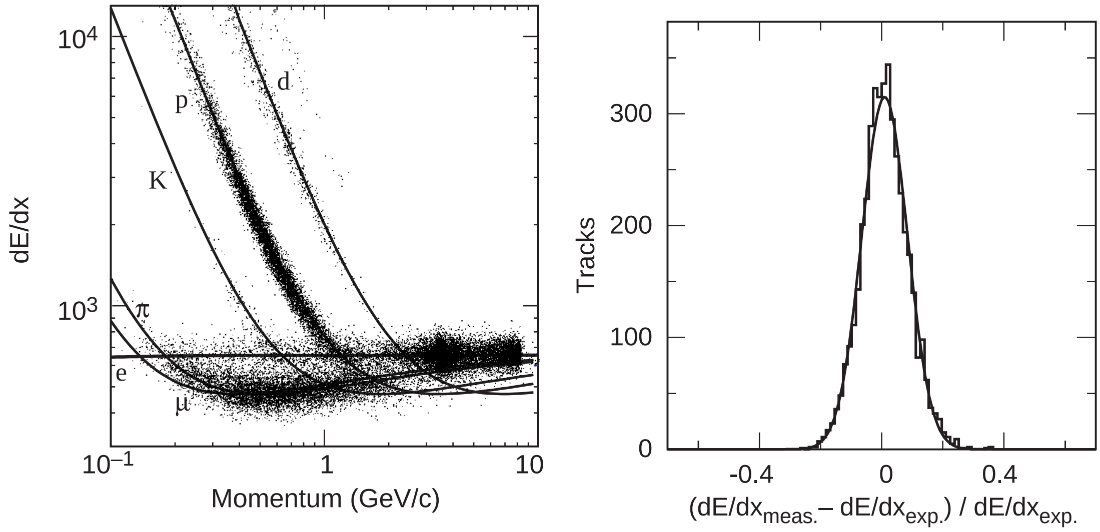

Figure 2.15: Energy loss resolution: on the left dE/dx resolution as a function of particle momentum, on the right difference between measured and expected dE/dx for Bhabha electrons.

2.5 Detector of internally reflected Čherenkov radiation

Particles with $p_T \geq 700$ MeV/c cannot be identified using only the dE/dx informations coming from the inner tracker detectors. A special Čherenkov (DIRC) is the main particle identification system in *BABAR* it allows k/π separation of 3σ or greater for tracks with momenta ranging from 500 MeV/c up to 4.2 GeV/c.

Detector Layout

The DIRC is a novel design ring-imaging Čherenkov detector, it is based on the principle that the light angle is conserved in the reflection on a flat surface [52]. In Fig. 2.16 the schematics of the DIRC detector is shown.

The material used both as a radiator and as light guides in the DIRC, is synthetic silica (its refraction index being $n = 1.473$) fused in 144 bars with rectangular cross section. The bars are 17mm thick, 35mm wide and 4.9 m long, they are arranged in a 12-sided polygonal barrel section, with each side made up of 12 bars. The azimuthal coverage of the system is 94% while it covers only 83% of the polar angle in the CM system. For particles at normal incidence is only 17% X_0. The detector, being only 8cm

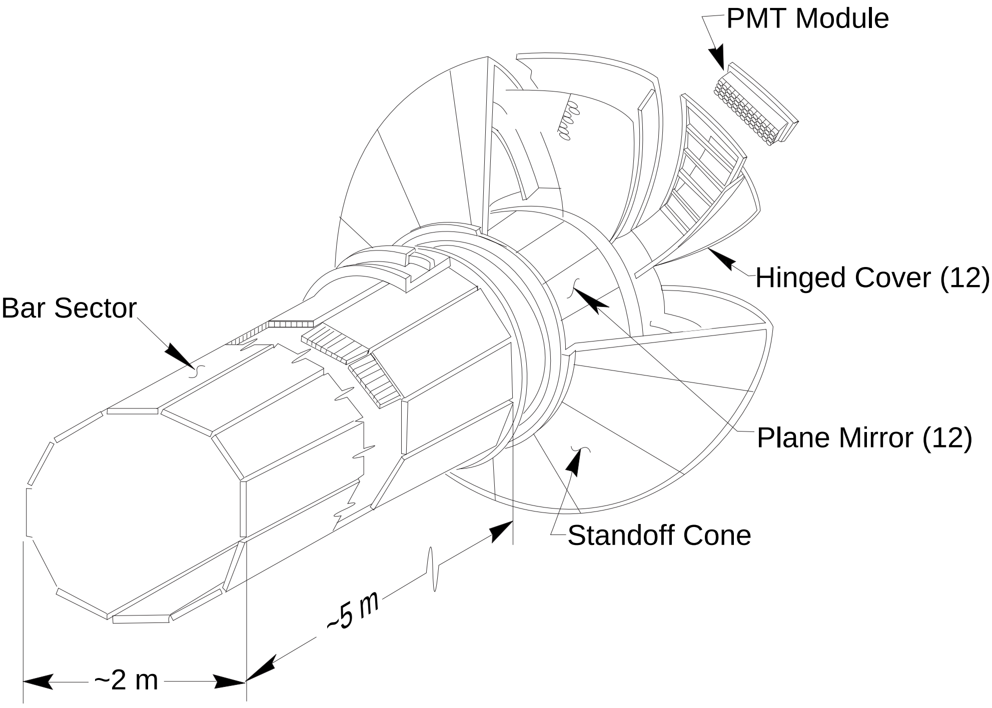

Figure 2.16: Schematics of DIRC radiator bars and detection region

thick, leaves room for a large tracking volume, which allows to achieve precise momentum resolution, and allows to build a compact electromagnetic calorimeter with a high angular resolution.

The bars have also a high internal reflection coefficient, greater than 0.9992 per bounce, making optimal light guides. A charged particle traversing the silica bar generates a Čherenkov light cone of angle $2\theta_C$ with its axis along the particle direction, $\cos\theta_C = 1/\beta n$. For particles with $\beta = v/c \sim 1$, some photons will be reflected inside the tube and transported to wither one or both ends of the bar. To avoid any losses or having detectors at both ends of the detector, a mirror, perpendicular to the bar axis was placed at the forward end of the bars, and it reflected incident photons towards the backward end of the detector, where the light detection system was installed.

Once photons are guided to the backward region, they emerge into an expansion region (Fig.2.17), filled with 6000 liters of purified water. A fused silica wedge, located at the end of each bar reflects photons at large angles reducing the required detection surface. The light detection system has arrays of densely packed photomultiplier's tubes (PMTs), each of it surrounded by reflecting cones, which capture light otherwise lost by the PMT. The expected Čherenkov light pattern in the expansion region is a conic section, whose opening angle is the Čherenkov angle θ_C, modified by the refraction of the purified water outside the silica window.

Detector performance

The resolution on the Čherenkov angle σ_{θ_C} scale as

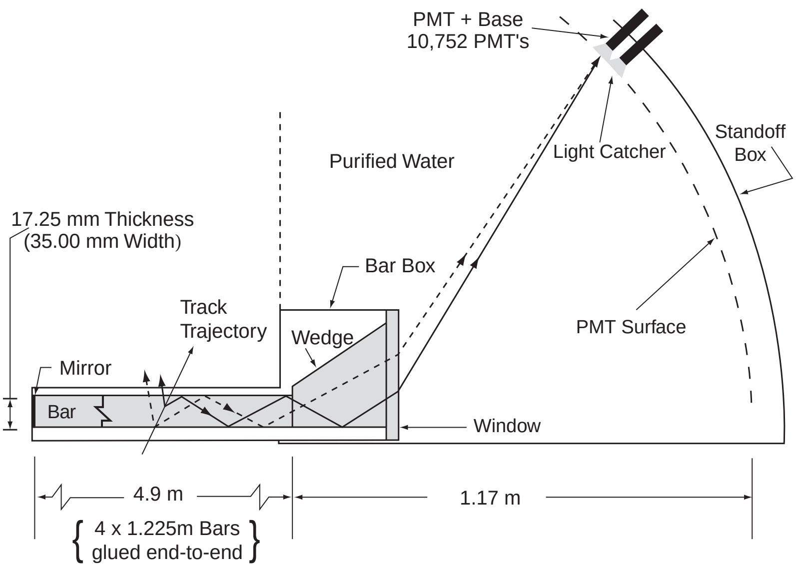

Figure 2.17: Schematics of the radiator and detection system of the DIRC

$$\sigma_{\theta_C} = \frac{\sigma_{\theta_{C,\gamma}}}{\sqrt{N_\gamma}} \tag{2.2}$$

where $\theta_{C,\gamma}$ is the single photon angle resolution and N_γ is the number of Čherenkov photons detected.

The single photon resolution is estimated using di-muon events control samples, and it is measured to be 10.2 mrad, as shown in Fig.2.18. The main contribution on the photon resolution come from the detector geometry (bar size and distance between the wedge and PMTs) and from the spread on the photon production angle.

The number of photons detected varies as a function of the track polar angle, as shown in Fig.2.19, ranging from a minimum of about 20 for $\theta \sim 90°$, to over 50 photons when the track is going towards the forward or backward direction. The detection of more photons by particles with large dip angles is because more material is traversed by the particle, resulting in a higher photon yield, and the angle of emission is such that the number of photon internally reflected by the bars is higher. This feature is particularly useful in *BABAR* thanks to the forward boost of the CM in the laboratory frame, with more particle boosted at large dip angles. A bump is present at $\theta \sim 90°$ because light coming from both forward and backward direction is collected around that angle, the drop in the collected photons for tracks going in the backward direction is due to the absorption in the silica bar.

The combination of the Čherenkov photon angle distribution, the angular distribution of detector photon, and the polar angle distribution of charged track yields an average σ_{θ_C} of about 2.5 mrad, for di-muon events. A similar resolution is found for Kaons and pions using control samples from charm meson decay ($D^{*\pm} \to D^0\pi^\pm$, with $D^0 \to K^\pm\pi^\mp$) reconstructed in data, where $K^\pm/\pi^\mp$ are identified exploiting the charge correlation with the $\pi^\pm$ coming from $D^{*\pm}$ decay. The single track resolution from single tracks as a function of momentum can be measured, from the difference between the expected angles

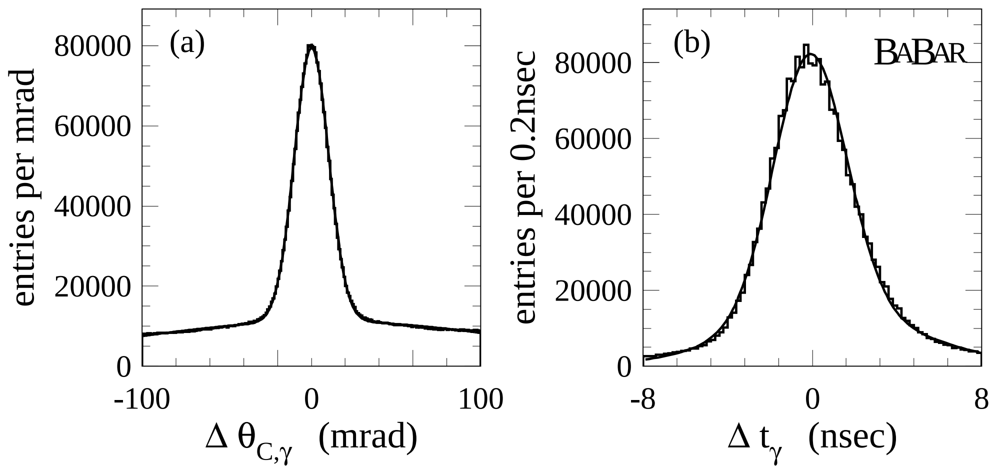

Figure 2.18: Resolution for single photon $\theta_{C,\gamma}$ (left plot) and spread in time of the photon detection (right plot) , measured using a di-muon control sample.

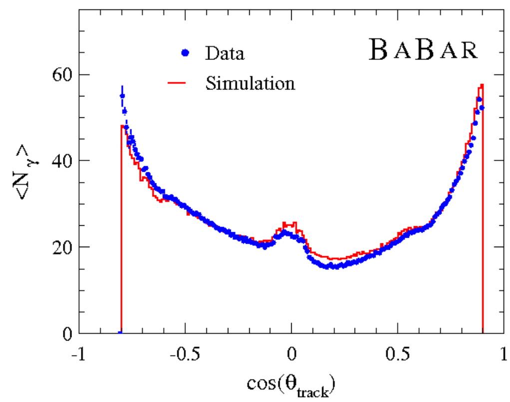

Figure 2.19: number of detected Čherenkov photons as a function of the track dip angle

of charged pions (θ_C^π) and kaons (θ_C^K) K/π separation can be calculated as $|\theta_C^K - \theta_C^\pi|/\sigma_{\theta_C}$. Fig.2.20 show the K/π separation as a function of the reconstructed track momentum

A possible major source of error in the DIRC θ_C measurement is introduced by beam-generated background. Such backgrounds can be suppressed by over-constraining θ_C thanks to the use of the time propagation time in the silica bars: the propagation angle (α_x, α_y, α_z) with respect to the bar axis, is actually directly related to the propagation time. The over-constrain can be used to resolve some ambiguities in the association between PMT hits and the track as the forward-backward ambiguity between photons that have or have not been reflected by the mirror. The measured and expected photon propagation time is used as a discriminating variable to distinguish between signal and background photons. The resolution on the propagation time, as measured in di-muon events (Fig. 2.18), is about 1.7 ns, close to the intrinsic 1.5 ns transit time of the photo-electrons in PMTs. Applying the time information the correct matching photons and tracks improves substantially and reduces the number of accelerator induced backgrounds by a factor 40, as is clearly visible in Fig. 2.21 [53].

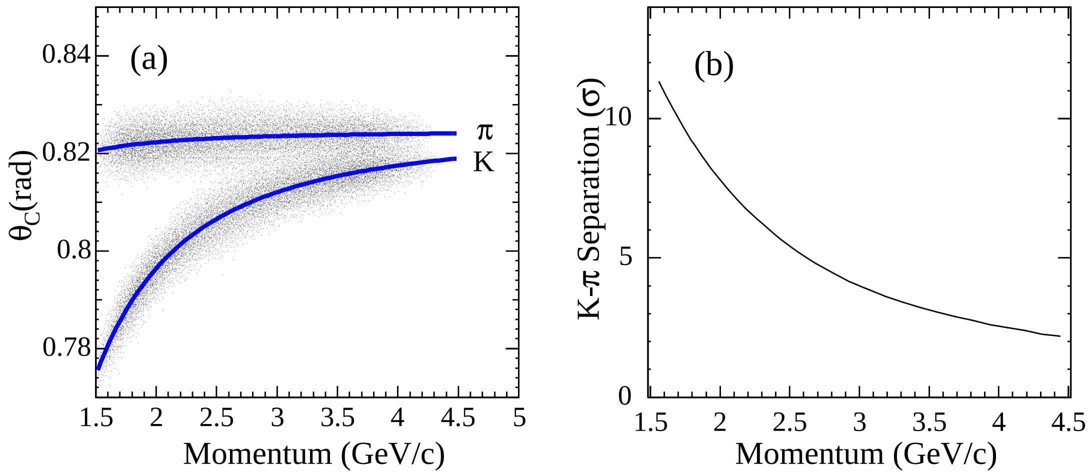

Figure 2.20: On the left the expected distributions for pions θ_C^π and kaons θ_C^K are shown. The right panel shows the average K/π separation

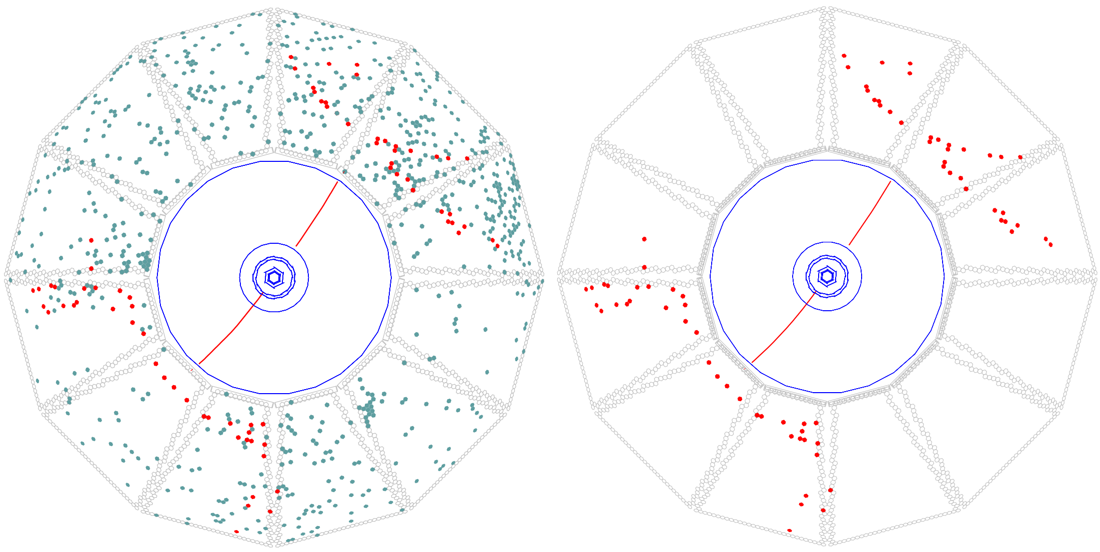

Figure 2.21: Different timing cuts on the DIRC hits: on the left hits recorded in 300 ns after trigger signal, on the right hits recorded in 8 ns after trigger signal

2.6 Electromagnetic Calorimeter

The *BABAR* electromagnetic calorimeter (EMC) is designed for high efficiency detection and precise measurement of the electromagnetic showers, produced by photons and electrons. The EMC is designed to operate efficiently over an energy range, from 20 MeV photons, slow π^0 coming from B meson decays, to up to 9 GeV, that is measured in the study of events originated in initial state radiation processes where an hard photon is produced. Besides precise energy and momentum measurements, the EMC represents the most important sub-detector for electron-hadron separation over a wide range of particle momenta, making possible to have the high electron selection efficiencies needed for this analysis.

The energy deposits clusters are identified as photons by EMC when the lateral shape of the cluster is consistent with the expected pattern from an electromagnetic shower, and when the deposit is not associated with any measured charged track coming from the complete tracking system. Electrons are identified from deposits matching to a charged track, when the ratio between the energy E, reconstructed in the calorimeter, and the momentum p, measured by the tracking systems, E/p is ~ 1.

The need to reconstruct high multiplicity B decays, where slow π^0's may be present, posed strict design requirements to the EMC system, the energy resolution was needed to be better than 1%, along with sensitivity to low energy deposits, up to ~ 20 MeV. This goals has been achieved allowing the reconstruction of B decays with multiple π^0 or η in the final states, with a mass resolution on a single π^0 of 6.9 MeV/c^2. Efficient electron hadron separation was the other main feature EMC should offer, with a 0.1% hadron contamination for particle momenta as low as 500 MeV/c.

The need for high efficiency resulted in a quasi-hermetic coverage of the center of mass system, with a $\sim 90\%$ of polar angle covered by the EMC, and the high energy resolution is achieved thanks to the small amount of traversed material in front of the EMC.

Detector Layout

The EMC is a total-absorption electromagnetic calorimeter, composed of 6580 CsI crystals doped with 1000 ppm of thallium iodide [54]. The CsI(Tl) crystals high light yield and small Molière radius, allow to reach the energy and angular resolution required from the *BABAR* design, while the short radiation length of CsI(Tl) ensure complete shower containment at $\Upsilon(4S)$ energy, maintaining a compact detector design. The main properties of CsI(Tl) crystals are reported in Tab. 2.5.

Table 2.5: Main features of CsI(Tl) crystals.

Parameter	Value
Radiation Length	1.86 cm
Molière Radius	3.8cm
Density	5.43 g/cm^3
Light Yield	$5 \times 10^5 \gamma/$ MeV
Light Yield Temperature Coefficient	0.28%/°C
Peak Emission (λ_{max})	565nm
Refractive Index at λ_{max}	1.79

Each crystal is casted as a truncated trapezoidal pyramid, their front to back length vary from 29.6 cm (16 X_0) and 32.4 cm (17.5 X_0), the typical front surface is 5×5 cm^2. To minimize the material traversed by the particles, the carbon fiber support structure for the crystals and the front-end electronics are located on the outer surface of the EMC, as shown in Fig. 2.22. The small amount of photons not internally reflected by the crystal surface, each crystal is recovered using a reflective material enveloping each crystal. Each crystal is instrumented with two independent 2×1cm^2 silicon photo-diodes on its rear face, which detect scintillation light.

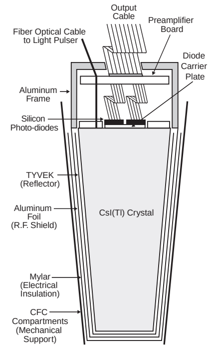

Figure 2.22: EMC crystal module structure. Inner radius at the bottom, outer radius on top. Note how all the electronics is on the outer part of the detector.

Thanks to their shape thee crystals are arranged projectively in two structures. The barrel is composed of 48 crystal rows spanning in the polar angle direction (θ-rows) and 120 rows spanning the azimuthal angle Φ, the barrel has an inner radius of 90 cm as shown in Fig. 2.23. The forward end is closed by a separable end-cap holding nine additional θ-rows allowing further polar angle coverage, needed to increase photon detection efficiency. The full assembly of the EMC provide full azimuthal coverage in the polar angle range of $15.8° < \theta_{LAB} < 140.8°$. In the backward detector there is no crystal coverage.

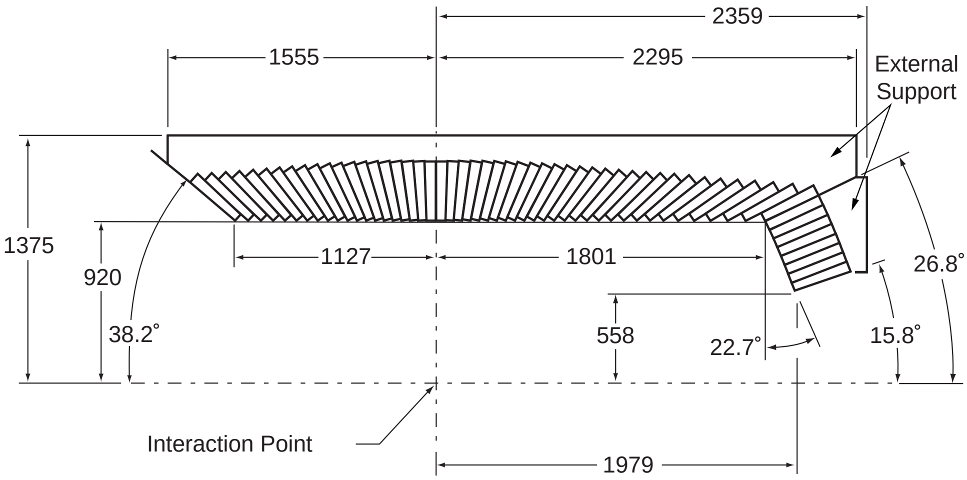

Figure 2.23: EMC barrel and front end layout, all lengths are in cm and all angles in degrees.

Detector performance

Detector performance

As for any homogeneous total absorption calorimeter, the limit on energy resolution is determined by fluctuations in the electromagnetic shower propagation. For BABAR crystal calorimeter the dependence of the resolution on the shower fluctuation is empirically described as the quadratic sum of a stochastic term $\sigma_1 E^{-\frac{1}{4}}$ and a constant term σ_2 as:

$$\frac{\sigma_E}{E} = \sigma_1 E^{-\frac{1}{4}} \oplus \sigma_2 \tag{2.3}$$

The stochastic term is dominant at lower energies, and depend primarily on fluctuations in photon statistics, and, to a lesser extent, on electronic noise in the readout chain and on beam generated backgrounds. σ_2 instead, dominates at higher energies and depend on several different effects: the main contribution to σ_2 arise from fluctuation in shower containment due to energy leaks out of the crystal rear face, or from the absorption in the material between, and in front of, the crystals. The other main contribution to σ_2 comes from uncertainties in the calibrations, which are not energy dependent.

The energy resolution is measured on selected control samples from the data recorded by *BABAR* detector, these control samples include electron and positrons produced in BhaBha scattering, which are selected over a wide momentum range (between 3 and 9 GeV/c); photons from π^0 and η decays, which have energies under 2 GeV, and from $\chi_{c1} \rightarrow J/\Psi\gamma$ ($E_\gamma \sim 500\,\text{MeV}$). At low energies the resolution is calibrated weekly, performing measurement with a radioactive $^{16}O^*$ source, which produces 6.13 MeV photons. The resolution dependency on energy is the fitted as shown in Fig.2.24, and the empirical parametrization from Eq.2.3 for *BABAR* detector is measured to be[54]:

$$\frac{\sigma_E}{E} = (2.32 \pm 0.30)\% E(\text{ GeV})^{-\frac{1}{4}} \oplus (1.85 \pm 0.12)\% \tag{2.4}$$

The stochastic term dominates at energy lower than 2.5 GeV, above this energy the constant term becomes the limiting factor to the resolution.

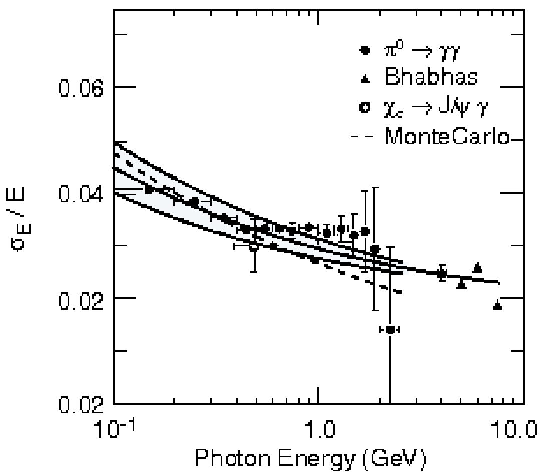

Figure 2.24: EMC resolution as a function of Energy, obtained using different control samples. The solid line represent the Eq.2.3, and the gray area between solid lines represents 1σ errors.

Angular resolution

The main limit on the angular resolution of the EMC depends on the transverse crystal size and the distance from the interaction point, improving for crystals with smaller transverse size. The crystals have been designed to optimize the transverse size maintaining good energy resolution. The electromagnetic showers have a natural lateral spread of the order of the Molière radius, depending on the scintillating material, so the crystal can't be significantly smaller than the Molière radius. Decreasing too much the size of the crystals does not increase space resolution because of the summing of the electronic noise from several different crystals.

The chosen size of CsI(Tl) crystals allows an angular resolution of few milliradians at low energies, in the worst expected case.

The angular distribution of EMC is shown in Fig.2.25 as a function of energy. The resolution is measured using π^0 control samples, where the two photons candidate from the decays have approximately equal energy. The resolution is measured to be between 12 mrad at low energies and 3 mrad for higher energy. An empirical parametrization is used to fit the data, resulting in:

$$\sigma_\theta = \left(\frac{(3.87 \pm 0.07)}{\sqrt{E(\,\mathrm{GeV})}} + (0.00 \pm 0.04) \right) \mathrm{mrad} \tag{2.5}$$

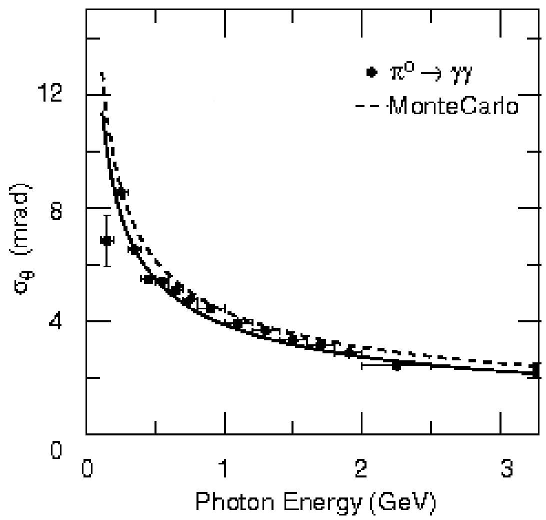

Figure 2.25: EMC angular resolution as a function of Energy, obtained using π^0 control sample. The solid line represent the Eq.2.5

2.7 Instrumented Flux Return

The instrumented Flux Return (IFR) is designed for muon and neutral hadrons (mainly K_L and neutrons) identification, the most needed features for this sub-detector are good solid angle coverage, good efficiency and a high muon identification efficiency for tracks with momenta below 1 GeV/c.

Detector Layout

The IFR uses the the superconducting magnet steel flux return as muon filter and hadron absorber. Track detection was done using single gap resistive plate chambers (RPC) [55], operated in limited streamer mode, for Run1-4. The sub-detector has been upgraded during *BABAR* data-taking period, starting from Run5 the barrel section RPCs were replaced by limited streamer tubes (LST) [56], in Run5 two of the barrel sextants were instrumented with Limited Streamer Tubes, while in Run6 all RPCs in the barrel sectors were substituted.

The RPCs detect charge generated in the electric field inside the chambers by the particles passing trough, via capacitive readout strips. The main advantage of RPCs is the presence of large signal and fast response, allowing a time resolution as good as 1-2 ns. The spatial resolution depends on the readout segmentation of the sub-detector, a resolution of few millimeters for a single hit was achieved during operations at *BABAR* detector.

The RPCs consist of two 2mm thick Bakelite sheets, separated by a 2mm gap. The resistivity of the Bakelite sheets have been tuned to be $10^{11} - 10^{12}\Omega$cm. The external surfaces of the Bakelite sheets are coated with graphite to obtain a surface resistivity of 100KΩ/cm^2, the surfaces facing the gap are treated with linseed oil to improve their performances. The two graphite surfaces are connected to a voltage of about 8KV, in order allow charge amplification, and protected by a Mylar film using for insulation purpose. A cross section of a IFR module is shown in Fig. 2.26. The modules are operated in limited streamer mode with a capacitive readout on both sides of the gap, made of aluminum strips.

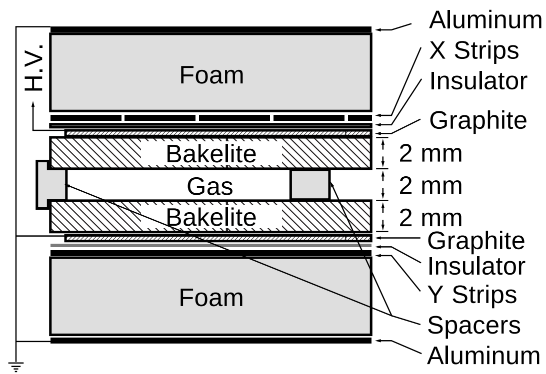

Figure 2.26: IFR RPC module cross section

The RPCs modules were installed inside the gaps formed by the segmented steel of the six barrel sectors and the two end doors as shown in Fig. 2.27. The steel segmentation has been optimized in order to provide good hadron filtering for muon identification. The steel has been segmented in 18 plates, of increasing thickness going towards the outer part of the detector, with a minimum thickness of 2 cm in the 9 inner plates to 10 cm of the outermost plate, for a total steel thickness of 65cm. In addition to the modules installed in the flux return, two cylindrical plates of RPCs work inside the *BABAR* solenoid magnetic field, and are placed between the EMC and the magnet cryostat in order to detect particles going exiting EMC and to keep track of showers going trough the crystals.

Data used in this analysis has been collected with both RPC only ($\mathcal{L} = 235.9$ fb^{-1}) and with LST in the barrel region ($\mathcal{L} = 234.1$ fb^{-1}) which have been installed between 2004 and 2006 [57]. The replacement was needed because of the observed deterioration and continuous decreasing of RPC efficiency, mainly due to temperature excursions and other enviromental conditions.

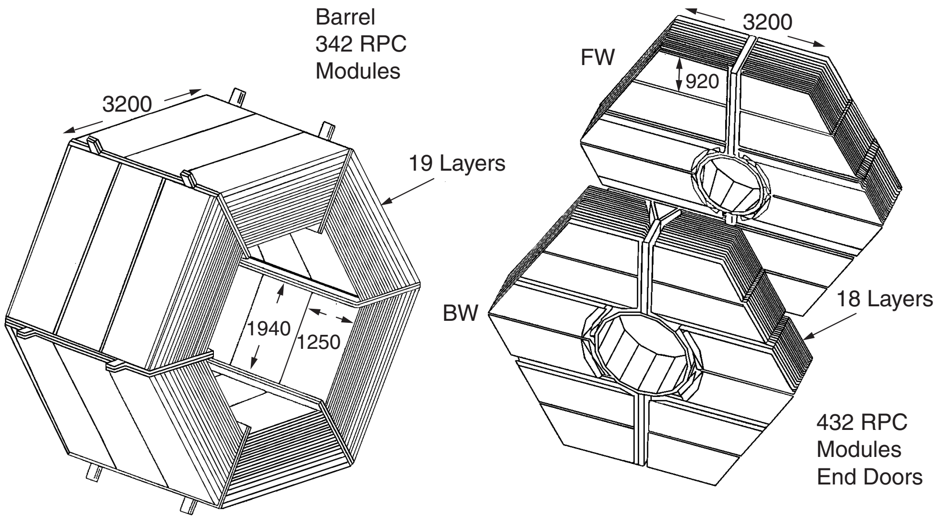

Figure 2.27: IFR sub-detector layout, showing both the barrel (left) and end doors (right) sections. The stratification of the modules can be seen in both sections.

The LST detector [56] consist of silver plated wire with 100 μm diameter, located at the center of a cell filled with gas. A plastic (PVC) extruded structure, or profile, contains 8 such cells, open on one side (see Figure 2.28). The profile is coated with a resistive layer of graphite, having a typical surface resistivity between 0.1 and 1 MΩ/cm^2. The profiles, coated with graphite and strung with wires, are inserted in plastic tubes ("sleeves") of matching dimensions for gas containment. The signals for the measurement of one coordinate can be read directly either from the wires or from external strip planes attached on both side of the sleeve.

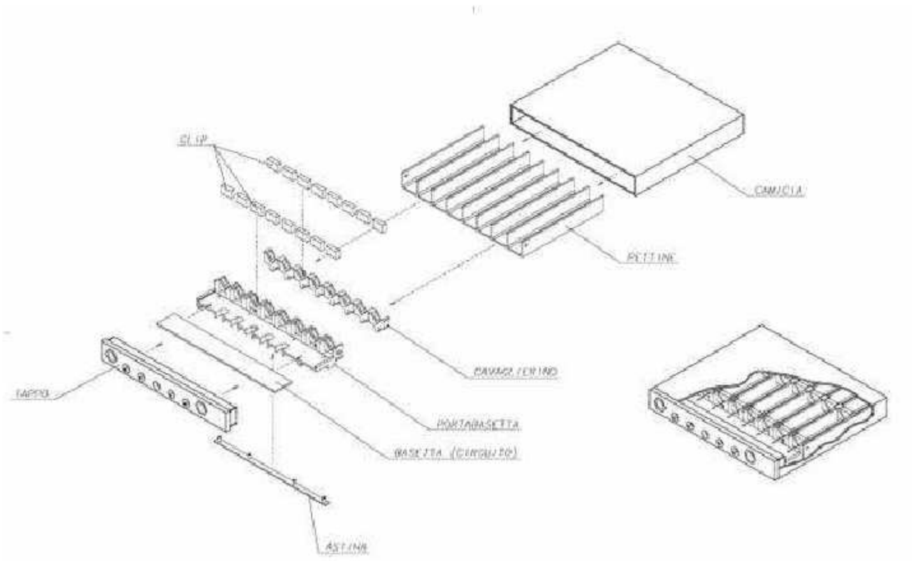

Figure 2.28: Schematics for the standard Limited Streamer Tube module

A 15x17 mm^2 cell design is used where each tube is composed by 7 or 8 cells and assembled in modules. In order to obtain high performances and to respect the safety requirements a ternary gas mixture of $Ar/C_4H_{10}/CO_2$ (3/8/89)% has been chosen [58].

A voltage of 5-6 KV is applied between the cell and the sensitive wire, and HV connectors are put on one of the end-caps: a charged particle traversing the cell ionizes the gas and the high voltage applied on the wire allows a charge stream to build up, which can be measured from the wire. At the same time the signal will be induced on the strips above. The charge on the wire is used to measure the azimuthal coordinate Φ while the induced charge allows to measure the z coordinate. The steel segmentation is used to infer the r coordinate, which is taken from the layer position, and along with the other two measurements it consent to have a three-dimensional hit information. Studies performed shown an average efficiency for LST modules above 90% measured from cosmic ray runs, which did not degrade during the one and a half year of operations.

Detector Performance

Tracking efficiency

The efficiency of IFR sub-detector (for both RPCs and LSTs modules) is measured from enriched data samples of high momentum muons collected both during normal operations, from $e^+e^- \to \mu^+\mu^-$ events, and dedicated cosmic ray runs. The efficiency is measured observing the hit found in the chamber under study when a charged track is expected to traverse it, based on the extrapolation from the inner trackers and the other IFR chambers, the efficiency itself is defined as the ratio of the number of recorded hit and the number of expected hits. The absolute efficiency at nominal working voltage, of 7.6 KV for RPCs and 5.5 KV for LSTs, is used by the reconstruction software for loose muon selection, and is stored in the database used for online data processing by *BABAR*.

After the installation and commissioning of the IFR system in 1999 the RPC modules were tested with cosmic rays, resulting in an average efficiency to be $\sim 92\%$, as shown in Fig. 2.29.

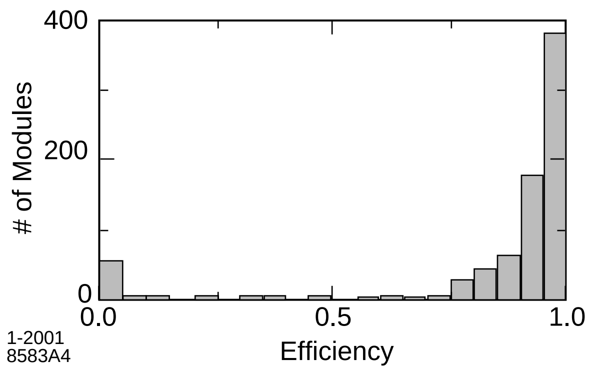

Figure 2.29: Distribution of the efficiencies of RPCs after installation, as can be seen from the leftmost bin ~ 50 modules were not operational upon installation.

As stated in the previous section, after installation a progressive and steady efficiency reduction was observed in the months following the installation, in a significant fraction of RPC modules. Detailed studies of RPC chambers revealed regions were the efficiency reduction was much larger with respect to the average degradation, however no clear pattern was identified nor the source of the problem was identified. The efficiency measured in the first year of RPC operation is shown in Fig. 2.30

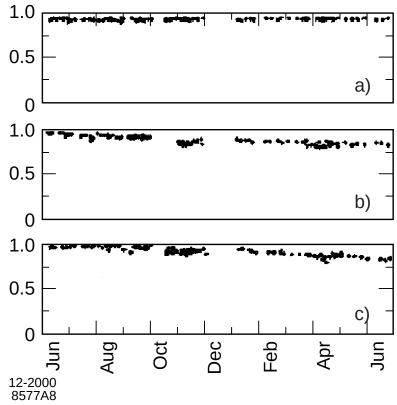

Figure 2.30: Efficiency history for 12 months starting in June 1999 for RPC modules showing different performance. Top: highly efficient and stable. Middle: slow continuous decrease in efficiency. Bottom: faster decrease in efficiency.

After the installation of LST the problem was solved, and the tracking efficiency recovered and remained stable during the period of operation following the installation, as shown in Fig. 2.31.

2.8 The *BABAR* Trigger System

The *BABAR* trigger is designed to be able to select a wide variety of physics processes, ranging from high multiplicity B-meson decay to initial state radiation processes, without overloading the downstream processing, which means having trigger output rates of about 300 Hz. The trigger is required to select physic events of interest with high efficiency, and should be able to select different physics processes with well understood efficiency. In order to allow online diagnostic and background studies the trigger have to be able to select pre-scaled sample of Babha, di-muon, and cosmic events.

The trigger has two independent stages, the second is conditionally dependent over the first stage. The first stage, Level 1 (L1), is an hardware trigger and operates at the machine crossing rate. L1 trigger reduce the data flow rate to a level which can be processed by the second stage, Level 3 (L3) trigger, a software trigger running on a farm of commercial processors.

The L1 is optimized to simplicity and speed of operation, and it consists of a pipe-lined hardware processor. It is designed to provide an output data flow of about 5 KHz. The L1 trigger selection is made using a subset of the information from DCH, EMC, and IFR sub-detectors. The L1 trigger processor produces a 30 MHz clocked output that is passed to the *Fast Control and Timing System* (FCTS), which can optionally mask or pre-scale certain trigger lines. Tab. 2.6 reports the production rates and L1 trigger rates for the main physics processes at $\Upsilon(4S)$ resonance for an instant luminosity $\mathcal{L} = 3 \cdot 10^{33}\mathrm{cm}^{-2}\mathrm{s}^{-1}$.

The L3 trigger is a software trigger, it uses the complete event informations, including L1 trigger processors output and FCTS, the software algorithms composing the L3 trigger

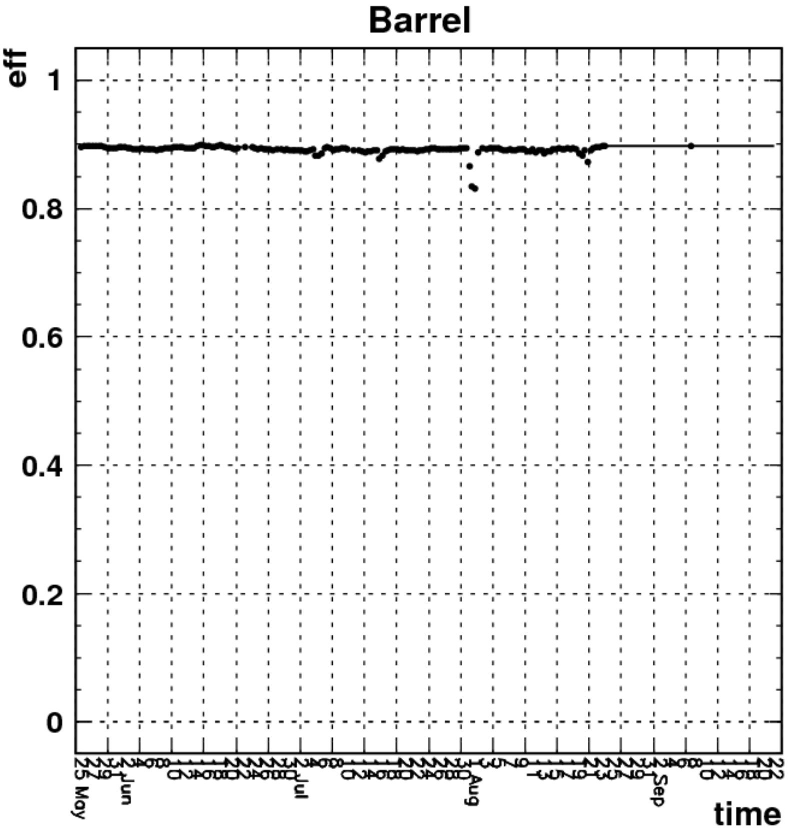

Figure 2.31: Efficiency history for 12 months starting in June 1999 for RPC modules showing different performance. Top: highly efficient and stable. Middle: slow continuous decrease in efficiency. Bottom: faster decrease in efficiency.

Table 2.6: Effective cross section, production rates and L1 trigger rates for the main physics processes at *BABAR*. Rates refer to events with either e^+, e^-, or both in the EMC detection volume.

$e^+e^- \rightarrow$	Cross section (nb)	Production Rate (Hz)	L1-Accept Rate (Hz)
$\tau^+\tau^-$	0.919	2.8	2.4
$b\bar{b}$	1.05	3.2	3.2
$q\bar{q}$ (not b)	3.4	10.2	10.1
e^+e^-	~ 53	159	156
$\mu^+\mu^-$	1.16	3.5	3.1

select events to be stored on tapes for further analysis. The selection process go through two set of orthogonal filters, one based exclusively on track reconstruction information obtained from DCH, and the other based on calorimetry readings of EMC only.

The DCH filter selects all events containing at least one track with $p_T > 600\,\mathrm{MeV}/c$, or two low p_T tracks compatible from being originated from the interaction point. The EMC filters look for energy clusters in the EMC, the *effective mass* is calculated from cluster energy sum and the energy weighted centroid position (in order to reconstruct also the spatial part of the cluster four-momenta) in mass-less particle hypothesis, events with *effective mass* greater than 1.5 GeV is preselected. In order to pass L3 trigger the event must also contain at least two clusters with energy greater than 350 MeV in c.m frame, or four clusters with no energy requirement.

Tab.2.7 shows L3 and L1+L3 trigger accept efficiencies for the main physics processes produced at $\Upsilon(4S)$, all results shown are derived from MC studies.

Table 2.7: L3 and L1+L3 trigger efficiencies for main physics processes produced at *BABAR* experiment. All efficiencies are in %.

	$\varepsilon_{b\bar{b}}$	$\varepsilon_{B\to\pi^0\pi^0}$	$\varepsilon_{B\to\tau\nu}$	$\varepsilon_{c\bar{c}}$	ε_{uds}	$\varepsilon_{\tau\tau}$
L3 1 track filter	89.9	69.9	86.5	89.2	88.2	94.1
L3 2 track filter	98.9	84.1	94.5	96.1	93.2	87.6
L3 Combined DCH	99.4	89.1	96.6	97.1	95.4	95.5
L3 2 cluster filter	25.8	91.2	14.5	39.2	48.7	34.3
L3 4 cluster filter	93.5	95.2	62.3	87.4	85.5	37.8
L3 Combined EMC	93.5	95.7	62.3	87.4	85.6	46.3
L3 DCH+EMC	$\geq$ 99.9	99.3	98.1	99.0	97.6	97.3
Combined L1+L3	$\geq$ 99.9	99.1	97.8	98.9	95.8	92.0

Chapter 3

Event Preselection and Particle Identification

3.1 Analysis Overview

In the following we will search for the radiative decays of the τ to a charged lepton $\tau \to l\gamma\nu\bar{\nu}$, where $l = e$, μ. Generic $e^+e^- \to \tau^+\tau^-$ events are preselected using standard techniques widely used at B-factories. Each event is divided in two hemispheres by means of the Thrust axis [41] and the two hemispheres are then called "signal hemisphere" and "tagging hemisphere". Depending on the signal mode we require either a muon or an electron together with a single photon candidate on the signal side while on tagging side we require either a lepton or a pion and up to 4 additional photons (fig. 3.1). Events in which a lepton candidate with the same flavor appears in both signal and tagging hemisphere are rejected, in order to suppress background contamination mainly from Bhabha and $e^+e^- \to \mu^+\mu^-$ events.

After preselection some additional refinement cuts are applied to correct for observed MC/Data discrepancy. Later, in chapter 4, we will introduce a set kinematical variables to discriminate signal from background and define and a specific figure of merit to find the best set of selection criteria in order to obtain the lowest total error (statistic+systematic) on the final result.

3.2 Data and MC Samples

For this analysis we used data taken by *BABAR* in the period between October 1999 and September 2007. *BABAR* data sample was collected at a center of mass energy of 10.58 GeV, which we will call *On-Peak* data, and at a center of mass 40 MeV below the $\Upsilon(4S)$ resonance referred as *Off-Peak* data, as reported in Tab. 3.1. The corresponding number of τ-pairs can be calculated using for the cross section the value of 0.919 ± 0.003nb, estimated with `KK2F`[45].

Signal Monet Carlo (MC) samples are used to estimate the selection efficiency and optimize the selection criteria. Monte Carlo generated background samples are used for background estimation and to evaluate MC accuracy in reproducing data. As will be shown, there are some discrepancies between data and MC, this problem was addressed

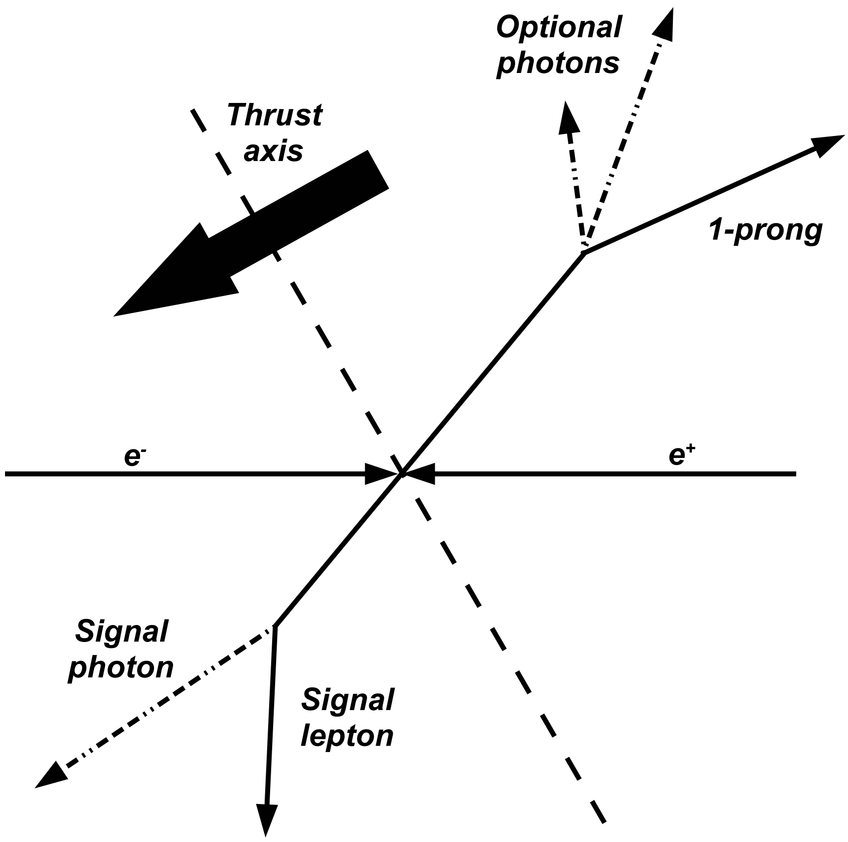

Figure 3.1: Topology of a typical signal event in the center of mass frame.

in different ways during the selection and background extrapolation procedures and will be discussed in detail in the following sections.

The backgrounds considered in the present work can be grouped in three broad classes:

- generic $\tau^+\tau^-$ background: includes all non-signal τ decays according to PDG [15];
- QED backgrounds: $\mu^+\mu^-$ production, Bhabha scattering and two-photon;
- $q\bar{q}$ background: further subdivided in $u\bar{u}/d\bar{d}/s\bar{s}$, $c\bar{c}$ and $b\bar{b}$ MC samples.

For all of the above listed modes suitable MC samples were generated, except for Bhabha and $e^+e^- \to \gamma\gamma$. Their contributions are evaluated directly on data. τ-pair production, for both signal and generic $\tau\tau$ backgrounds was simulated using KK2F generator [60, 61] and their decay was simulated with TAUOLA [62, 63] libraries, radiation in the decay was simulated with PHOTOS [64]. B-meson decays are simulated with EvtGen generator [65], while $q\bar{q}(q = u, d, s, c)$ are produced using JETSET [66] generator. Two different samples are used for $q\bar{q}$, one dealing with $c\bar{c}$ and one used to study $u\bar{u}$, $d\bar{d}$, and $s\bar{s}$, in the following the latter will be referred to as *uds* sample.

All events produced by MC generators are processed using a detailed *BABAR* detector model, simulating both particle interacting in the detector material, and the detector electronics response to the traversing particles, the detector is modeled using GEANT4 simulation package [67].

Run	Period	*On-Peak* $\mathcal{L}\,\mathrm{fb}^{-1}$	*Off-Peak* $\mathcal{L}\,\mathrm{fb}^{-1}$
Run1	Oct 1999-Oct 2000	20.8	2.6
Run2	Feb 2001-Jun 2002	61.6	6.9
Run3	Dec 2002-Jun 2003	32.5	2.5
Run4	Sep 2003-Jul 2004	101.6	10.1
Run5	Mar 2005-Aug 2006	134.9	14.5
Run6	Jan 2007-Aug 2007	79.6	7.9
Total	Oct 1999-Aug 2007	431.1	44.5

Table 3.1: Data collected in each data taking cycle by *BABAR* detector, and corresponding number of τ-pairs produced

Run1	Run2	Run3	Run4	Run5	Run6
292770237	958730314	501290667	1593488357	2104338820	1262807458

Table 3.2: Total number of Data events used in the analysis.

The same reconstructed variables are present in MC and Data sample, but the information about the original decay (as produced by event generators), is also contained in the MC sample (MC truth). To take into account the different running conditions between different data-taking periods, MC samples were produced for each Run, proportionally to the amount of luminosity integrated in a given data-taking Run. To further reduce the mismatch between data and MC *BABAR* keeps track of all changes in condition and calibrations occurred during data-taking, so that MC events can be simulated in conditions as close as possible to the real data.

A breakdown of the total number of events for the MC simulated background samples along with equivalent luminosity and cross-section are reported in tables 3.2, 3.2 and 3.2 respectively. For non-simulated backgrounds the same luminosity as data is assumed unless otherwise stated.

	Run1	Run2	Run3	Run4	Run5	Run6
$\tau\bar{\tau}$	19687000	57194000	49002000	180077000	237094000	139424000
$\mu\bar{\mu}$	24597000	74079000	38890000	121574000	153551000	94085000
uds	44588000	185688000	137541000	416151000	514364000	327032000
$c\bar{c}$	55254000	164722000	88321000	267308000	344275000	208664000
$b\bar{b}$	69818000	209749000	113923000	336585000	431121000	265560000

Table 3.3: Total number of background MC events used in the analysis.

The signal Monte Carlo consists of one (signal) τ decaying radiatively to a charged lepton and the other one decaying according to the current experimental knowledge. This decay mode is already included in the list of `Tauola` standard decay modes, hence, instead of producing a dedicated signal MC sample, we can filter on generic τ decays in which, together with the charged lepton at least one photon is emitted in decay. This way we have the advantage that we can use events from *BABAR* central MC production, whose equivalent luminosities are reported in 3.2, saving much computing time, in particular

	Run1	Run2	Run3	Run4	Run5	Run6	Total
$\tau\bar{\tau}$	21.4222	62.2350	53.3210	195.9488	257.9913	151.7127	742.6310
$\mu\bar{\mu}$	21.4446	64.5850	33.9058	105.9930	133.8718	82.0270	441.8272
uds	21.3340	88.8460	65.8090	199.1153	246.1072	156.4746	777.6861
$c\bar{c}$	42.5030	126.7092	67.9392	205.6215	264.8269	160.5108	868.1106
$b\bar{b}$	66.4933	199.7610	108.4981	320.5571	410.5914	252.9143	1358.8152

Table 3.4: Equivalent luminosities of data and MC events used in the analysis.

	σ (nb)
$\tau\bar{\tau}$	0.919 ± 0.003
$\mu\bar{\mu}$	1.147 ± 0.004
uds	2.09
$c\bar{c}$	1.3
$b\bar{b}$	1.05

Table 3.5: Cross sections for the various MC modes considered in the analysis.

for detector simulation and reconstruction, and gaining in statistics with respect to a dedicated MC production. These decays are simulated by `Tauola` with 4-body phase space and full polarization matrix. Details may be found in [36].

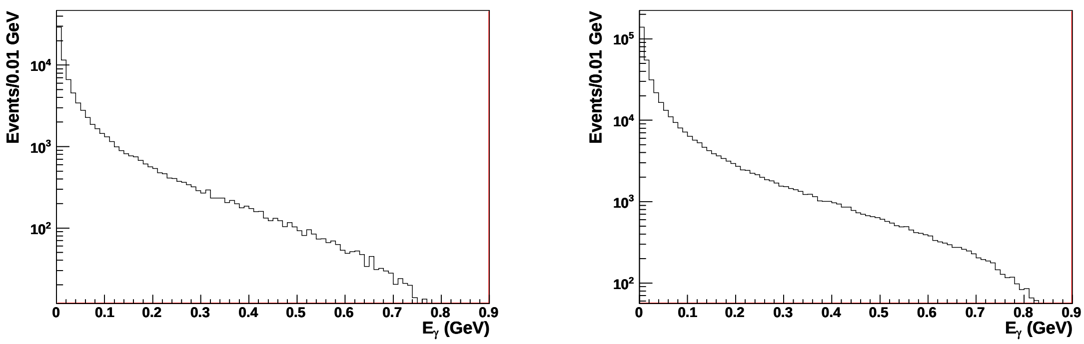

Figure 3.2: Photon energy spectrum in the τ rest frame for $\tau \to \mu\gamma\nu\nu$ (left) and $\tau \to e\gamma\nu\nu$ (right) decays as given by `Tauola` (normalization is arbitrary).

As has already been stressed in chapter 1 and as shown in figure 3.2 the energy spectra for both $\tau \to l\gamma\nu\bar{\nu}$, $l = e, \mu$ decays are infrared-divergent. This means that one has to make an assumption on the minimum allowed energy; this energy corresponds to the minimum energy which can be experimentally detected. The most common choice is to assume a minimum photon energy of $E^*_{gamma} < 10$ MeV in the τ rest frame. In this analysis we don't apply any cut to define our initial signal sample; instead we consider the full photon energy spectrum as given by `Tauola` to calculate efficiency. In this way we are able to verify which is the actual minimum value for the photon energy (E'_γ) to which we are experimentally sensitive. Only after the whole selection procedure is defined we will check how many events with $E^*_\gamma < 10$ MeV survive selection criteria and correct our selection efficiency. The branching fractions for $\tau \to l\gamma\nu\bar{\nu}$, $l = e, \mu$ decays as given by `Tauola` with and without the cut-off at $E^*_\gamma = 10$ MeV are shown in 3.2. The total number of events for both signal channels is reported in table 3.2. Finally we have checked for possible generator-level asymmetry for the two charge conjugated states and found them to be compatible within statistical accuracy. The explicit results are reported in table 3.2 for all four samples.

	$\Gamma_{(\tau\to l\gamma\nu\nu)}/\Gamma_{tot}$	$\Gamma_{(\tau\to l\gamma\nu\nu)}/\Gamma_{tot}$ $(E^*_\gamma > 10MeV)$
$\tau \to e\gamma\nu\nu$	2.805 ± 0.002	1.843 ± 0.002
$\tau \to \mu\gamma\nu\nu$	0.573 ± 0.001	0.3686 ± 0.0009

Table 3.6: MC branching fractions calculated by `Tauola` for the two signal channels.

	$N(\tau \to l\gamma\nu\nu)$	$N(\tau \to l\gamma\nu\nu)$ $(E_\gamma > 10MeV)$
$\tau \to e\gamma\nu\nu$	38287010	25156135
$\tau \to \mu\gamma\nu\nu$	7821197	5031227

Table 3.7: Total number of MC signal events, positive and negative, used for efficiency calculation.

	Γ^+/Γ^-	Γ^+/Γ^- $(E_\gamma > 10MeV)$
$\tau \to e\gamma\nu\nu$	1.003 ± 0.002	1.003 ± 0.002
$\tau \to \mu\gamma\nu\nu$	1.001 ± 0.004	0.995 ± 0.005

Table 3.8: Charge ratio $\Gamma^+/\Gamma^- = \Gamma_{(\tau^-\to l^-\gamma\nu\nu)}/\Gamma_{(\tau^+\to l^+\gamma\nu\nu)}$ for `Tauola` branching fractions for the two signal channel.

3.3 Charged Track Reconstruction

Information from SVT and DCH are processed to reconstruct charged tracks present in each event accepted by the trigger system. The track finding and fitting procedure make use of a Kalman filter algorithm [68], which takes into account the material in the detector, the full magnetic field map, and the hit information. A raw list of reconstructed tracks is produced in the earlier stages of the processing, then a refinement sequence is applied.

The refinement assembles basic information from different tracks, finding primary and secondary vertexes, then the tracks are further selected to remove tracks reconstructed from noise hits in the SVT and DCH sub-detectors (*ghosts*), and tracks generated by a single charged particle, with low p_T, spiraling inside the tracking volume (*loopers*). To improve the momentum resolution hit not associated to any track are added or removed depending on the probability of the hit to fit the reconstructed track trajectory.

In the offline analysis a candidate track list is created starting from the sub-list generated during online processing and refinement stages, at reconstruction level pion mass hypothesis is applied to all reconstructed tracks since the particle identification information is not used. In the analysis tracks are selected if surviving the following criteria:

- **Detector Acceptance**: the track should be inside the EMC acceptance, thus it is required to have a reconstructed polar angle direction in the laboratory frame of $0.41 < \theta_{LAB} < 2.46$.

- **Minimum Transverse Momentum**: the reconstructed track should have a minimum transverse momentum of $p_T > 0.1$ GeV/c, so at least minimal particle identification information will be available in the following stages of the analysis.

- **Maximum Total Momentum**: the reconstructed track is required to have a maximum total momentum $p < 10\,\mathrm{GeV}/c$, this request reduces the number of mis-reconstructed tracks and refine the overall tracking performance rejecting mis-assigned hits in the tracking volume.

3.4 Photon Reconstruction

Photons are reconstructed from EMC energy deposit clusters. The reconstructed photons are required to not match any charged track extrapolated from the tracking volume to the inner surface EMC, for all clusters momenta and angles are assigned to be consistent with photons originating from the interaction region. Photon candidates are required to have an energy $E_\gamma > 30$ MeV in the laboratory frame, this cut is set in order to reduce the beam-induced backgrounds of low energy photons, and the contributions coming from the detector noise. Backgrounds from hadrons such as neutrons and K_L is reduced using cluster shape information.

A shape variable, LAT, is used to discriminate between electromagnetic and hadron clusters in the EMC using the lateral shape distribution of the electromagnetic shower. The LAT is defined as:

$$LAT = \frac{\sum_{i=3}^{N} E_i r_i^2}{\sum_{i=3}^{N} E_i r_i^2 + E_1 r_0^2 + E_2 r_0^2} \tag{3.1}$$

where N is the number of crystal associated to the shower, r_0 is the average distance between two crystals, which is about 5 cm in BABAR detector, E_i is the energy deposited in the i-th crystal, crystals are numbered so to have $E_n > E_{n+1}$, and r_i is the distance between the crystal and the shower center. The summation starts from the third most energetic deposit, so the two crystals containing the largest amount of energy do not contribute to LAT. Since electron and photons deposit most of their energy in few crystals, the value of LAT is small for electromagnetic clusters, and weighting energies with squared distances enhances the difference between electromagnetic and hadronic shower shapes. Photon candidates are required to have $LAT < 0.8$.

3.5 $e^+e^- \to \tau^+\tau^-$ Candidates

The first step of preselection is to reconstruct $e^+e^- \to \tau^+\tau^-$ event candidates, rejecting backgrounds coming from other processes. During this stage, unless otherwise stated all tracks have a pion mass hypothesis assigned.

3.5.1 Trigger and Background Filters

In order to reduce the sample under study before further offline selection trigger informations and background filter flags are used. Both trigger and background filters are applied before the reconstruction of the signal τ candidate, and use only raw reconstruction of tracks and clusters.

Trigger Flags

The events are required to pass both L3 trigger selectors:

- **L3OutDCH** trigger line selects events using reconstructed tracks and is defined as the OR operation of:
  1. *DCH based one track criteria*: at least 1 track is present in the event with $p_T > 600\,\mathrm{MeV}/c$, and the track should have its reconstructed point of closest approach to the interaction region not further than $d_{xy} < 1$cm in the transverse plane and $d_z < 7$cm along the beam axis;
  2. *DCH based two tracks criteria*: at least 2 tracks present in the event both with $p_T > 250\,\mathrm{MeV}/c$, with $d_{xy} < 1.5$cm and $d_z < 10$cm.
- **L3OutEMC** trigger line selects events using EMC information and is defined as the OR operation of:
  1. *EMC high energy criteria*: at least two clusters with $E > 350\,\mathrm{MeV}$ are present in the event, and the event total invariant mass should be $M > 1.5\,\mathrm{GeV}/c^2$;
  2. *EMC high multiplicity criteria*: at least 4 clusters with $E > 100\,\mathrm{MeV}$ are present in the event and the event total invariant mass should be $M > 1.5\,\mathrm{GeV}/c^2$;

Background Filters

For further background reduction raw event informations a series of background filters (BGF) are applied to the events passing the L3 trigger. All events are requested to have at least two charged tracks, for charge conservation, and the subscripts 1 and 2 identify the first and second highest momentum tracks. Filters involving charged tracks have some requirements on R2, defined as the ratio of 2^{nd} and 0^{th} Fox-Wolfram moment, computed in the CM frame. The Fox Wolfram ℓ^{th} moment is defined as [69]:

$$H_\ell = \sum_{i,j} \frac{|p_i||p_j|}{E_{vis}^2} P_\ell(cos\theta_{ij}) \tag{3.2}$$

where p_i are the momenta of the tracks present in the events, E^2_{vis} is the visible energy in the event, and θ_{ij} is the angle between the i^{th} and j^{th} track. The Fox-Wolfram moments are indicators of the event shape, showing how spherical the event is. Two back to back tracks give a value of 1, while high multiplicity spherical events tend to have values close to 0.

A given event passes BGF selection if it satisfies at least one of the following BGF criteria:

- **Multi-Hadron BGF**: requires the event to have at least three tracks and $R2 < 0.8$, most of the signal events pass this filter, while it rejects events with large neutral hadron contribution

- **Tau BGF**: requires at least two tracks and no net charge in the event. The sum of the momenta of the two highest momentum tracks is required to be $p_1 + p_2 < 9\,\mathrm{GeV}/c$, $E_1 + E_2 < 5\,\mathrm{GeV}$. In order to reduce $e^+e^- \to q\bar{q}$ contribution only events with $E_1/p_1 < 0.8$ and $E_2/p_2 < 0.8$ are selelcted. Since at least one neutrino is present, the event should have $E_{CM}-p_1-p_2 > 0$ and $(p_1+p_2)/(E_{CM}-p_1-p_2) > 0.07$.

3.5.2 Topology

The events already passing the Trigger and BGF requirements are further selected using fully reconstructed track informations.

The thrust axis of the event is calculated using all tracks and neutral deposits present in the event. The thrust axis of the event, $\hat{T}$, is defined as the versor maximizing the Thrust, T [70], defined as:

$$T = \frac{\sum_i |\hat{T} \cdot \vec{p_i}|}{\sum_i |\vec{p_i}|} \tag{3.3}$$

where the index i runs over both the neutral deposits and the four tracks present in the event. The event space is divided in two non overlapping hemispheres by the plane normal to the thrust axis containing the interaction region.

The scalar product of the spatial momentum of each of the tracks and $\hat{T}$ is used to assign each track to one of the two hemispheres: tracks with scalar products of the same sign are assigned to the same hemisphere. This topology based selection strongly suppresses background contribution due to Bhabha scattering and di-muon processes.

In all calculations pion mass hypothesis is assumed for all the for reconstructed tracks.

In addition to BGF and Trigger filters, the following requirements are made:

- Number of tracks in ChargedTracks list < 10;

- Thrust is defined with all the BtaCandidates available in ChargedTracks and CalorClusterNeutral (with 50 MeV threshold on the energy of neutrals) lists. In the center-of-mass frame, the event is then divided into 2 hemisphere perpendicular to the thrust axis. The number of neutrals (with energy > 50 MeV) in each hemisphere is required to be < 6, to keep up to 3 π^0 decays from each τ;

- Based upon the number of tracks per hemisphere (Hemisphere 0 and Hemisphere 1), events with three kind of topology are retained:

LOW-multiplicity: (Hemisphere 0, Hemisphere 1) = 11, 21, 20
MID-multiplicity: (Hemisphere 0, Hemisphere 1) = 22, 23, 33
HIG-multiplicity: (Hemisphere 0, Hemisphere 1) = 1N(> 3).

The cumulative efficiencies for the above cuts are shown in table 3.5.2 and the breakdown by topology is shown in table REF.

	L3Trig	BGFTAG	NTrk	NCal50	Topology
DATA	90.6605	64.4385	53.4051	49.6298	37.6282
$\tau\bar{\tau}$	83.8306	68.1208	68.0500	67.9153	65.2014
$\mu\bar{\mu}$	72.8875	68.1625	68.1625	68.1625	67.9750
uds	95.9000	92.9700	78.2600	66.4200	34.5000
$c\bar{c}$	99.0400	97.3400	72.8400	55.7100	23.4500
bb	99.9350	99.4700	46.8550	29.3150	7.1300
Bhabha	67.7694	9.4535	9.4517	9.4517	8.948

Table 3.9: Cumulative efficiencies for data and MC for the skim tagbits.

For the topologies HIG-multiplicity and MID-multiplicity, the combined mass of all particles (ChargedTracks and CalorClusterNeutral candidates > 50 MeV) per hemisphere is required to be > 3 GeV.

For the LOW-multiplicity toplogy, 2 more cuts are applied:

- $\cos\theta$ of the 2 most energetic tracks are required lie within the calorimeter acceptance (-0.76,+0.96);
- ($m_{miss}/\sqrt{s} < 0.2$ || -log($2p_{T,miss}/\sqrt{s}$) < 4.0), where m_{miss} and $\cdot p_{T,miss}$ are the missing invariant mass and transverse momentum.

	TOT	HIG-multiplicity	MID-multiplicity	LOW-multiplicity
DATA	37.6282	5.4713	5.3312	26.8257
bb	7.1300	2.5350	4.3200	0.2750
$c\bar{c}$	23.4500	7.9400	12.9400	2.5700
uds	34.5000	11.3300	16.9500	6.2200
Bhabha	8.9488	1.9350	0.6191	6.3947
$\mu\bar{\mu}$	67.9750	0.2000	0.0500	67.7250
$\tau\bar{\tau}$	65.2014	16.3917	3.0861	45.7236

Table 3.10: Efficiencies on data and MC for the three possible topologies and their sum.

Obviously in the following we will focus our attention to the events which contain a single charged track in the signal hemisphere and, in particular, given the much higher decay rate of the τ to a single charged particle we will focus just on low multiplicity 1-1 events.

3.6 Particle Identification

Information from all *BABAR* sub-detectors contribute to particle identification. A cut-based selection is possible by simply applying cuts on variables related to each sub-detector, however this procedure is not optimal. A multivariate technique, using the same (or even more) variables as input for likelihood, neural network, or bagged decision tree algorithms have a higher discriminating power.

A selector is classified, in *BABAR* analysis, by the method used for the selection, and for different level of efficiency and rejection obtained, modifying selection parameters and variables used. A selector is a category related to a selection method with a certain choice of parameters and selection criteria. For each method a nested system of selectors is provided, with looser selector, with high efficiency but higher mis-identification rates, and hence lower rejection power, or tighter selectors, with lower efficiency and lower mis-identification rates, resulting in better rejection power. Due to the nested nature of looser and tighter selectors, each track satisfying a tighter selector satisfies also the looser selection criteria for the same selection method. For each particle category (electron and muons) many selectors with different selection criteria are available.

3.6.1 Electron Identification

In this analysis the electron selector make use of a bagged decision tree (BDT) [71] multivariate algorithm, using 36 variables as input, in the following the variables used by the algorithm are described, focusing on the variables with the highest discriminating power. The BDT algorithm used to select electrons has been trained on data control samples in order to identify different particles, and to measure mis-identification rates between electrons and other particles that can be revealed by *BABAR* detector. Pure electron samples were obtained from Bhabha scattering, pion samples are obtained looking at kinematically selected $K_S \to \pi^+\pi^-$ and three prong τ decays. Two-body Λ and D^0 decays provide pure samples of proton and charged kaons respectively.

The EMC is the most important source of information for electron identification. Electrons are separated from charged hadrons by looking at the ratio between the energy E deposited in the EMC and the momentum, p, of the track pointing to the cluster measured in the EMC. For an electron the E/p ratio should be compatible with unity, since the electron is expected to deposit all its energy inside the calorimeter volume. Hadrons will appear as minimum ionizing particles in the EMC, or at most they will deposit part of their energy after hadronic interaction in the crystals. although a small amount of energy is deposited by hadrons in EMC crystals E/p ratio is expected to be small.

Shower energy, Lateral shower shape from EMC are also used for e/h separation. These variables along with the E/p make it possible to measure the e/h separation using only EMC information. The typical electron efficiency and pion mis-identification rate as a function of track momentum and polar angle obtained from EMC only is shown in Fig. 3.3. The efficiency for electron identification is measured using data control samples containing radiative Bhabha scattering and two photon $\gamma\gamma \to e^+e^-$ processes. The pion mis-identification probability is measured using data control samples containing τ decays in three charged particles.

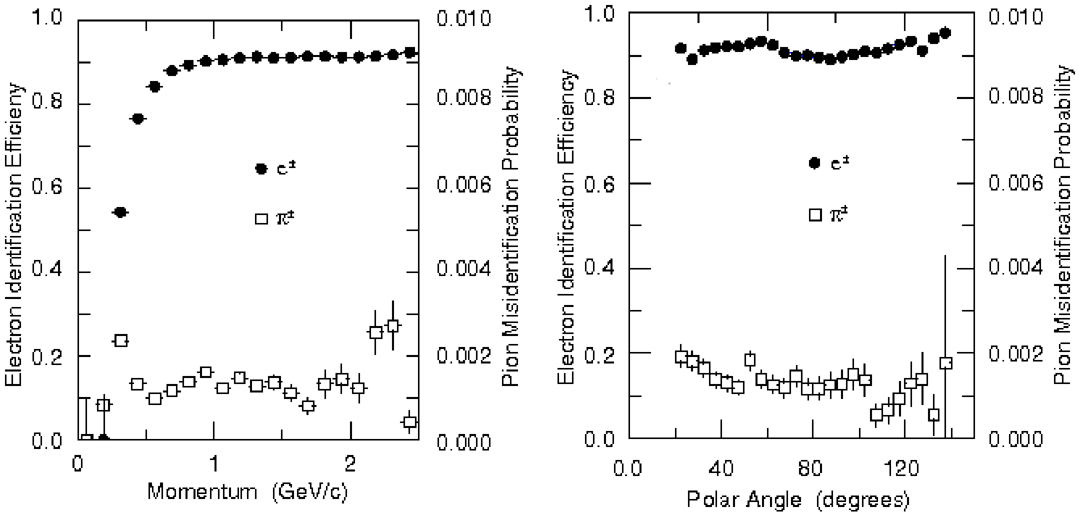

Figure 3.3: Electron efficiency and pion mis-identification probability as a function of momenta (left) and track polar angle (right)

To further refine electron identification other variables are used to build the bagged decision tree used in this analysis: the specific energy loss, dE/dx, in the DCH and the DIRC Čerenkov angle, $\theta_{\check{C}}$, represent the other main variables for electron-hadron separation. These variables offer a good e/π separation over a wide range of momenta, even using a cut-based selection.

Track selection criteria are tightened when electron are selected to ensure a reliable momentum measurement and identification efficiency. The selection requires a transverse momentum $p_T > 0.1\,\mathrm{GeV}/c$, a number of drift chamber hits $N_{DCH} \geq 12$, and then electron candidates are required to have a momentum in the laboratory frame, calculated in electron mass hypothesis, $p_{LAB} > 0.5\,\mathrm{GeV}/c$.

Another set of variables used as input are represented by the likelihood ratios[72], defined as:

$$F_{\xi'} = \frac{f_{\xi'} L(\xi')}{\sum_{\xi} f_{\xi} L(\xi)} \tag{3.4}$$

where $\xi \in \{e, \pi, K, p\}$ and the relative particle fraction are such as $f_e : f_\pi : f_K : f_p = 1 : 5 : 1 : 0.1$. The likelihood $L(\xi)$ is defined as:

$$L(\xi) = P_{SVT}(dE/dx|\xi) \cdot P_{DCH}(dE/dx|\xi) \cdot P_{DRC}(\theta_{\check{C}}) \tag{3.5}$$

These likelihood ratios depend only on tracking sub-systems and DIRC. Other variables used are:

- particle momentum and charge;
- polar and azimuthal angle of the track when the track enters inside the EMC volume;
- tracking system hit information, such as last DCH layer hit and number of hits in SVT;

- number of crystal with energy deposit associated to the track;
- other shape variables for EMC shower (Zernike moments, ratios of energies between central crystals and the first neighbors, longitudinal shower depth).

The BDT algorithm provides a reliable and efficient selector for e/π separation, and it shows better performances than the likelihood algorithm [72], used in previous *BABAR* analysis [59], over all momenta and polar angle regions electron identification efficiency while the pion mis-identification rate is slightly worse, as it is shown in Fig. 3.4. To achieve higher efficiencies the BDT algorithm was used instead of likelihood selector, despite the higher mis-identification rate, since pion contamination does not constitute a major source of contribution in this analysis.

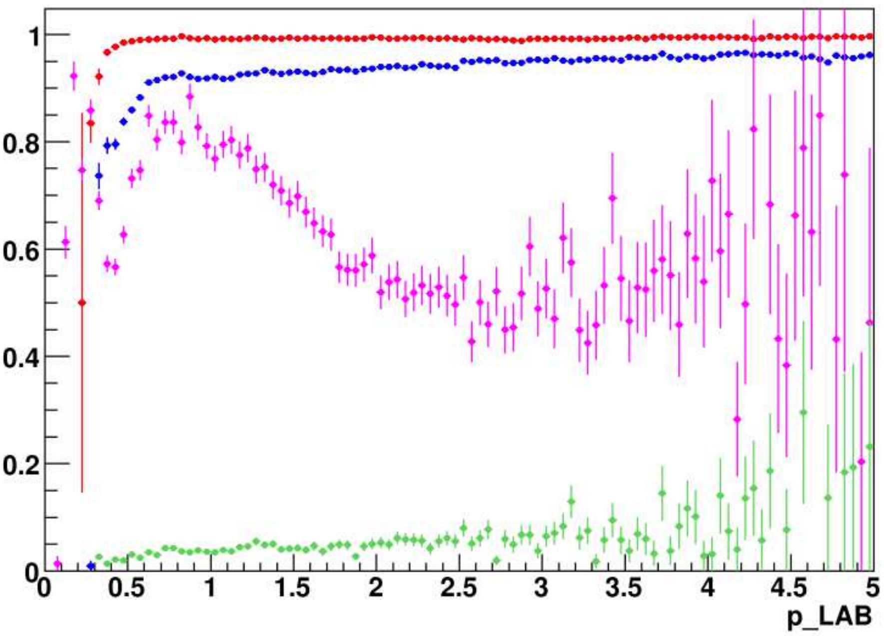

Figure 3.4: Selection efficiency for BDT electron selector (red) and for Likelihood based selector (blue) as function of track momentum. Pion mis-identification rate is shown as a function of the track momentum, in magenta for BDT selector, and in green for Likelihood based selector.

3.6.2 Muon Identification

The first level of muon identification, as used in online monitoring, is coming from the measurement of the number of traversed interaction lengths in the detector for a track. The projected intersection of a track in the IFR is computed and, for each readout plane, all clusters, made of hits in one of the two readout coordinates, are associated with the traversing track if they are detected near the intersection predicted extrapolating the track trajectory from the inner tracker system. Additional π/μ discrimination power can be obtained by observing the average number and r.ms. of the distribution of the

IFR hits in each layer: the average number of hits is expected to be larger for pions, producing an hadronic interaction, especially in the innermost layers, than for muons. Other variables employed for π/μ discrimination use cluster distribution shapes in the IFR, all the aforementioned variables are used in different algorithms which use the variables as input and give out a single discriminating variable as output. To test muon selection performance data control samples are used, composed of $\mu\mu ee$ and $\mu\mu\gamma$ final states, produced in e^+e^- scattering and pion control samples from τ and K_S decays. The average muon identification rate and pion mis-identification rates are measured as a function of track momenta and track reconstructed polar angle, and are shown in Fig. 3.5

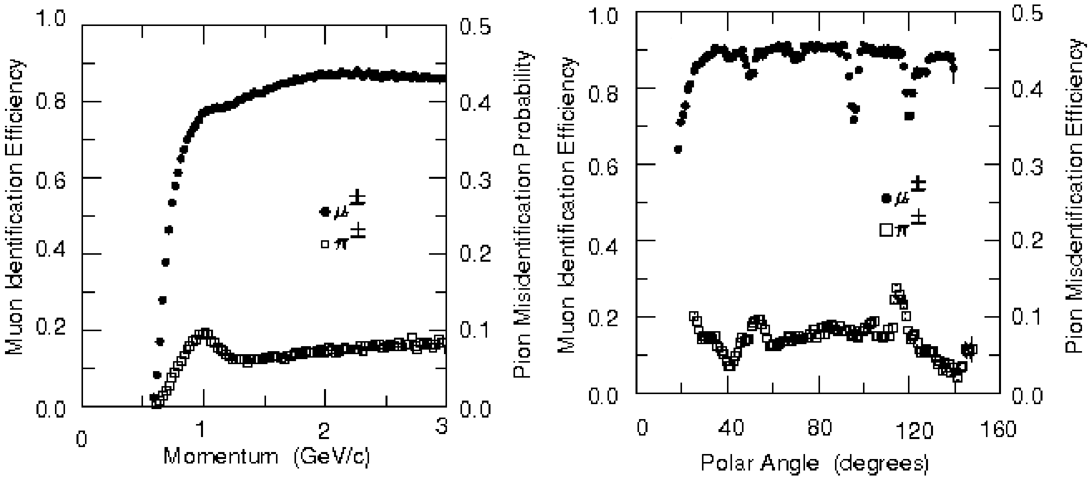

Figure 3.5: Muon identification efficiency and pion mis-identification rate, as a function of track reconstructed momentum (left) and track polar angle(right)

Due to the changes in RPC performances over the years and the subsequent installation of LST detectors the overall efficiency of the detector changed widely over the data-taking period, in Fig.3.6 are shown the performance of the system in different data-taking periods for tracks of high and low momenta, and for the forward end-cap and barrel.

In this analysis all tracks considered muon candidates are identified using internal tracking systems information along IFR information to build variables. The variables with the higher π/μ discrimination power used for muon selection are:

- tracking variables, measured by DCH and SVT: transverse momentum p_T, number of DCH hits N_{DCH}, polar angle in laboratory frame, θ_{LAB}, and track momentum in laboratory frame p_{LAB};

- energy deposited in the EMC, which is required to be consistent with minimum ionizing particle hypothesis;

- number of IFR layers hit associated with the track;

- total number of interaction lengths traversed by the particle from the IP to the last layer hit in the associated IFR cluster;

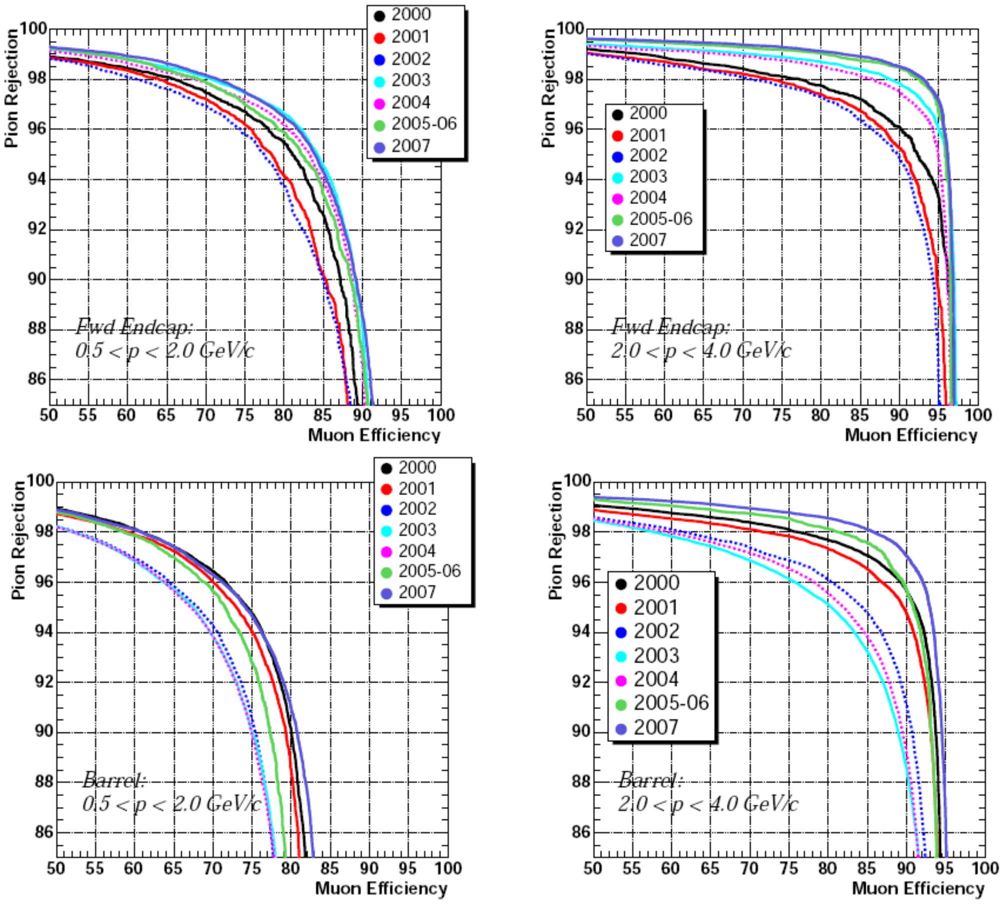

Figure 3.6: Muon efficiency vs. pion rejection as measured from neural network selection algorithms as a function of time (different colors), and track momenta, low momenta on the left side high momenta on the right side. The topmost figures represent muon identification capabilities for forward end cap while on bottom the performance of the barrel is shown.

- difference between the measured number of interaction lengths and the expected number of interaction length estimated for a muon of the same momentum and angle.
- average number and r.m.s. of the distribution of IFR hits per layer;
- *continuity* of IFR cluster hits, defined as $T_C = \frac{N_L}{L-F-1}$, where L and F are the last and first layers with hit and N_L is the number of layers with at least one hit; T_C is expected to be 1 for ideal muons and is expected to be smaller for hadrons;
- χ^2 of cluster centroids compared to the extrapolated charged tracks.

The performance of muon selection is tested on samples of muons from $\mu\mu ee$ and $\mu\mu\gamma$ samples for efficiency purposes, while pion contamination is studied using 3-prong τ decay and $K_S \to \pi^+\pi^-$ decay control samples.

A cut based selector for muons is not optimal, given the large number of variables under study and the complex geometry of tracks passing through the IFR. In order to fully exploit information recorded by *BABAR* detector it is natural to use multivariate algorithms like neural networks or bagged decision trees to put all information together to create a single discriminating variables. Both neural network and BDT algorithms have been implemented to create efficient selectors. The best performance for muon identification has been obtained the output of a BDT using 30 variables as input, implemented with StatPatternRecognition package[73]. Fig.3.7 shows comparison between the neural network selector used in [59] and the new BDT algorithm.

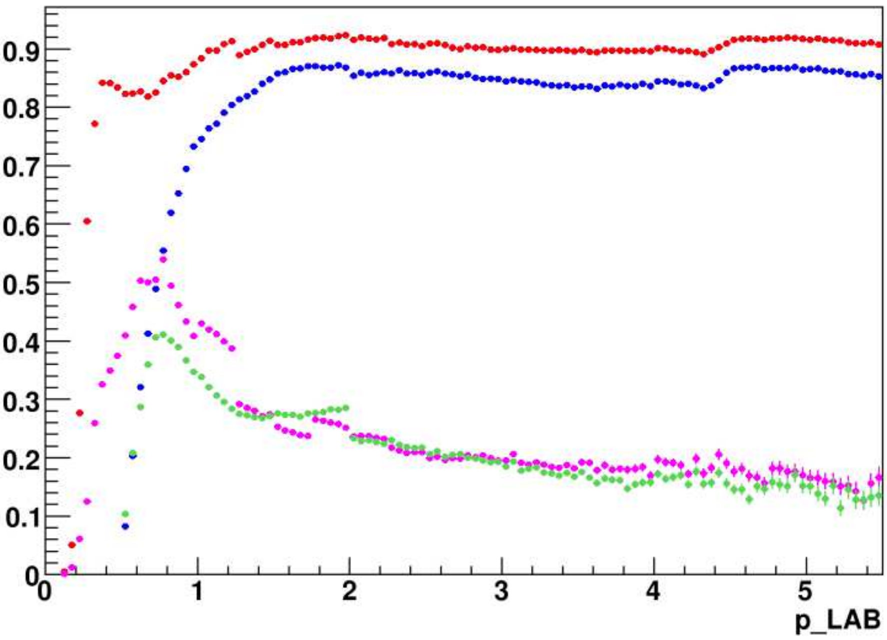

Figure 3.7: Selection efficiency for BDT muon selector (red) and for Likelihood based selector (blue) as function of track momentum. Pion mis-identification rate is shown as a function of the track momentum, for BDT selector (magenta) , and in for Likelihood based selector (light green).

The major improvements between the neural network and BDT based algorithms arise from a better parametrization of detector response, in particular dE/dx in DCH and SVT parametrization, use of more advanced statistical techniques, and from the use of 22 new variables with lower discriminating power than the 8 used in the neural network, but nonetheless adding more information useful for selection purposes. The new variables include:

- number of signal and background photons in the DIRC;
- last layer containing hits in DCH (mainly used to identify kaon and pion in-flight decays);
- DIRC Čerenkov angle, $\theta_{\check{C}}$;
- full set of EMC cluster-shape quantities, as done for electron selection;

- longitudinal EMC shower depth;
- use of geometry to predict *dead spots* in detector acceptance.

3.6.3 PID Tweaking

Particle identification selectors show a different efficiency for data and MC samples. The different behavior between data and MC is caused mainly by detector response modeling and detector material model. To reduce systematic errors introduced by these discrepancies the MC is corrected using a correction factor, obtained measuring the efficiency for data control samples selected without the use of PID information.

Particle identification efficiency and mis-identification probability for a given track are strongly dependent on the particle kinematics, and also discrepancies between data and MC change with particle momenta, polar, and azimuthal angle of the track under study as shown in Fig. 3.8 for electron selectors, and Fig.3.9 for muon selectors.

Possible discrepancies between data and MC resolution may introduce a systematic contribution on signal efficiency; discrepancies between data and MC PID efficiencies have been accounted for using the weights from the PID tables with the tweaking technique: first, the selection procedure as defined by the selector is is run then, with the help of PID-efficiency tables derived from data and MC (where MC has been treated in the same way as data), the second step is either rejecting an accepted track with probability

$$\epsilon_{data}/\epsilon_{MC} \text{ if } \epsilon_{data} < \epsilon_{MC} \tag{3.6}$$

or accepting a rejected track with probability

$$(\epsilon_{data} - \epsilon_{MC})/(1 - \epsilon_{MC}) \text{ if } \epsilon_{data} > \epsilon_{MC}. \tag{3.7}$$

A tweaking scheme of the MC events ensures that MC accurately reproduces PID efficiency for all tracks under study. Data control samples of pure, kinematically selected (i.e. without using PID selectors), particles are used to assign to each track, given the track reconstructed momentum, polar, and azimuthal angle, the probability to either be correctly identified or mis-identified as another particle. In this way MC particle identification information is disregarded, having large discrepancies in some kinematic regions, the PID (mis-)identification probability obtained from the data control samples is assigned to MC tracks. By using this weighting there is need to correct for differences between data and MC.

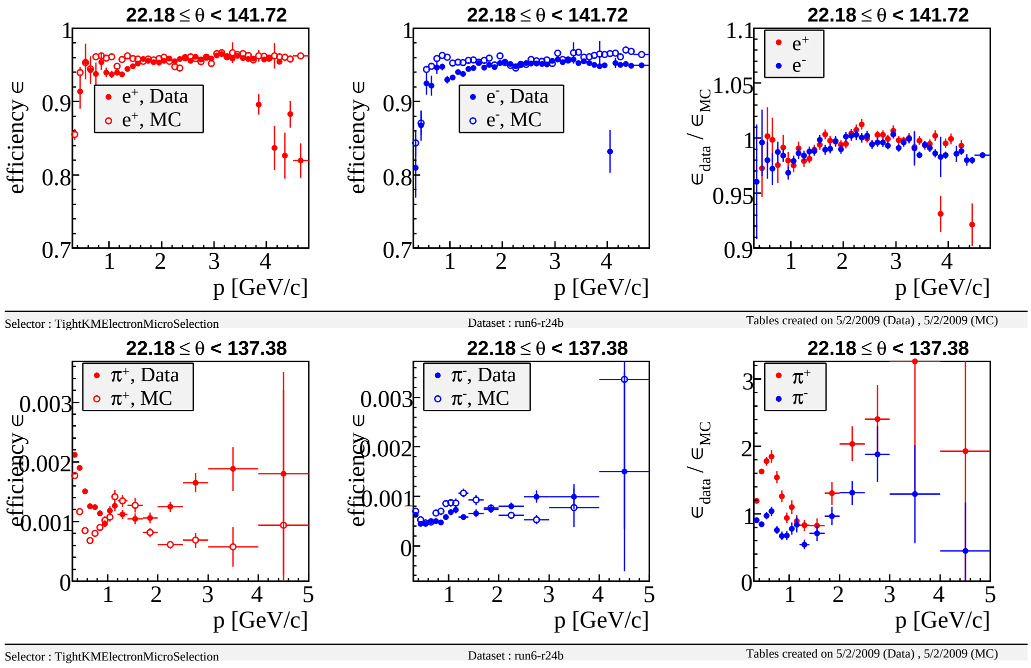

Figure 3.8: Comparison between data and MC efficiency for electron selector as a function of momentum (on top), and comparison between data and MC π selection efficiency for electron selector as function of momentum (on bottom)

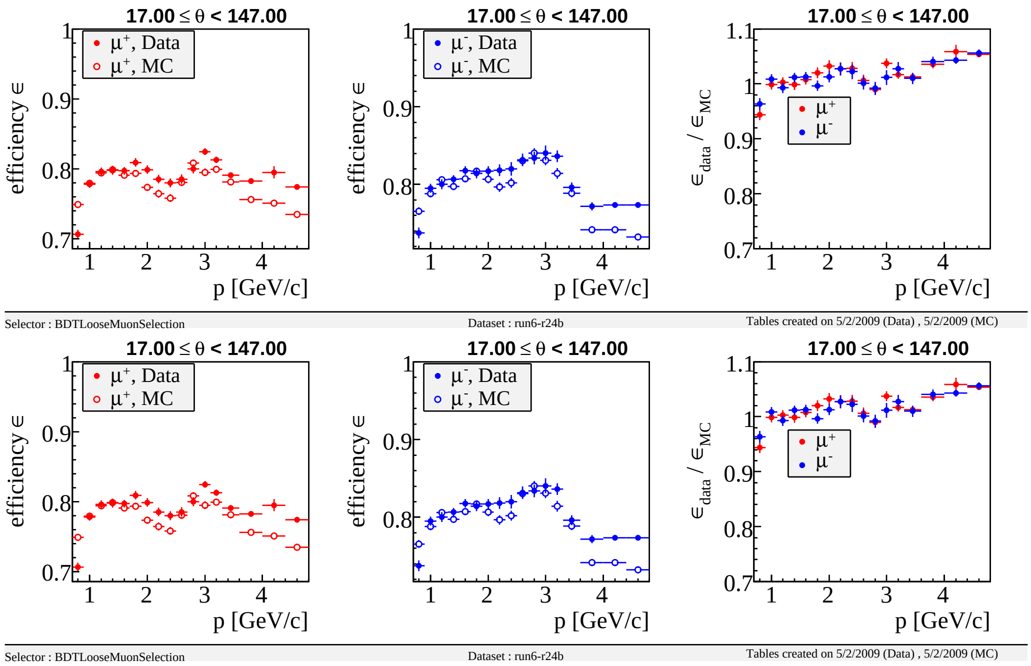

Figure 3.9: Comparison between data and MC efficiency for muon selector as a function of momentum (on top), and comparison between data and MC π selection efficiency for muon selector as a function of momentum (on bottom)

3.7 Event Reconstruction

After having defined the list of tracks and neutrals, applied the PID algorithms and reconstructed the event topology, we apply specific cuts to reconstruct $\tau \to l\gamma\nu\bar{\nu}$ as well as to reduce background contamination (especially non simulated backgrounds as Bhabha and two-photon production) and improve reconstruction quality.

In order to preselect our sample we apply the following cuts after the skim:

- Tracks:
  Every event should contain exactly 2 charged tracks; The additional following cuts are applied to charged tracks:
  - Transverse momentum $p_T > 0.3$ GeV. This reduces uncertainty and improves overall track quality.
  - Polar angle of each track $-0.75 < \cos\theta < 0.95$ in order to match the corresponding values of the PID tables.
  - Distance of closest approach (DOCA): the minimum distance between the interaction point (IP) and track helix should be less than 1 cm in the XY plane(transverse to the beams) and less than 3 cm in the beam direction (z-axis).
  - Number of hits in the drift chamber: there should at least 20 hits in the DCH associated wit the track, this improves track quality.
- Missing momentum:
  The total event momentum computed using all tracks and neutral deposits in the event should satisfy the following requirements:
  - Total missing momentum $p_{T,miss} > 0.5$ GeV.
  - Cosine of missing momentum $-0.75 < \cos\theta_{T,miss} < 0.99$. This cut is particularly useful to reject low p_T QED backgrounds such as $e^+e^- \to \gamma\gamma$ and radiative Bhabha events as well as beam related backgrounds.
- Charge Conservation:
  The total charge of the previously selected tracks has to sum up to zero.
- Reconstructed 1-1 topology:
  For each event, we compute the thrust axis using the tracks 3-momenta and the most energetic reconstructed neutral 3-momentum: a plane perpendicular to the thrust axis passing through the interaction point defines two hemispheres, the tag and the signal hemisphere. The scalar product of the particle momentum with the thrust axis determines to which hemisphere the particle belongs, we thus require that both the tag hemisphere and the signal hemisphere contain exactly one particle, i.e. the angle between the tag track and the signal track is greater than $\pi/2$. The magnitude of the thrust is required to be $0.75 < T < 0.995$, where the upper cut is set in order to reject typical QED backgrounds, i.e $\mu^+\mu^-$ production and Bhabha scattering, while the lower cut rejects most hadronic high-multiplicity events.
- Neutrals:
  - Minimum energy $E > 50$ MeV
  - Minimum number of crystals per cluster is 2

– Lateral momentum of the shower $0.001 < p_L < 0.8$

– We reject events with more than 5 neutral clusters and/or more than 2 $\pi^0 s$

– We also reject events with neutral clusters with less then 110 MeV if they are closer then 25 cm from a a charged track. This helps to suppress background from "split-off"'s i.e. neutral clusters, associated mainly with pions, caused by hadronic interactions inside the EMC

- K_s and conversions:
  events containing reconstructed K_ss and/or tracks originating from converted photons are rejected. The selection criteria for K_s and converted photons are shown in table 3.11.

Variable	K_s	Conversions
Invariant mass of tracks	$-0.007 < (m - m_K) < 0.007$ (GeV)	$0 < m < 0.03$ (GeV)
Distance of V_0 to IP	$0.5 < d_V < 80$ (cm)	$1.5 < d_V < 80$ (cm)
DOCA of track pair	<0.75 (cm)	<0.75 (cm)
Vertex probability of tracks	>0.02	>0.02
Primary pointing	>0.998	>0.998
# of DCH hits before V_0	<3	<3

Table 3.11: V0BtaTrack track requirements for K_s and conversion lists.

Cut	Efficiency (%)
Reject converted photons	96.63
Reject events with K_S	93.89
Number of charged tracks	70.46
Zero charge	70.41
Number of π^0	62.10
Minimum track p_T	61.86
Thrust Magnitude	55.67
Minimum event p_T	52.74
1 track per hemisphere	50.46

Table 3.12: Efficiencies (relative to the Tau11 skim) for the various preselection cuts.

After the preliminary cuts we retain only events with one charged track and one neutral on the signal side, while depending on the tagging mode we apply different requirements on the tagging side:

- e, π and μ tags:
  at most one neutral deposit in the EMC is admitted on the tag side.

- $\pi\pi^0$ tags:
  exactly 2 neutrals and 1 reconstructed π^0 in addition to the charged track are requested in the tagging hemisphere.

- $\pi\pi^0\pi^0$ tags:
  exactly 4 neutrals and 2 reconstructed π^0s along with 1 charged track are requested on tagging side.

pi^0s are defined starting from the photon list as defined in section 3.4 requiring for any pair of photon candidates $P_{CM} > 0.45$ GeV, $0.115 < m_{\gamma\gamma} < 0.150$ GeV.

For all three tagging modes, in order to reduce the data sample size before final selection, we further impose the maximum distance between the track and the photon candidate in the signal hemisphere on the inner surface of the EMC to be less than 100 cm.

Signal Hemisphere	eKMSuperTight
Tagging Hemisphere	(muBDTTight or piKMTight) and (!eKMLoose)

Table 3.13: PID scheme for $\tau \to e\nu\bar{\nu}$ for all tagging modes.

Signal Hemisphere	muBDTVeryTight
Tagging Hemisphere	(eKMLoose or piKMTight) and (!muBDTLoose)

Table 3.14: PID scheme for $\tau \to \mu\nu\bar{\nu}$ for all tagging modes.

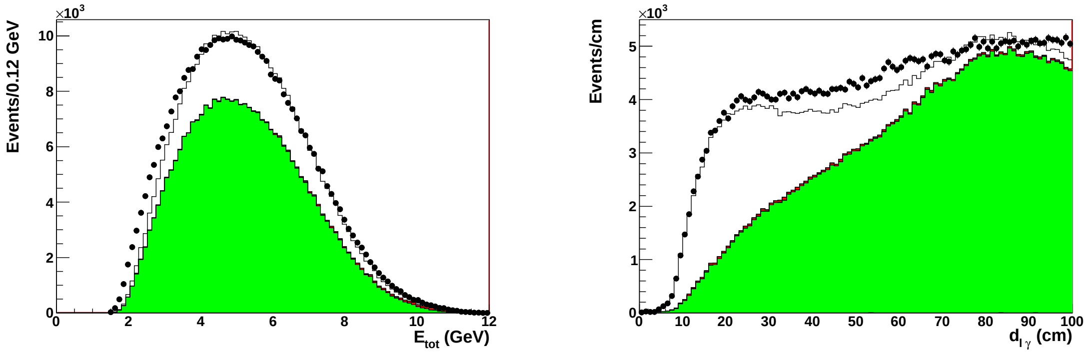

Figure 3.10: Total reconstructed energy in the event for radiative τ decay into a muon after preselection. The black dots are data, the green bars are generic (non signal) τ MC decays while the white bars are $\tau \to \mu\gamma\nu\bar{\nu}$ decays.

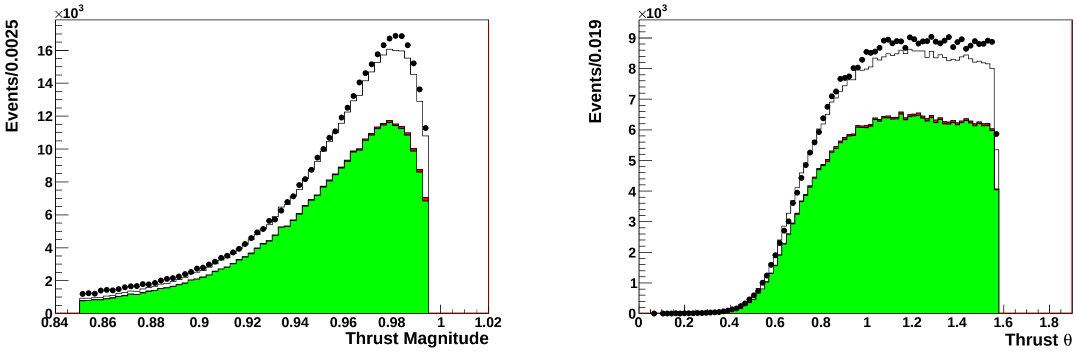

Figure 3.11: Thrust magnitude and polar angle in the event for radiative τ decay into a muon after preselection. The black dots are data, the green bars are generic (non signal) τ MC decays while the white bars are $\tau \to \mu\gamma\nu\bar{\nu}$ decays.

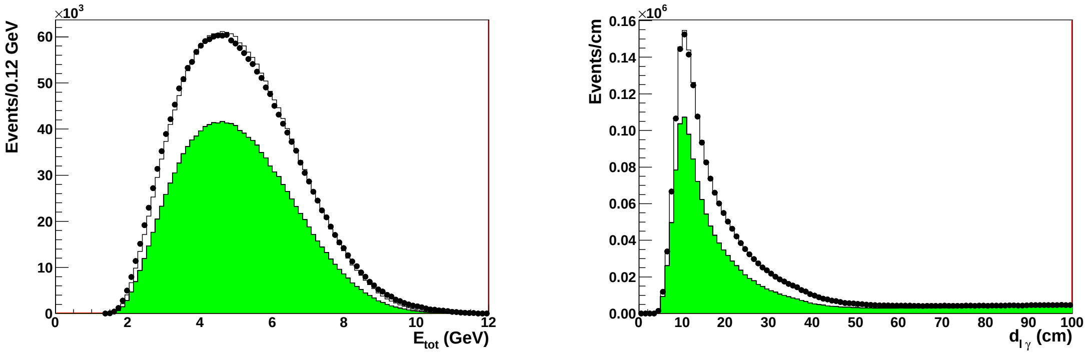

Figure 3.12: Total reconstructed energy in the event for radiative τ decay into an electron after preselection. The black dots are data, the green bars are generic (non signal) τ MC decays while the white bars are $\tau \to e\gamma\nu\bar{\nu}$ decays.

3.8 MC Correction

After applying the preselection criteria significant discrepancies are seen between the data and MC samples, as shown in the previous section. To improve the agreement between the two samples we impose further preselection requirements; this requirements are mostly empirical and, in general, have no direct physical meaning. The aim is simply to reduce discrepancies which are mostly related to the detector simulation and to unsimulated backgrounds. Furthermore, to avoid bias, we do not apply criteria to variables and regions which are especially sensitive to distributions of the signal channels.

To improve MC reproduction of data we further impose:

- $\tau \to e\gamma\nu\bar{\nu}$:
  Total reconstructed energy $E_{tot} < 9$ GeV
  Missing momentum of charged tracks $p_{tot,miss} > 1.5$ GeV
  Thrust magnitude $T > 0.9$
  Thrust angle $\theta_T < 1.5$ rad
  Cosine of polar angle of the charged tracks $\cos\theta_{p_1}, \cos\theta_{p_2} < 0.8$

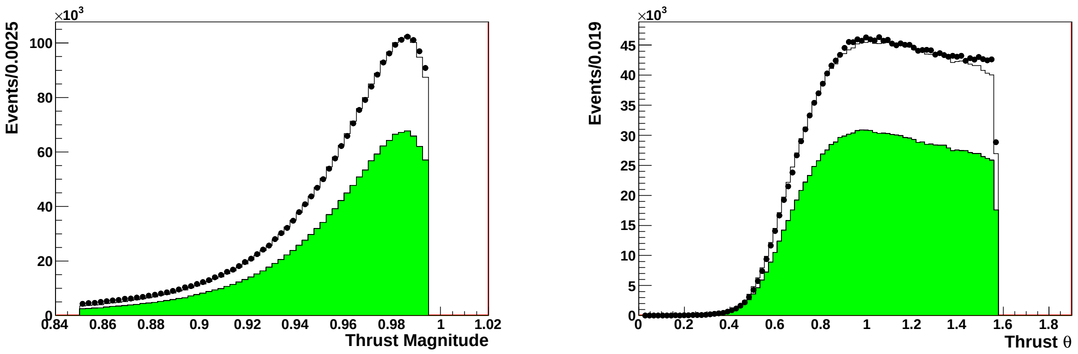

Figure 3.13: Thrust magnitude and polar angle in the event for radiative τ decay into an electron after preselection. The black dots are data, the green bars are generic (non signal) τ MC decays while the white bars are $\tau \to e\gamma\nu\bar{\nu}$ decays.

	$\tau \to e\gamma\nu\bar{\nu}$	$\tau \to \mu\gamma\nu\bar{\nu}$
MC	2104900.9	380188.0
Data	2124230	396139
$\tau \to \mu\gamma\nu\bar{\nu}$	–	88851.7
$\tau \to e\gamma\nu\bar{\nu}$	688895.0	–
$\tau\bar{\tau}$ (SP3429) bkg	1415532.0	288276.0
$\mu\bar{\mu}$ (SP3981)	247.8	2846.5
uds (SP998)	23.8	104.7
$c\bar{c}$ (SP1005)	55.1	42.7
$b\bar{b}$ (SP1235+SP1237)	35.2	27.3
Bhabha	112.0	0.0

Table 3.15: Number of signal and background events for data and MC (normalized to data) after preselection. For the signal modes the whole sample is considered without cuts on the minimum energy.

- $\tau \to \mu\gamma\nu\bar{\nu}$:
  Total reconstructed energy $E_{tot} > 3.5$, $E_{tot} < 9$ GeV
  Thrust magnitude $T > 0.9$
  Thrust angle $\theta_T < 1.525$ rad

Final preselection efficiencies and number of events passing preselection requirements are given in tables 3.8-3.8.

	$\tau \to e\gamma\nu\bar{\nu}$	$\tau \to \mu\gamma\nu\bar{\nu}$
$\tau \to \mu\gamma\nu\bar{\nu}$	–	1.96(%)
$\tau \to e\gamma\nu\bar{\nu}$	3.04 (%)	–
Data	3.1×10^{-2} (%)	5.9×10^{-3} (%)
$\tau\bar{\tau}$ (SP3429) bkg	0.36 (%)	7.3×10^{-2} (%)
$\mu\bar{\mu}$ (SP3981)	5×10^{-5} (%)	5.7×10^{-4} (%)
uds (SP998)	2.6×10^{-6} (%)	1×10^{-5} (%)
$c\bar{c}$ (SP1005)	1×10^{-5} (%)	8×10^{-6}
$b\bar{b}$ (SP1235+SP1237)	8×10^{-6} (%)	6×10^{-6} (%)
Bhabha	$< 10^{-8}$	$< 10^{-8}$

Table 3.16: Preselection efficiencies for signal and background events for data and MC. For the signal modes the whole sample is considered without energy cut-off.

	$\tau \to e\gamma\nu\bar{\nu}$	$\tau \to \mu\gamma\nu\bar{\nu}$
MC	1746035.44	282368
Data	1748573	282005
$\tau \to \mu\gamma\nu\bar{\nu}$	–	69900.7
$\tau \to e\gamma\nu\bar{\nu}$	573686.0	–
$\tau\bar{\tau}$ (SP3429) bkg	1172180.0	211281.0
$\mu\bar{\mu}$ (SP3981)	84.9	1117.0
uds (SP998)	8.9	25.5
$c\bar{c}$ (SP1005)	33.8	27.3
$b\bar{b}$ (SP1235+SP1237)	21.6	17.4
Bhabha	20.4	0.0

Table 3.17: Number of data and MC events (normalized to data) for signal and background after preselection and additional cuts. For the signal modes the whole sample is considered without energy cut-off.

	$\tau \to e\gamma\nu\bar{\nu}$	$\tau \to \mu\gamma\nu\bar{\nu}$
$\tau \to \mu\gamma\nu\bar{\nu}$	–	1.54(%)
$\tau \to e\gamma\nu\bar{\nu}$	2.53 (%)	–
Data	2.6×10^{-2} (%)	4.2×10^{-3} (%)
$\tau\bar{\tau}$ (SP3429) bkg	0.30(%)	5.3×10^{-2} (%)
$\mu\bar{\mu}$ (SP3981)	1.7×10^{-5} (%)	2.3×10^{-4} (%)

Table 3.18: Preselection efficiencies on the refined sample for signal and most relevant background for data and MC. For the other background modes the change in efficiency is negligible. For the signal modes the whole sample is considered without cuts on the minimum energy.

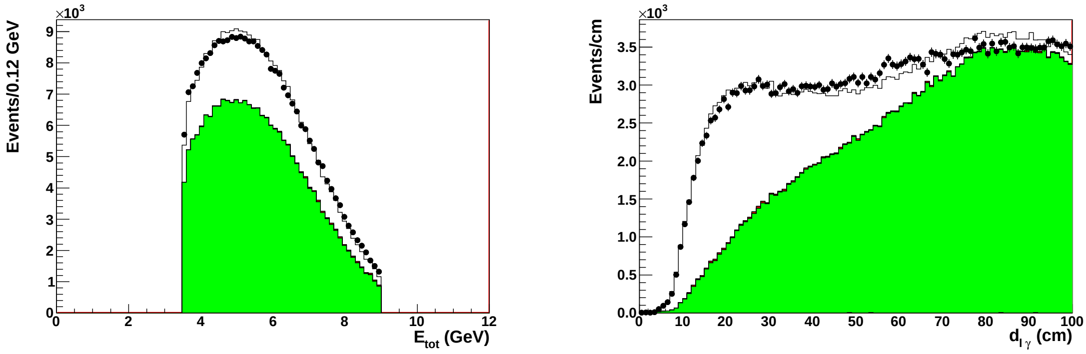

Figure 3.14: Total reconstructed energy in the event for radiative τ decay into a muon after preselection and additional refinement cuts. The black dots are data, the green bars are generic (non signal) τ MC decays while the white bars are $\tau \to \mu\gamma\nu\bar{\nu}$ decays.

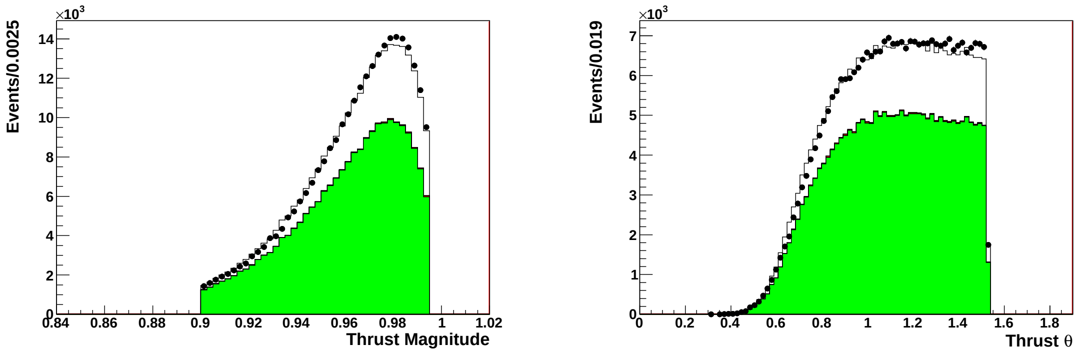

Figure 3.15: Thrust magnitude and polar angle in the event for radiative τ decay into a muon after preselection and additional refinement cuts. The black dots are data, the green bars are generic (non signal) τ MC decays while the white bars are $\tau \to \mu\gamma\nu\bar{\nu}$ decays.

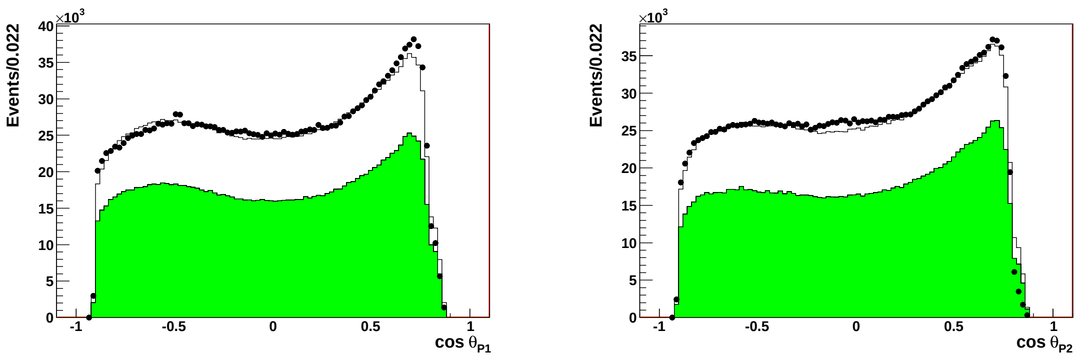

Figure 3.16: Polar angle of charged tracks for radiative τ decay into an electron after preselection before additional refinement cuts. The black dots are data, the green bars are generic (non signal) τ MC decays while the white bars are $\tau \to e\gamma\nu\bar{\nu}$ decays.

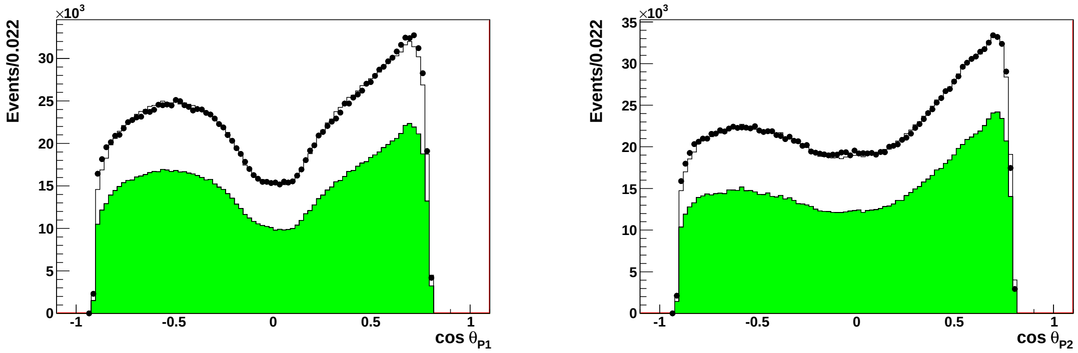

Figure 3.17: Polar angle of charged tracks for radiative τ decay into an electron after preselection after refinement cuts. The black dots are data, the green bars are generic (non signal) τ MC decays while the white bars are $\tau \to e\gamma\nu\bar{\nu}$ decays.

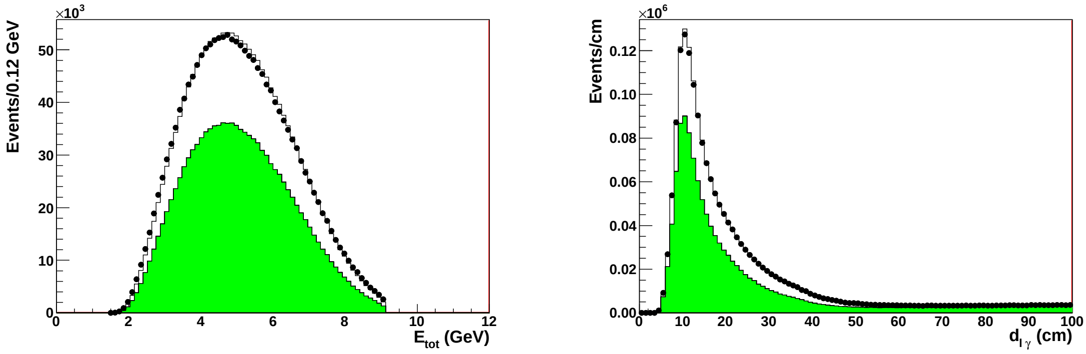

Figure 3.18: Total reconstructed energy in the event for radiative τ decay into an electron after preselection and additional refinement cuts. The black dots are data, the green bars are generic (non signal) τ MC decays while the white bars are $\tau \to e\gamma\nu\bar{\nu}$ decays.

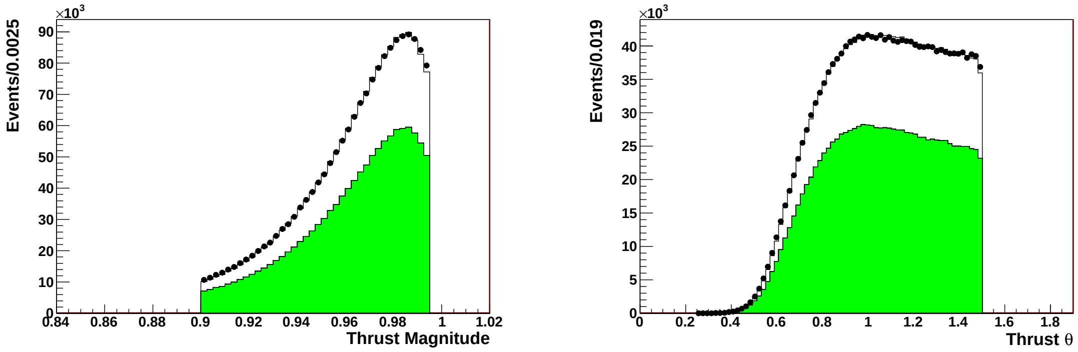

Figure 3.19: Thrust magnitude and polar angle in the event for radiative τ decay into an electron after preselection and additional refinement cuts. The black dots are data, the green bars are generic (non signal) τ MC decays while the white bars are $\tau \to e\gamma\nu\bar{\nu}$ decays.

Chapter 4

Selection and Background Estimation

After preselection the sample is still dominated by generic τ decay background events. In this chapter we will define the final selection criteria for the two signal modes. As shown previously, all existing measurements are limited by the systematic error; since our sample has much more statistics with respect to existing measurements our first aim is to reduce the systematic contribution. In section 4.1 we will introduce an appropriate figure of merit to optimize our selection accounting for systematic effects. In the following sections we will focus on the kinematics of $\tau \rightarrow l\gamma\nu\bar{\nu}$ and define a set of variables suitable to discriminate signal from background. This will be done separately for the two signal channels because, as we will see, the type of backgrounds which affect the two modes is significantly different. For each channel we will show how our figure of merit behaves for different choices of the selection criteria. We will also compare our optimization method with the standard one used to maximize the signal to noise ratio. Finally we will introduce the cut on the minimum value of the photon energy already discussed in chapter 3, estimate our efficiency in the $E*_\gamma < E*_{min}$ region and correct the actual signal efficiency.

4.1 Optimization strategy

The quantity we want to measure is given by

$$BR_{\tau\rightarrow X\gamma\nu\bar{\nu},X=e,\mu} = \frac{N_{obs} - N_{bkg}}{2\epsilon_X \sigma_{\tau\tau}\mathcal{L}} \tag{4.1}$$

where N_{obs} is the number of candidate events, N_{bkg} is the number of background events, evaluated from MC, ϵ_X is the selection efficiency, $\sigma_{\tau\tau}$ is the τ-pair production cross section and $\mathcal{L}$ the integrated luminosity. Using the fact that $\epsilon_X = N_{sig}/N_{sig,tot}$, where $N_{sig,tot} = \mathrm{BF}_{sig}N_{\tau\tau}$ and $N_{\tau\tau} = 2\sigma_{\tau\tau}\mathcal{L}$ equation 4.1 can be rewritten as

$$\Delta(BR_{\tau\rightarrow X\gamma\nu\bar{\nu},X=e,\mu}) = \Delta(\frac{N_{obs} - N_{bkg}}{N_{sig}})BR_{\tau\rightarrow X\gamma\nu\bar{\nu},X=e,\mu} \tag{4.2}$$

and, since we want to minimize the relative error on the branching fraction, our figure of merit is given by

$$\frac{\Delta(BR_{\tau\to X\gamma\nu\bar{\nu},X=e,\mu})}{BR_{\tau\to X\gamma\nu\bar{\nu},X=e,\mu}} = \Delta(\frac{N_{obs}-N_{bkg}}{N_{sig}}). \tag{4.3}$$

At this point if one neglects systematic contributions, the only error contributing to 4.3 is the poissonian error on N_{obs}, which rewriting $N_{obs} = N_{sig}+N_{bkg}$ leads to the maximization of the well known quantity

$$FOM = \frac{N_{sig}}{N_{sig+N_{bkg}}}. \tag{4.4}$$

In our case however the aim is to define the optimization procedure in such a way as to minimize the total error and consequently we return back to 4.3 and write the right hand side as

$$\frac{\Delta(BR_{\tau\to X\gamma\nu\bar{\nu},X=e,\mu})}{BR_{\tau\to X\gamma\nu\bar{\nu},X=e,\mu}} = \sqrt{\frac{\Delta(N_{obs})^2}{N_{sig}^2}+\frac{\Delta(N_{bkg})^2}{N_{sig}^2}+\frac{\Delta(N_{sig})^2}{N_{sig}^4}}. \tag{4.5}$$

Now we assume systematic the error on MC signal and background events to be linear in the same quantities, i.e. $\Delta N_{bkg} = \alpha N_{bkg}$ and $\Delta N_{sig} = \beta N_{sig}$ while N_{obs} has the usual statistic error, so

$$\frac{\Delta(BR_{\tau\to X\gamma\nu\bar{\nu},X=e,\mu})}{BR_{\tau\to X\gamma\nu\bar{\nu},X=e,\mu}} = \sqrt{\frac{N_{obs}}{N_{sig}^2}+\frac{\alpha^2 N_{bkg}^2}{N_{sig}^2}+\frac{\beta^2}{N_{sig}^2}} \tag{4.6}$$

which, simplifying, leads to the minimization of

$$\frac{\Delta(BR_{\tau\to X\gamma\nu\bar{\nu},X=e,\mu})}{BR_{\tau\to X\gamma\nu\bar{\nu},X=e,\mu}} = \frac{1}{N_{sig}}\sqrt{N_{obs}+\alpha^2 N_{bkg}^2+\beta^2} \tag{4.7}$$

or, as used, in later sections to the maximization of

$$FOM = \frac{N_{sig}}{\sqrt{N_{obs}+\alpha^2 N_{bkg}^2+\beta^2}}. \tag{4.8}$$

Now that we have defined our figure of merit we optimize our selection cuts as follows

- a set a initial values for all selection variables is defined
- a loop over a wide range of values of cuts for each variable is executed retaining the other cuts fixed st their initial value
- the cut on variable giving most improvement to our FOM is set to the new value and the loop is started again
- the procedure is repeated until all cuts are set and the result converges

To check that the procedure is not biased we repeat the algorithm with random initial values for the various cuts in order to prove the the algorithm converges always to the same values. For the results quoted in the following sections (tables 4.2 and 4.3.2) refer to the systematic contributions reported in table 5.4.

4.2 Selection of $\tau \to \mu\gamma\nu\bar{\nu}$

4.2.1 Kinematics and backgrounds

For $\tau \to \mu\gamma\nu\bar{\nu}$ after preselection the major background is represented by $\tau \to \mu\nu\bar{\nu}$ decays in which a photon coming either initial state radiation (ISR), final state radiation (FSR), π^0 decay in the tag hemisphere or machine background is measured in the EMC close to the charged track. The second major background source is represented by $\tau \to \pi(n)pi^0\nu$ decays in which the pion is misidentified as muon. $e^+e^- \to \mu^+\mu^-$ and other τ decays contribute to a lesser amount. Background from other physics processes are negligible. To refine the selection one can take advantage, as was mentioned before, of the peculiar kinematics of τ radiative decays and in particular of the fact that, in the τ rest frame, the photon tends to be emitted in the direction of the outgoing lepton. Unfortunately due to the presence of two neutrinos in the final state it is not possible to reconstruct the τ flight direction and hence determine it's rest frame if both τ decays to a single charged particle but thanks to τ boost vector this feature remains in the CM frame. The cosine of the angle between the muon and the outgoing photon is shown in figure 4.1 top left. As can be clearly seen the signal is peaked in the $\cos\theta \sim 1$ direction while the background is broadly uniform in this range. A complementary quantity is the distance between the track and the neutral cluster on the inner face of the EMC in the signal hemisphere (figure 4.1 top right). We decided to include both of them in our selection criteria because while the first quantity is purely physical the second one may include also experimental effects related to cluster reconstruction in the EMC. To reject events in which the signal photon candidate originates from a π^0 decay we set an upper limit on the invariant mass of the lepton-photon pair (figure 4.1 bottom left) as well as on the maximal energy of the photon in the CM frame. The requirement on the maximal photon energy also strongly suppress $e^+e^- \to \mu^+\mu^-(\gamma)$ contributions. A lower cut on the photon energy is useful to reject events coming from machine and detector background and improve reconstruction quality (figure 4.1 bottom right).

4.2.2 Selection

As stated in the previous section in this case the following variables are used for the selection:

- $\cos\theta_{CM,min}$: the minimum angle between the signal muon and photon in the CM frame;
- $M_{\mu\gamma}$: the maximum invariant mass of the lepton photon pair;
- $E_{\gamma,CM}$: the minimum and maximum energy of the photon in the CM;
- $d_{\mu\gamma}$: the maximum and minimum distance between the muon and the neutral deposit in the EMC;

We start from a series of nominal cuts as reported in an apply 4.8 until the procedure converges.

In this case the parameters which enter our figure of merit as explained extensively in chapter 5 are given by $\alpha = 8\%$ and $\beta = 2.5\%$.

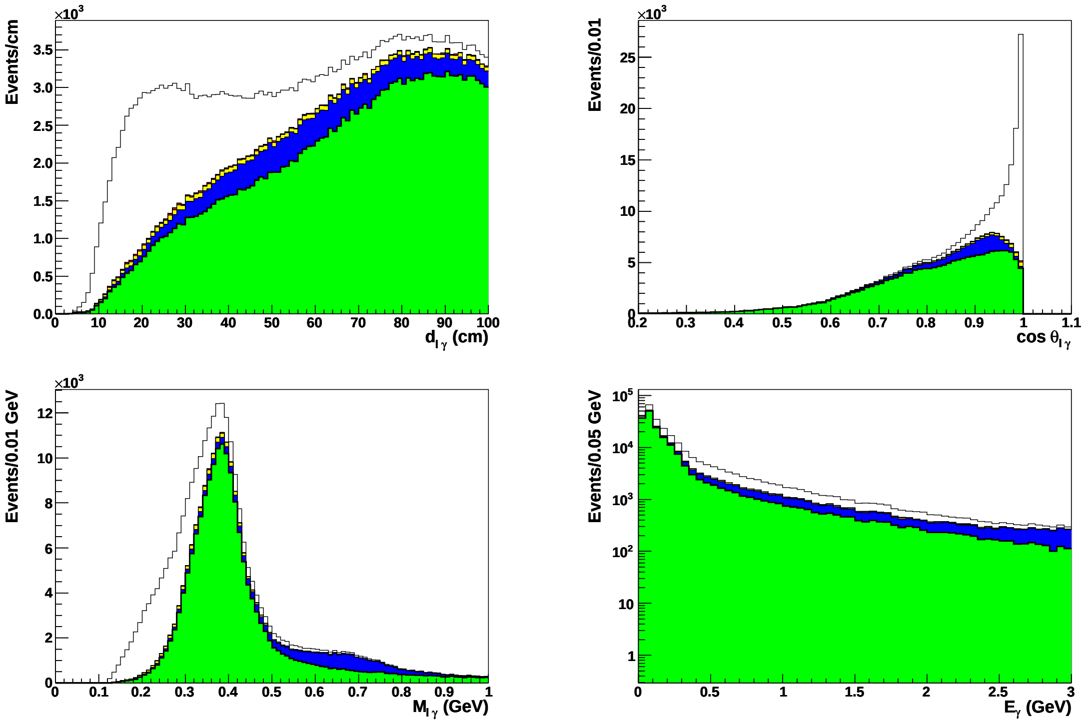

Figure 4.1: From top to bottom, left to right: distance between lepton and photon candidates on the inner EMC wall, cosine of the angle between momenta of the lepton and photon in the CM frame, invariant mass and photon candidate energy in the CM frame for radiative τ decay into a muon after applying all selection cuts of table 4.2. The green bars are $\tau \to \mu\nu\bar{\nu}$ decays, the blue bars are $\tau \to \pi\pi^0\nu$ decays, the red bars are $ee \to \mu\mu$ events, the white bars are signal $\tau \to \mu\gamma\nu\bar{\nu}$ decays while the yellow bars are other (background) τ decays.

Variable	Value
$\cos\theta_{CM,min}$	0.96
$E_{\gamma,min}$	0.05
$E_{\gamma,max}$	4.0
$d_{\mu\gamma,min}$	5
$d_{\mu\gamma,max}$	70
$M_{\mu\gamma,max}$	0.40

Table 4.1: Initial set of selection criteria for $\tau \to \mu\gamma\nu\bar{\nu}$.

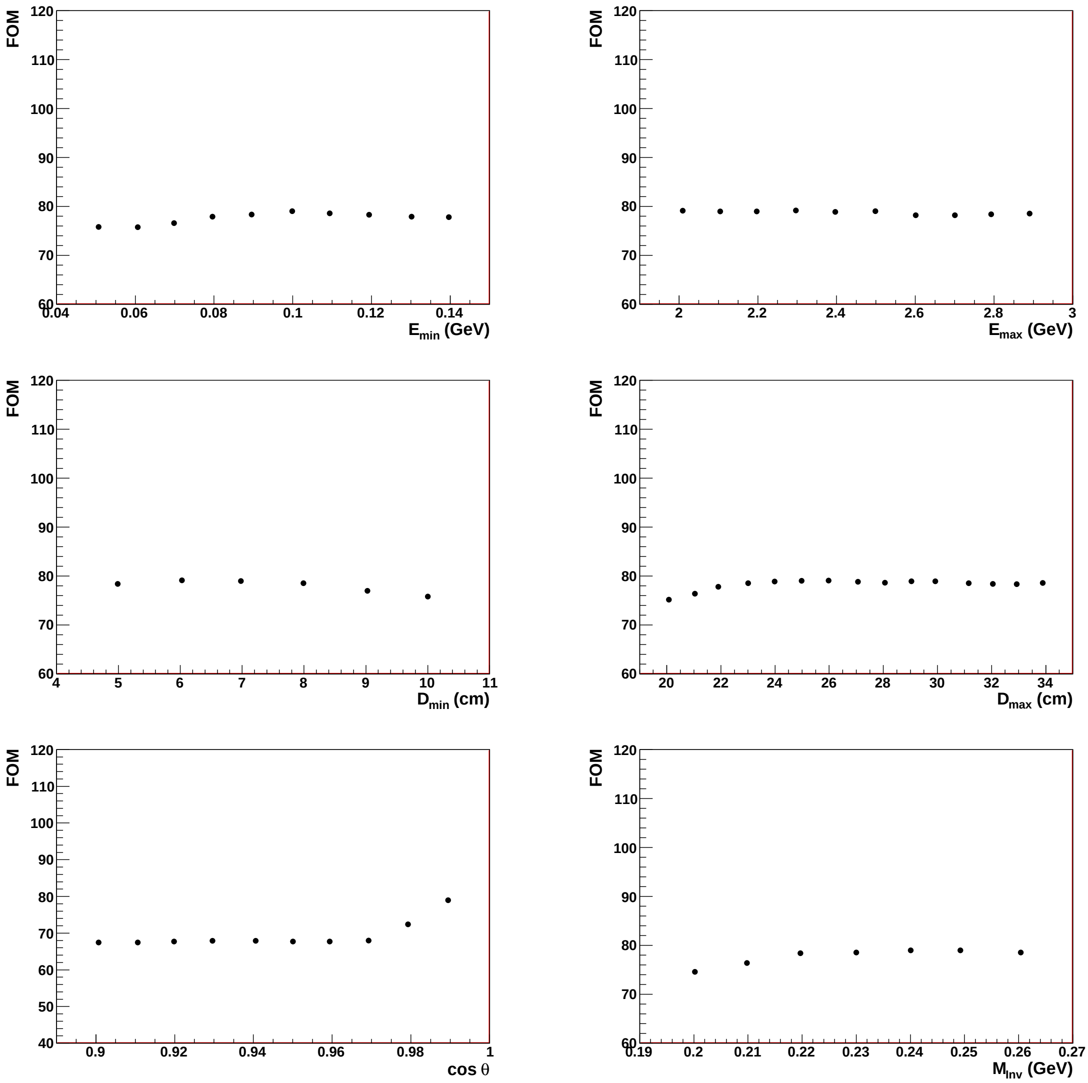

Figure 4.2: Optimization function (equation 4.7) as function of cut value for radiative τ decay into a muon for the various selection variables. From top to bottom, left to right: minimum and maximum energy in the CM frame, maximum and minimum distance between cluster and track in the EMC, the cosine of the angle between track and photon in the CM and invariant mass of the lepton-photon system. Just a small range around the optimized value is shown. All cuts except the plotted one are set to their nominal value.

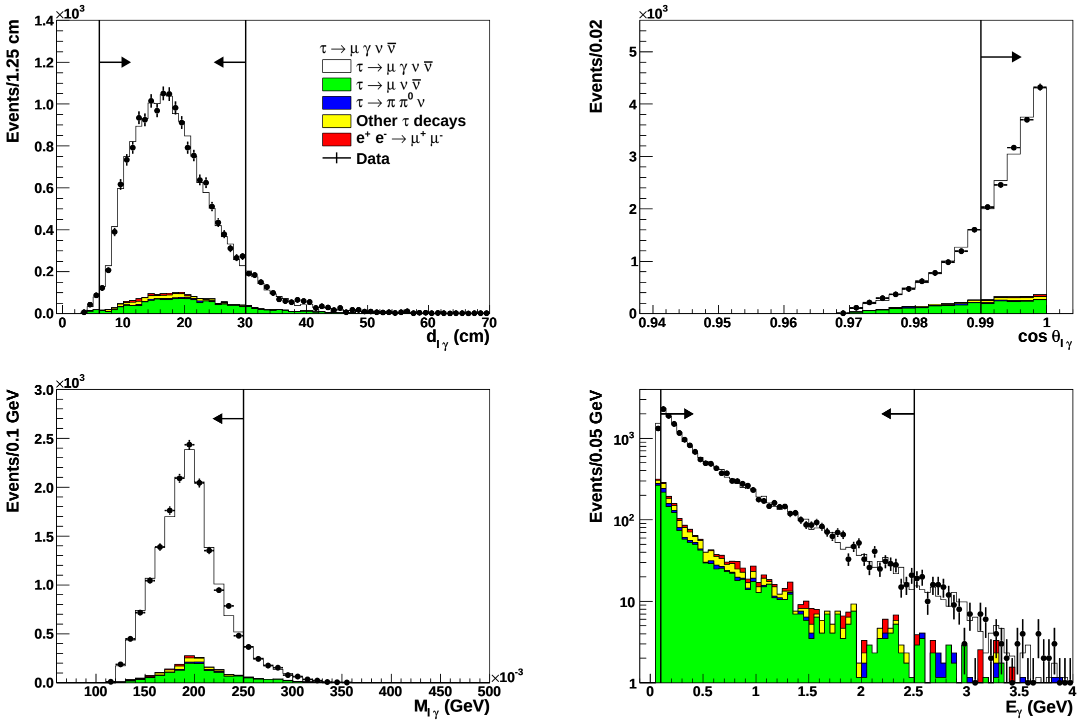

Figure 4.3: From top to bottom, left to right: distance between lepton and photon candidates on the inner EMC wall, cosine of the angle between momenta of the lepton and photon in the CM frame, invariant mass and photon candidate energy in the CM frame for radiative τ decay into a muon after applying all selection cuts of table 4.2 except the one on the plotted quantity. The green bars are $\tau \to \mu\nu\bar{\nu}$ decays, the blue bars are $\tau \to \pi\pi^0\nu$ decays, the red bars are $ee \to \mu\mu$ events, the white bars are signal $\tau \to \mu\gamma\nu\bar{\nu}$ decays while the yellow bars are other (background) τ decays and the black dots are data.

Variable	Value
$\cos\theta_{CM,min}$	0.99
$E_{\gamma,min}$	0.10
$E_{\gamma,max}$	2.5
$d_{\mu\gamma,min}$	6
$d_{\mu\gamma,max}$	30
$M_{\mu\gamma,max}$	0.25

Table 4.2: Summary of optimized selection cuts applied to $\tau \to \mu\gamma\nu\bar{\nu}$.

4.3 Selection of $\tau \to e\gamma\nu\bar{\nu}$

4.3.1 Kinematics and backgrounds

Also in this case the signal photon is emitted preferentially in the direction of th outgoing lepton, the phase space distribution of the lepton-photon pair in the CM frame is similar to the $\tau \to \mu\gamma\nu\bar{\nu}$ and the $\cos\theta$ distribution is even more strongly peaked in the forward direction, as is clearly shown in figure 4.4 top left. However the discriminating power of this variable is less powerful than in the $\tau \to \mu\gamma\nu\bar{\nu}$ decays because of the different background contribution to $\tau \to e\gamma\nu\bar{\nu}$. About two thirds of the preselected sample in this case consist of $\tau \to e\nu\bar{\nu}$ decays in which a photon is emitted by the electron drifting trough the detector. The similarity of the photon and electron energy spectra for detector and background (see figures 4.4) make it difficult to discriminate between them and different requirements on the selection criteria are necessary with respect to the previous case.

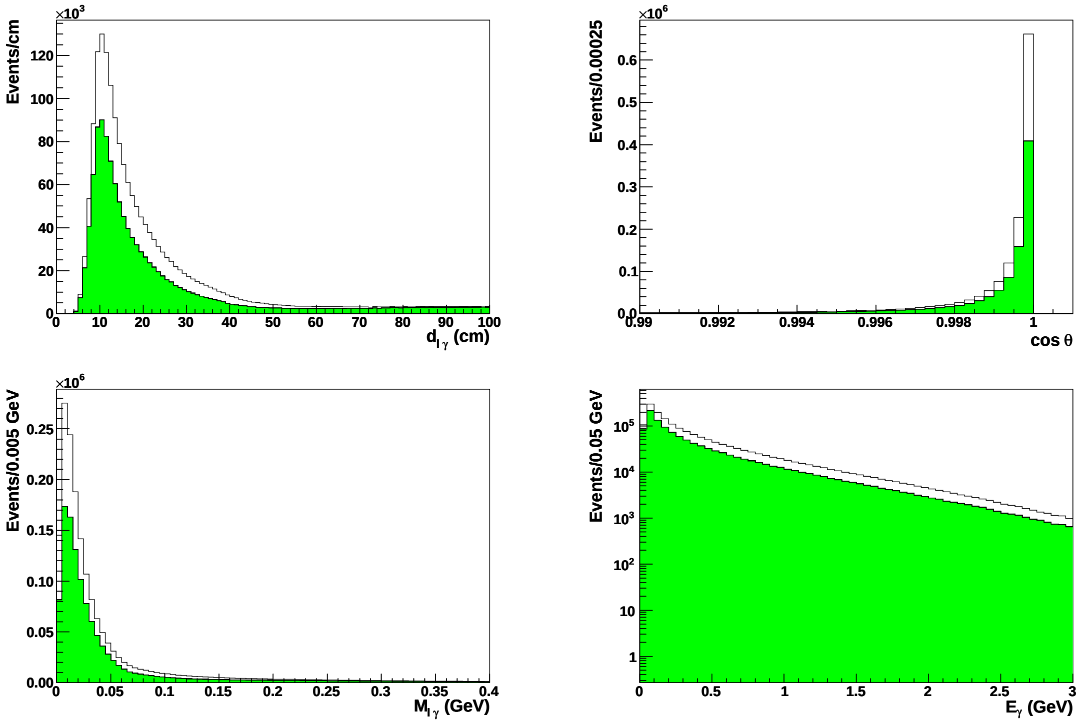

Figure 4.4: From top to bottom, left to right: distance between lepton and photon candidates on the inner EMC wall, cosine of the angle between momenta of the lepton and photon in the CM frame, invariant mass and photon candidate energy in the CM frame for radiative τ decay into an electron after preselection. The bars are $\tau \to e\nu\bar{\nu}$ decays, the white bars are signal $\tau \to e\gamma\nu\bar{\nu}$ decays while the blue bars are other (background) τ decays and the black dots are data.

For an independent proof of the type of background which is involved for $\tau \to e\gamma\nu\bar{\nu}$ decays, we have studies the distributions of the differences of the polar and azimuthal angular distributions in the CM frame. In fact because of the different curvature of negative and positive electron candidates for photons coming from bremsstrahlung we expect these distribution to be biased towards negative or positive $\Delta\phi$ values depending on charge. This effect is indeed observed on the MC (figures 4.5).

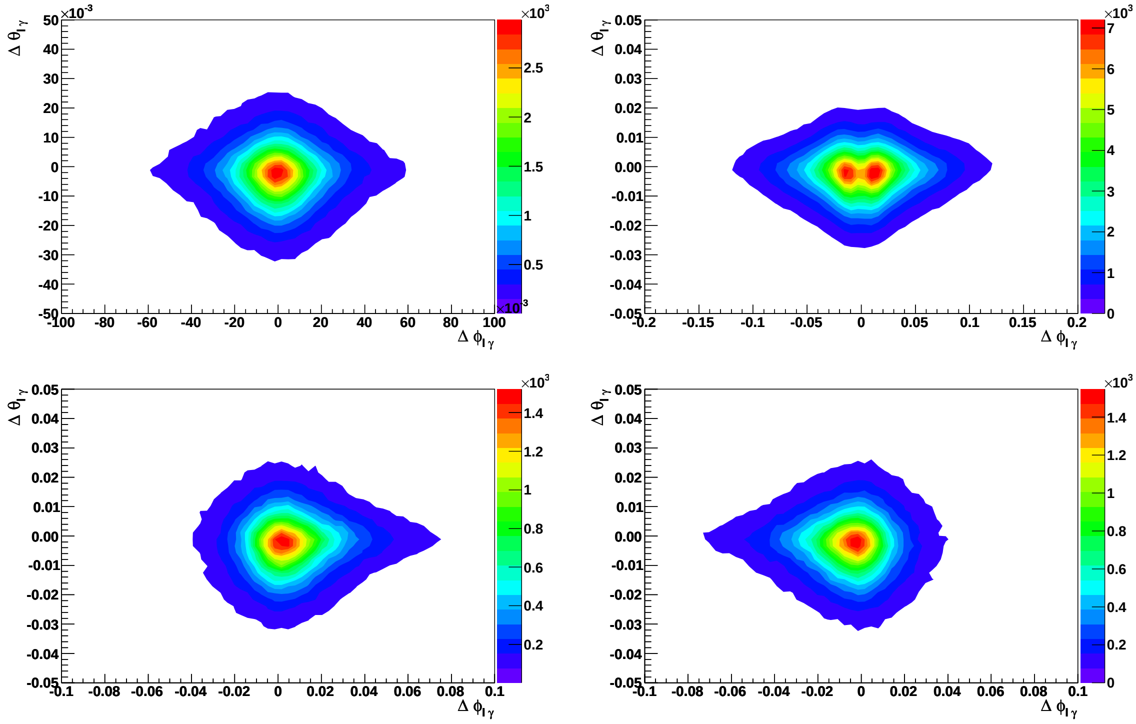

Figure 4.5: $\Delta\theta_{l\gamma}$ vs $\Delta\phi_{l\gamma}$ of the lepton photon candidates in the CM frame for radiative τ decay into an electron after preselection. Top: signal MC (left) and background MC (right). Bottom: signal MC negative electron candidates (left) and positive candidates (right).

To check that our MC correctly reproduces this effect we have compared the azimuthal distributions for positive and negative candidates as shown in figure 4.6.

To recover discriminating power we use the fact that for bremsstrahlung photons the invariant mass of the lepton photon pair $M_{l\gamma} \sim 0$ while for $\tau \to e\gamma\nu\bar{\nu}$ its value is only limited by the τ mass. Differently to what we have done for $\tau \to \mu\gamma\nu\bar{\nu}$ we hence impose, in addition to the other selection criteria, a lower value on the invariant mass of the lepton-photon pair $M_{inv,min}$. This is a strong requirement in terms of signal yield, nevertheless, as will be shown in detail in later section this allows us to achieve a much better signal to noise ration with respect to existing measurements. Figure 4.8 shows the effect of this requirement.

4.3.2 Selection

As discussed in the previous section, in this case the following variables are used for the selection:

- $\cos\theta_{CM,min}$: the angle between the signal electron and the photon in the CM frame;
- $M_{e\gamma}$: the minimum invariant mass of the lepton photon pair;

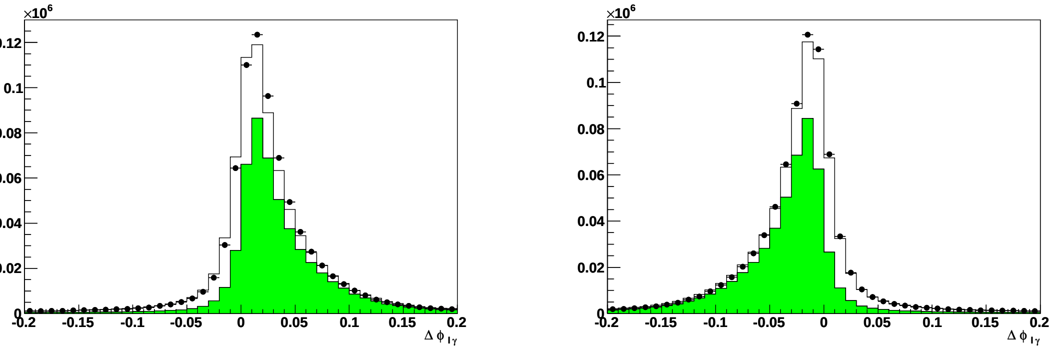

Figure 4.6: $\Delta\phi_{l\gamma}$ of the lepton photon candidates in the CM frame for radiative τ decay into an electron after preselection for signal MC negative electron candidates (left) and positive candidates (right). The green bars are $\tau \to e\nu\bar{\nu}$ events while the white bars are $\tau \to e\gamma\nu\bar{\nu}$ events.

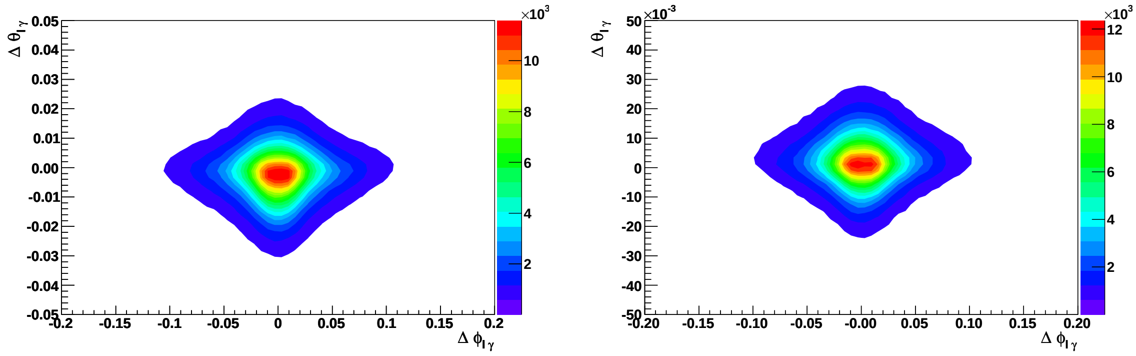

Figure 4.7: $\Delta\theta_{l\gamma}$ vs $\Delta\phi_{l\gamma}$ of the lepton photon candidates in the CM frame for radiative τ decay into an electron after preselection for (full) MC (left) and data (right).

- $E_{\gamma,CM}$: the minimum and maximum energy of the photon in the CM;
- $d_{e\gamma}$: the maximum and minimum distance between the electron and the neutral deposit in the EMC;

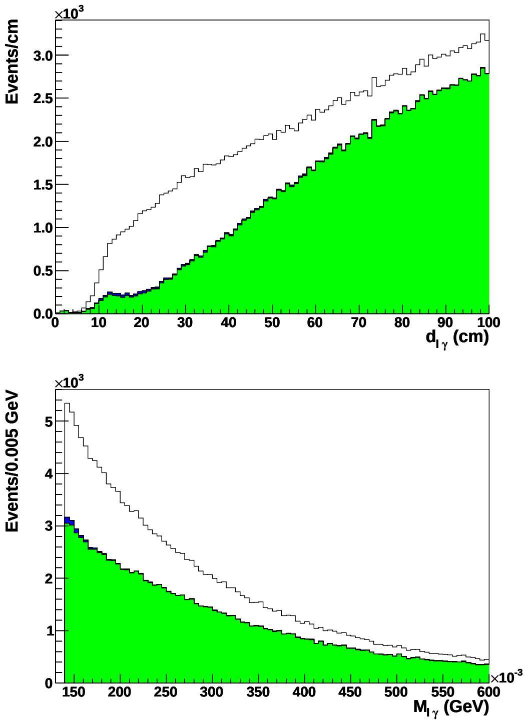

Figure 4.8: From top to bottom, left to right: distance between lepton and photon candidates on the inner EMC wall, cosine of the angle between momenta of the lepton and photon in the CM frame, invariant mass and photon candidate energy in the CM frame for radiative τ decay into an electron after preselection with the additional requirement on $M_{l\gamma,min}$. The green bars are $\tau \to e\nu\bar{\nu}$ decays, the white bars are signal $\tau \to e\gamma\nu\bar{\nu}$ decays while the blue bars are other (background) τ decays and the black dots are data.

Variable	Value
$\cos\theta_{CM,min}$	0.99
$E_{\gamma,min}$	0.05
$E_{\gamma,max}$	4.0
$d_{e\gamma,min}$	10
$d_{e\gamma,max}$	50
$M_{e\gamma,min}$	0.0

Table 4.3: Initial set of selection criteria applied for $\tau \to e\gamma\nu\bar{\nu}$.

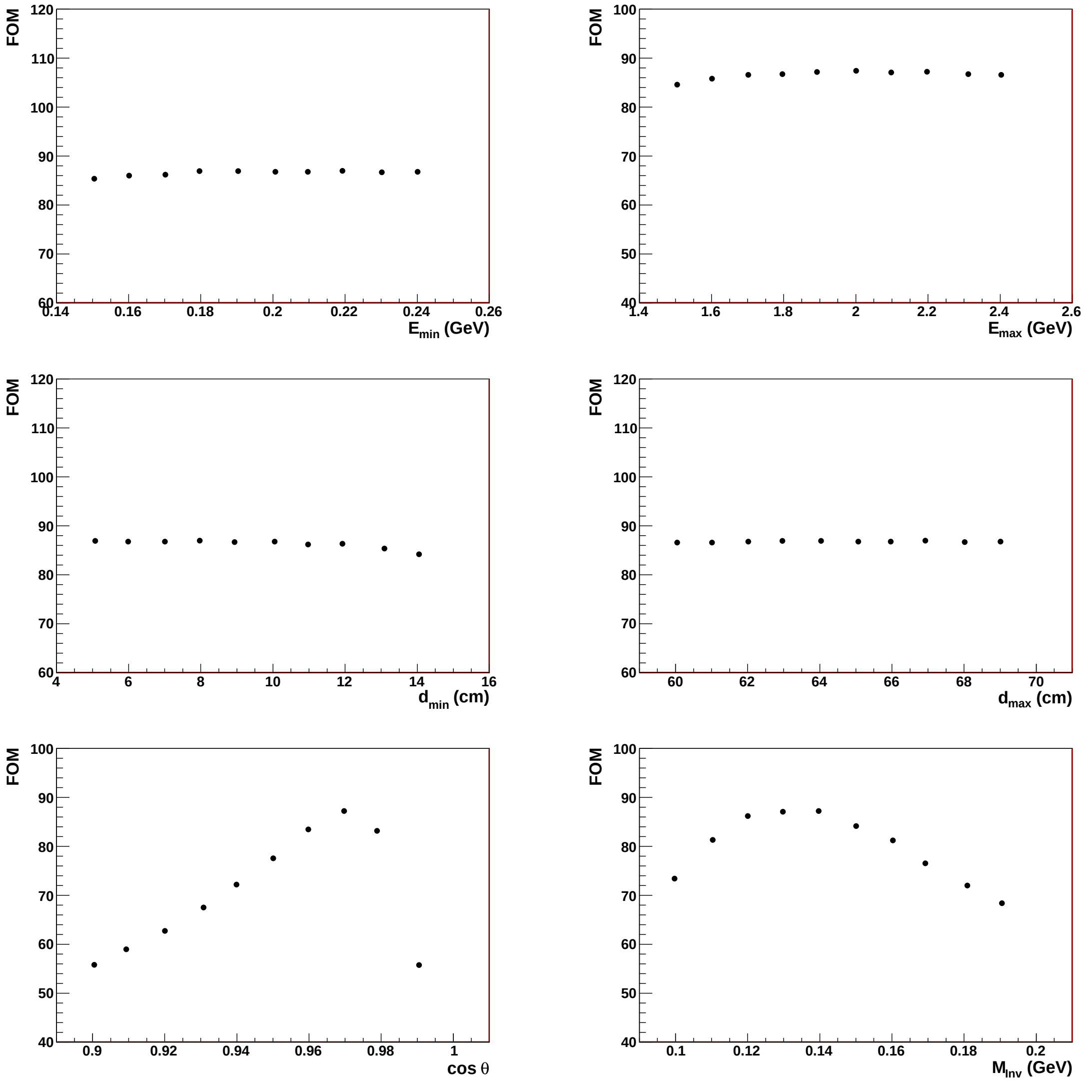

Figure 4.9: Optimization function (equation 4.7) as function of cut value for radiative τ decay into an electron for the various selection variables. From top to bottom, left to right: minimum and maximum energy in the CM frame, maximum and minimum distance between cluster and track in the EMC, the cosine of the angle between track and photon in the CM and invariant mass of the lepton-photon system. Just a small range around the optimized value is shown. All cuts except the plotted one are set to their nominal value.

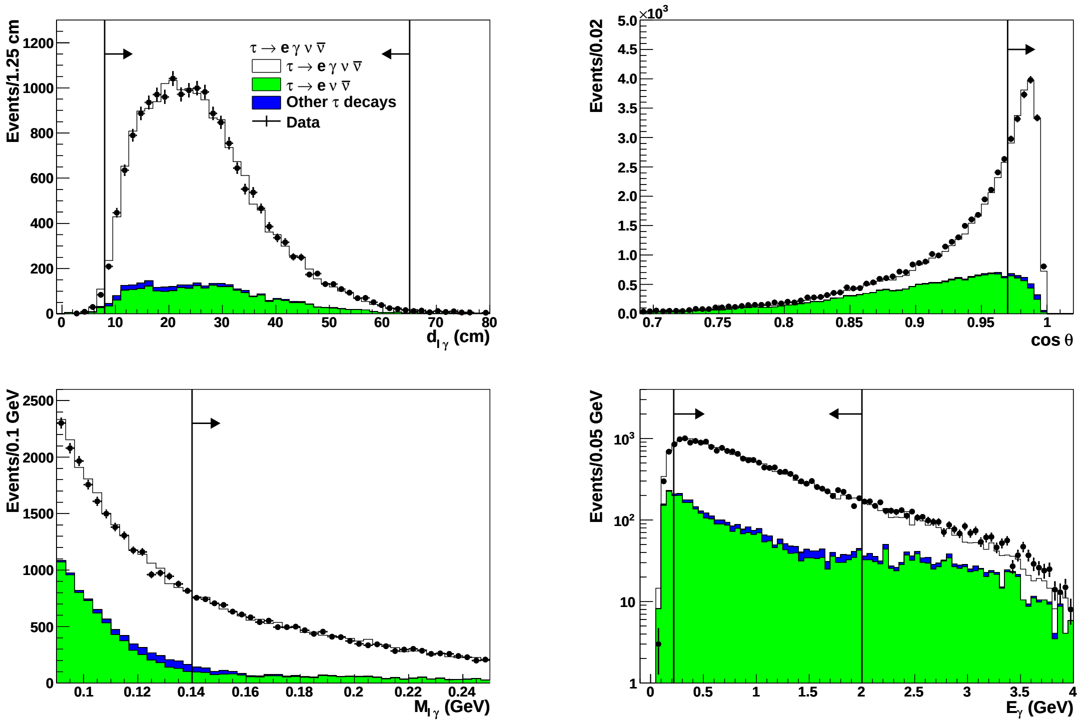

Figure 4.10: From top to bottom, left to right: distance between lepton and photon candidates on the inner EMC wall, cosine of the angle between momenta of the lepton and photon in the CM frame, invariant mass and photon candidate energy in the CM frame for radiative τ decay into an electron after applying all selection cuts of table 4.3.2 except the one on the plotted quantity. The green bars are $\tau \to e\nu\bar{\nu}$ decays, the white bars are signal $\tau \to e\gamma\nu\bar{\nu}$ decays while the blue bars are other (background) τ decays.

Variable	Value
$\cos\theta_{CM,min}$	0.97
$E_{\gamma,min}$	0.22
$E_{\gamma,max}$	2.0
$d_{e\gamma,min}$	8
$d_{e\gamma,max}$	65
$M_{e\gamma,min}$	0.14

Table 4.4: Summary of optimized selection cuts applied to $\tau \to e\gamma\nu\bar{\nu}$.

4.4 Standard Figure of Merit

For completeness we report also the results obtained using a standard figure of merit for the optimizatin, i.e.

$$FOM = \frac{N_{sig}}{\sqrt{N_{sig} + N_{bkg}}}. \tag{4.9}$$

Variable	Value
$\cos\theta_{CM,min}$	0.94
$E_{\gamma,min}$	0.05
$E_{\gamma,max}$	3.1
$d_{\mu\gamma,min}$	5
$d_{\mu\gamma,max}$	65
$M_{\mu\gamma,max}$	0.54

Table 4.5: Selection cuts for $\tau \to \mu\gamma\nu\bar{\nu}$ using 4.4.

Variable	Value
$\cos\theta_{CM,min}$	0.90
$E_{\gamma,min}$	0.05
$E_{\gamma,max}$	4.7
$d_{e\gamma,min}$	6
$d_{e\gamma,max}$	100
$M_{e\gamma,min}$	0.0

Table 4.6: Selection cuts for $\tau \to e\gamma\nu\bar{\nu}$ using 4.4.

As can be clearly seen from table 4.4 for both channels the event yield is much higher, but background rates are even higher than signal.

	Efficiency	Exp. Signal	Exp. Background	$(N_{sig}/(N_{sig} + N_{bkg}))$
$\tau \to \mu\gamma\nu\bar{\nu}$	1.112 ± 0.005 %	50517.3	25263.9	0.66
$\tau \to e\gamma\nu\bar{\nu}$	2.23 ± 0.02 %	531765	993417	0.35

Table 4.7: Summary of corrected selection efficiency and background contamination after standard optimization.

4.5 Energy cut-off and efficiency correction

Until now we did not apply any cut on the MC photon energy, i.e. we used the the MC signal sample corresponding to the whole photon energy spectrum, this was done in order to find out which is the minimum photon energy on τ rest frame to which we are sensitive. Now we want to check this point and to compute the corrected efficiency for $E^*_\gamma > 10$ MeV in order to compare our results with the measurements that have been performed by CLEO.

For $\tau \to \mu\gamma\nu\bar{\nu}$ the contamination of events with less than 10 MeV in the τ rest frame is 0.13%, while in the electron case it is negligible for $\tau \to e\gamma\nu\bar{\nu}$.

The corrected efficiency is given by

$$\epsilon^* = \frac{(N_{sig,sel}(E^* > 10MeV) - N_{sig,sel})}{N_{sig}(E^* > 10MeV)} \tag{4.10}$$

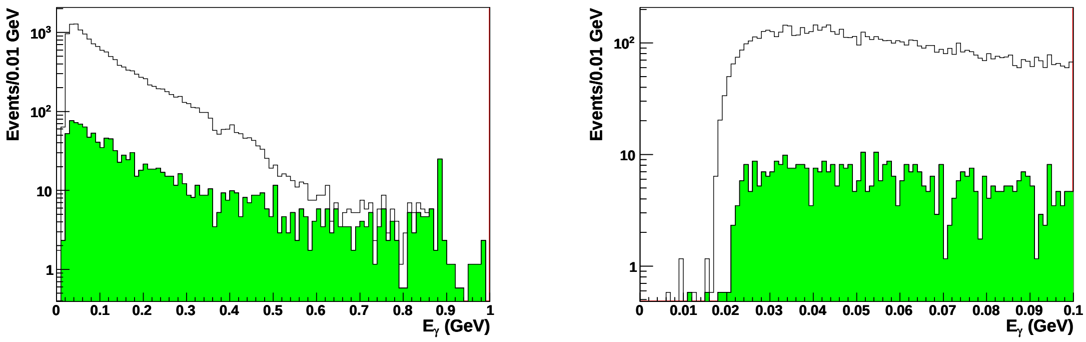

Figure 4.11: Candidate photon energy distribution for $\tau \to \mu\gamma\nu\bar{\nu}$ in the tau rest frame after selection (left) and closeup at low energy (right). The green bars are $\tau \to \nu\bar{\nu}$ events while the white bars are $\tau \to \mu\gamma\nu\bar{\nu}$ events.

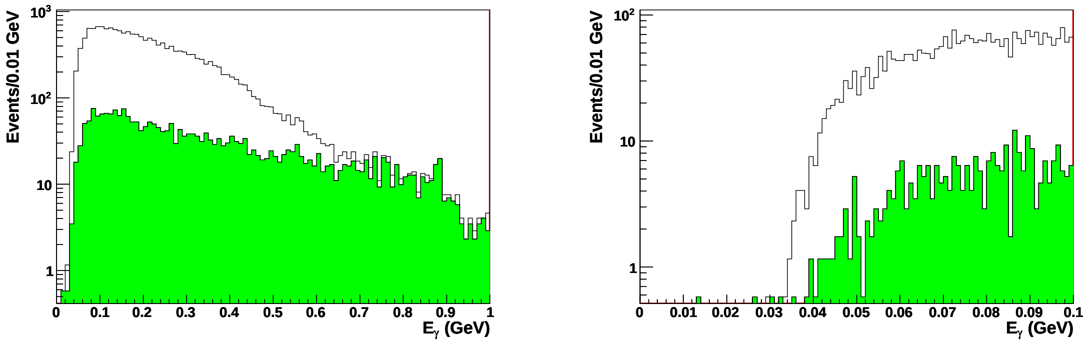

Figure 4.12: True candidate photon energy distribution for $\tau \to e\gamma\nu\bar{\nu}$ in the tau rest frame after selection (left) and closeup at low energy (right). The green bars are $\tau \to e\nu\bar{\nu}$ events while the white bars are $\tau \to e\gamma\nu\bar{\nu}$ events.

	Efficiency	Exp. Signal	Exp. Background	$N_{bkg}/(N_{sig}+N_{bkg})$
$\tau \to \mu\gamma\nu\bar{\nu}$	$(0.480 \pm 0.010)\%$	14053 ± 118	1596 ± 40	0.102 ± 0.02
$\tau \to e\gamma\nu\bar{\nu}$	$(0.105 \pm 0.003)\%$	16316 ± 124	2823 ± 53	0.156 ± 0.003

Table 4.8: Summary of corrected signal selection efficiency and background contamination after all selection cuts are applied.

Chapter 5

Systematic Errors and Cross Checks

Given the formula for the branching faction given in 4.1, i.e.

$$BR_{\tau\to X\gamma\nu\bar{\nu},X=e,\mu} = \frac{N_{obs} - N_{bkg}}{2\epsilon_X \sigma_{\tau\tau} \mathcal{L}} \tag{5.1}$$

we can group the systematic contributions to the total error in three classes:

- Signal efficiency
- Background evaluation
- Luminosity and cross-section

This contributions will be examined in the following sections in detail.

5.1 Signal efficiency

- Limited MC statistics:
  Due to limited number of events used for efficiency calculation we have to account for the fluctuation on the number of selected and produced events; this contribution can be written as

  $$\sigma_{MC} = \sqrt{\frac{\epsilon(1-\epsilon)}{N_{MC}}}. \tag{5.2}$$

  This contribution varies from 0.5% (relative percent) for $\tau \to \mu\gamma\nu\bar{\nu}$ to 0.6% for $\tau \to e\gamma\nu\bar{\nu}$.

- Trigger and background filters (TauBGF):
  To evaluate the effect of trigger and background filters we look at the change in signal efficiency due to this requirements; for what concerns the trigger one sees that the signal efficiency is unchanged within 0.01% for both channels, hence the uncertainty on this component can be neglected. For what concerns the background filters, there is an efficiency drop of 4.9% for $\tau \to \mu\gamma\nu\bar{\nu}$ and of 6.4% for $\tau \to e\gamma\nu\bar{\nu}$. As most of the inefficiency is associated with the geometrical acceptance, we conservatively assume the MC correctly describes the data up to a relative factor 10% due to the inefficiency from these sources.This leads to a systematic error estimate of 0.6% (0.5%) for $\tau \to e\gamma\nu\bar{\nu}$ and $\tau \to \mu\gamma\nu\bar{\nu}$ respectively.

- Tracking and resolution:
  Differences between data and MC tracking efficiency will lead to a systematic contribution; for $p_T > 180$ MeV single track modeling is good up to 0.14%, hence we assign safely a 0.28% total uncertainty on efficiency both for $\tau \to \mu\gamma\nu\bar{\nu}$ and $\tau \to e\gamma\nu\bar{\nu}$.

- PID:
  Possible discrepancies between data and MC resolution may introduce a systematic contribution on signal efficiency; discrepancies between data and MC PID efficiencies have been accounted for using the weights from the PID tables with the tweaking technique: first, the selection procedure as defined by the selector is run then, with the help of PID-efficiency tables derived from data and MC (where MC has been treated in the same way as data), the second step is either rejecting an accepted track with probability

$$\epsilon_{data}/\epsilon_{MC} \text{ if } \epsilon_{data} < \epsilon_{MC} \tag{5.3}$$

  or accepting a rejected track with probability

$$(\epsilon_{data} - \epsilon_{MC})/(1 - \epsilon_{MC}) \text{ if } \epsilon_{data} > \epsilon_{MC}. \tag{5.4}$$

  We introduce for each charged track an error which corresponds to the error on the ratio $\epsilon_{data}/\epsilon_{MC}$ in the given momentum range. The total error per event is taken as the sum in quadrature of the errors o the two tracks. As can be seen in 5.1 and 5.2 in the considered momentum range those errors are around 1% for all selectors which means that we can reasonably assign a 1.5% uncertainty due to PID.

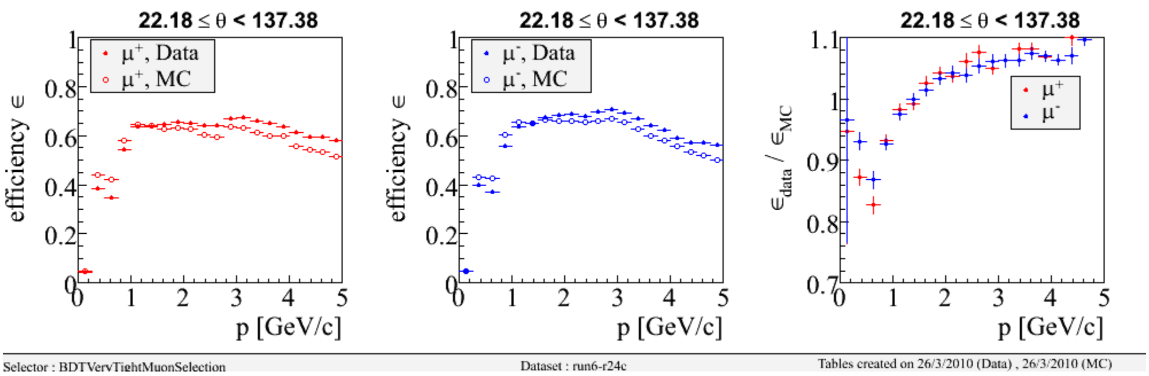

Figure 5.1: MC and data efficiency comparison for the BDTVeryTight muon selector as function of momentum.

- Photon efficiency:
  Various studies have been performed in *BABAR* to study efficiency corrections between data and MC both for photon efficiency using $e^+e^- \to \mu^+\mu^-\gamma$ events [26] (and references therein) in which the photon kinematics can be fully reconstructed using the muon pair. This process is sensitive to photons with a minimum energy of 1 GeV and data and MC have seen to compatible within 1% [26]. For low energy photons efficiency is extracted from π^0 reconstruction efficiency measuring the

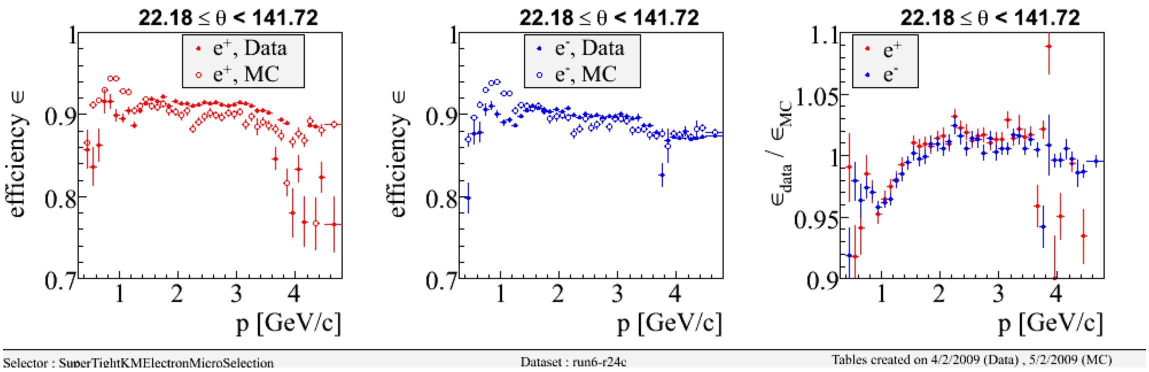

Figure 5.2: MC and data efficiency comparison for the SuperTightKM electron selector as function of momentum.

branching fraction ratio for $\tau \to \pi\nu$ and $\tau \to \rho\nu$ decays [27]. The resulting π^0 efficiency is 3% and including a 1.1% uncertainty on the branching fraction the resulting single photon efficiency is taken to be 1.8%. Although the processes we are looking for involve photons whose spectrum is peaked at zero the maximum discrepancy between data and MC in our spectra is seen at high energy; as consequence we can safely set the systematic contribution to efficiency to 1.8%.

- Dependence on selection criteria:
  Another possible source of systematic uncertainty may come from the dependence of the result from the selection criteria; in particular a non-negligible variation of the value of the BF has been observed varying the minimum value of $\cos\theta_{l\gamma}$ (cfr. fig. 6.8). To evaluate this contribution we have studied calculated the resolution on $\cos\theta_{l\gamma}$ for the two signal modes by taking the difference between the reconstructed value of the momenta and the MC truth value. The distributions obtained for the 2 modes are shown in figure 5.3.

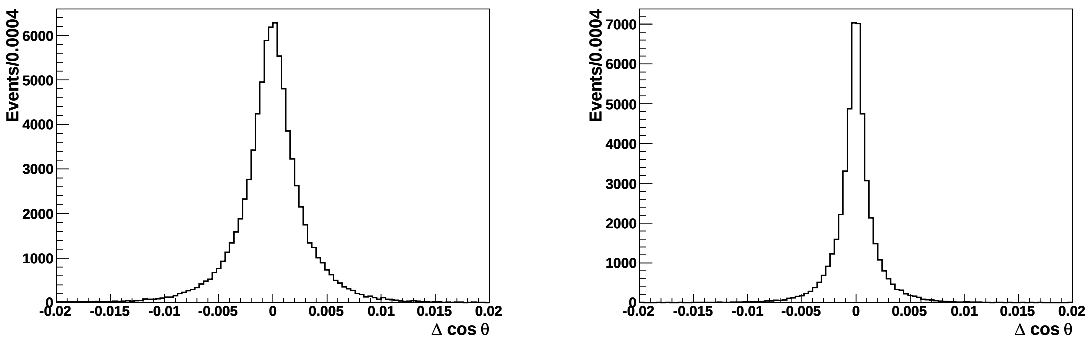

Figure 5.3: Resolution on the angle between lepton and photon for $\tau \to e\gamma\nu\bar{\nu}$ (left) and $\tau \to \mu\gamma\nu\bar{\nu}$ (right) in the CM frame.

From the distributions shown in 5.3 we extract the RMS of the distributions for the two signal modes and we perform a scan on $\cos\theta_{l\gamma,min}$ (fig. 5.4). The maximum variation on the value of the BF in a $\pm\sigma$ interval around the optimized value of $\cos\theta_{l\gamma,min}$ is taken as uncertainty due to the choice of selection criteria. For both channels this value is found to be $< 0.5\%$, and hence we take this value as estimate of the uncertainty due to the choice of selection criteria.

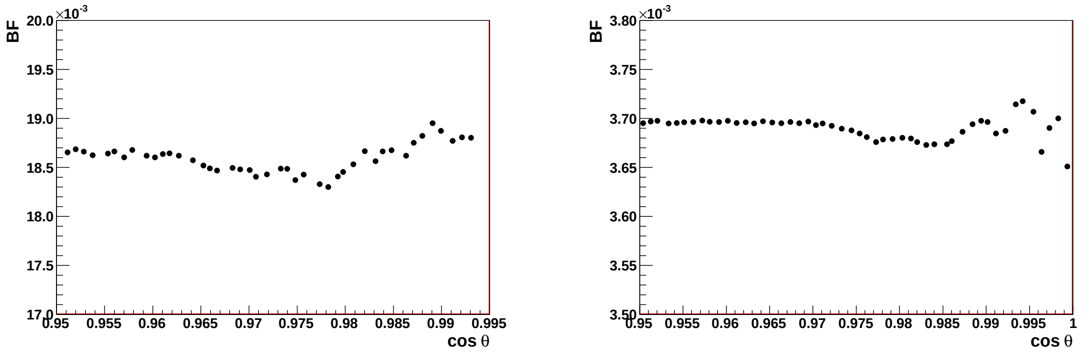

Figure 5.4: Branching fraction as function of the minimum value of the cosine of the angle between track and photon in the CM for $\tau \to e\gamma\nu\bar{\nu}$ (left) and $\tau \to \mu\gamma\nu\bar{\nu}$ (right). All selection criteria except the plotted one are set to their nominal value.

It is worth to note that even if the $\tau \to \mu\gamma\nu\bar{\nu}$ distribution has a notable better resolution on $\cos\theta_{l\gamma}$ the corresponding uncertainty is of the same size as that for $\tau \to e\gamma\nu\bar{\nu}$ because of the lower statistic and bigger fluctuation on N_{sig} when varying selection criteria.

- PDG branching fractions:
  Tau decays in the tag-side for signal MC sample are simulated by Tauola according to PDG branching fractions with an additional unitary constrain imposed. The related systematic error is evaluated as a quadrature sum of the individual branching fraction uncertainties weighted by the relative fraction of selected events in a given channel. The relative systematic uncertainty is estimated to be 0.7%.

- E_{min} cut-off and efficiency correction:
  we consider the fluctuation on the number of photons with $E^* < 10$ MeV which was subtracted to the selected samples in the previous section; for $\tau \to \mu\gamma\nu\bar{\nu}$ we observe a 0.13% contamination from $E^* < 10$ MeV photons and the corresponding uncertainty on the BF is 0.03%, while for $\tau \to e\gamma\nu\bar{\nu}$, due to the higher cut on the minimum photon energy in the CM frame, we do not observe any photon with $E^* < 10$ MeV in the final sample and hence the corresponding uncertainty is negligible.

5.2 Background estimation

For background estimation we want to rely as little as possible on MC simulation, in this way we can account for background modes not included in simulation or to unknown background modes as well as for MC/data discrepancies. For this reason we define suitable control regions to evaluate background rates as explained in the following.

- $\tau \to \mu\nu\bar{\nu}$:
  in this case the major background contribution comes from generic τ decays is

not peaking in $\cos\theta_{l\gamma}$ and to evaluate possible discrepancy between data and MC we define a sideband region where the expected signal yield is low; this region is defined by $\cos\theta_{\mu\gamma} < 0.8$. In this region the expected signal is 3% of the whole MC sample. The discrepancy between the MC prediction and the number of observed events is 8%, with an excess of MC events. We take this discrepancy as error on the background MC accuracy.

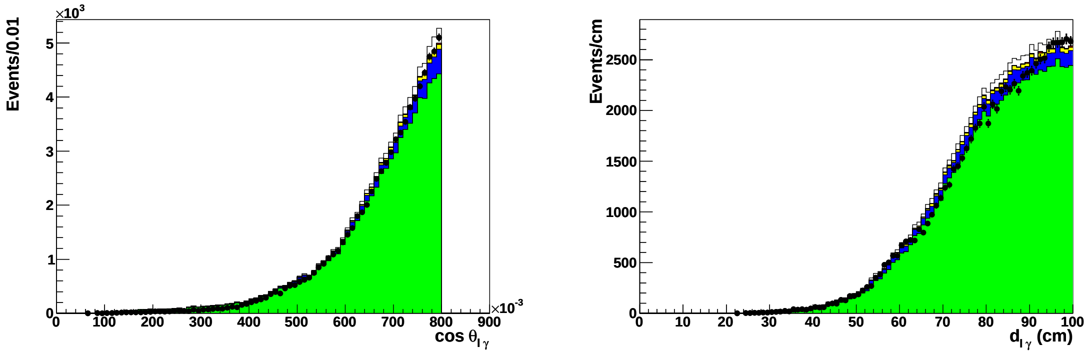

Figure 5.5: Angle (left) and distance in the EMC (right) between lepton and photon τ decay into a muon in the control region. The black dots are data, the green bars are generic (non signal) τ MC decays while the white bars are $\tau \to \mu\gamma\nu\bar{\nu}$ decays.

- $\tau \to e\nu\bar{\nu}$:
  in this case the major background component is from external-bremsstrahlung and has the same distribution as signal in all variables used for selection; to apply the same strategy as before first we cut on the invariant mass of the photon-lepton pair $M_{e\gamma} < 0.14$ and then consider the distribution of $\cos\theta_{e\gamma}$ for $\cos\theta_{e\gamma} < 0.95$

  In this region the expected signal is 10% of the whole MC sample. The discrepancy between the MC prediction and the number of observed events is 4%, with an excess of data events. We take this discrepancy as error on the background MC accuracy.

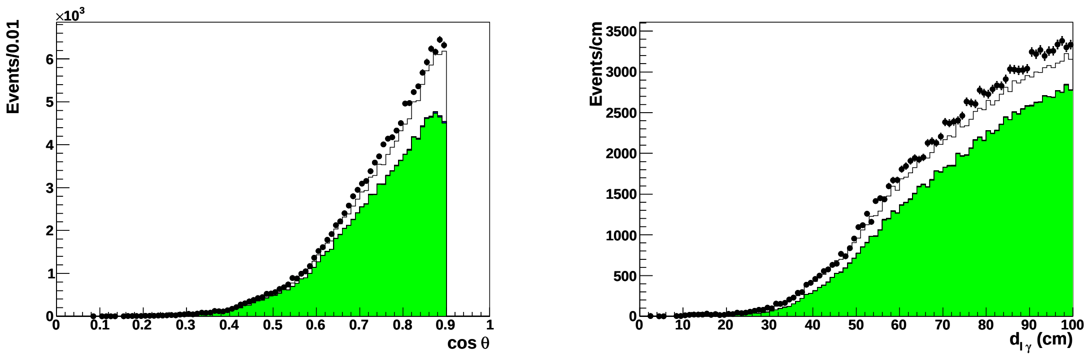

Figure 5.6: Angle (left) and distance in the EMC (right) between lepton and photon τ decay into an electron in the control region. The black dots are data, the green bars are generic (non signal) τ MC decays while the white bars are $\tau \to e\gamma\nu\bar{\nu}$ decays.

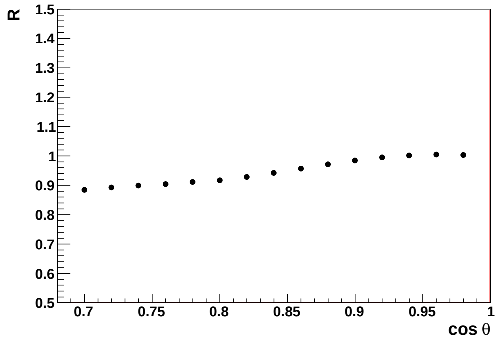

Figure 5.7: Data/MC ratio as function of cut value on $\cos\theta_{l\gamma}$ for radiative τ decay into a muon. All preselection criteria are applied but no selection criteria except the plotted one.

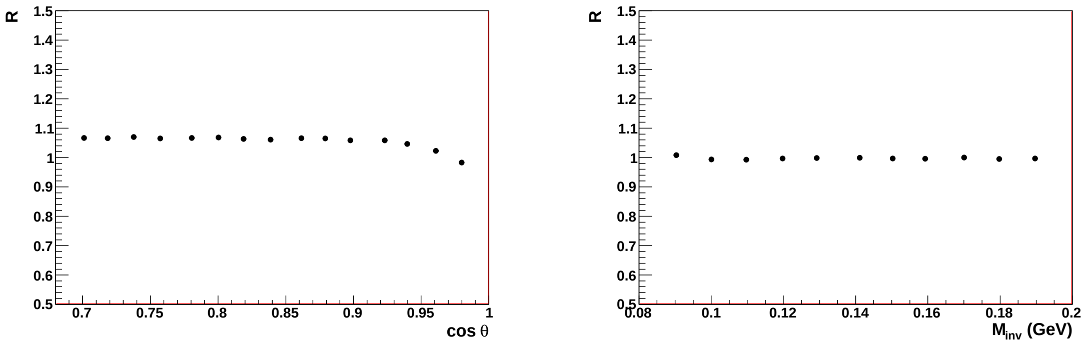

Figure 5.8: Data/MC ratio as function of cut value on $\cos\theta_{l\gamma}$ (left) and invariant mass of the lepton-photon system for radiative τ decay into an electron. All preselection criteria are applied but no selection criteria except the plotted one.

5.3 Luminosity and cross section

- Luminosity:
  The total luminosity recorded by *BABAR* at the $\Upsilon(4S)$ has been recently measured in a separate analysis with 0.5% precision using muon pairs [28].

- $\tau^+\tau^-$ production cross-section:
  The cross section τ pair production is taken from [19]. The average for *BABAR* running conditions is give by $\sigma_{\tau\tau} = 0.919 \pm 0.003$ nb.

The combined contribution of cross-section and luminosity errors gives a total 0.6% uncertainty to the number of produced tau pairs.

5.4 Summary

The systematic error on the branching fraction is obtained from

$$\mathcal{B} = \frac{N_{sig} - N_{bkg}}{2\epsilon_{\tau\to l\gamma\nu\bar{\nu}}\sigma_{e^+e^-\to\tau^+\tau^-}\mathcal{L}} \tag{5.5}$$

assuming $\mathcal{B} = f(x, y, z)$ with $x = N_{bkg}$, $y = \epsilon_{\tau\to l\gamma\nu\bar{\nu}}$, $z = \sigma_{e^+e^-\to\tau^+\tau^-}\mathcal{L}$) and using the usual formula

$$\Delta\mathcal{B} = \sqrt{\sum_i (\frac{\partial\mathcal{B}}{\partial x_i}\Delta x_i)^2}. \tag{5.6}$$

The various systematic components on efficiency are assumed to be independent and summed together in quadrature. The total statistical error on $\mathcal{B}$ is calculated taking the poissonian fluctuation on the number of observed events, i.e. $\sqrt{N_{sig}}$.

Table 5.4 summarizes the different systematic contributions to the total error in relative percent on the three discussed contributions.

	$\tau \to \mu\gamma\nu\bar{\nu}$	$\tau \to e\gamma\nu\bar{\nu}$
Photon efficiency	1.8	1.8
Particle ID	1.5	1.5
MC Statistics	0.5	0.6
Background Evaluation	0.9	0.7
PDG BF	0.7	0.7
Luminosity and Cross Section	0.6	0.6
Trigger & BGF	0.5	0.6
Selection criteria	0.5	0.5
Track reconstruction	0.3	0.3
E_{min}	0.03	–

Table 5.1: Summary of systematic contributions to the BF (in relative percent) for the two signal channels.

Chapter 6

Results

6.1 The branching fractions for $\tau \to l\gamma\nu\bar{\nu}$

After final selection we count the number of events reported in table 6.1. The observed number of events is compatible with expected yield assuming the branching fractions given by the `Tauola` libraries.

	Expected Signal	Expected Background	Expected Total	Observed
$\tau \to \mu\gamma\nu\bar{\nu}$	14053	1594	15647	15688
$\tau \to e\gamma\nu\bar{\nu}$	15289	2823	18115	18149

Table 6.1: Observed and expected number of events for signal and background the two signal channels.

The relative contributions for the different backgrounds considered in the analysis is shown in table 6.1.

	Generic $\tau^+\tau^-$	$\mu^+\mu^-$	uds	$c\bar{c}$	$b\bar{b}$	Bhabha
$\tau \to \mu\gamma\nu\bar{\nu}$	1494	100	–	–	–	–
$\tau \to e\gamma\nu\bar{\nu}$	2892	2	2	1	1	–

Table 6.2: Expected number of background events in the final sample for the two signal channels for the various MC modes.

A breakdown for the two charge states is shown in table 6.1 and 6.1 for $\tau \to \mu\gamma\nu\bar{\nu}$ and $\tau \to e\gamma\nu\bar{\nu}$ respectively.

Applying

$$BR_{\tau \to X\gamma\nu\bar{\nu}, X=e,\mu} = \frac{N_{obs} - N_{bkg}}{2\epsilon_X \sigma_{\tau\tau} \mathcal{L}} \tag{6.1}$$

already given in chapter 5, from the observed number of events we calculate the following values for the branching fractions of the two decays:

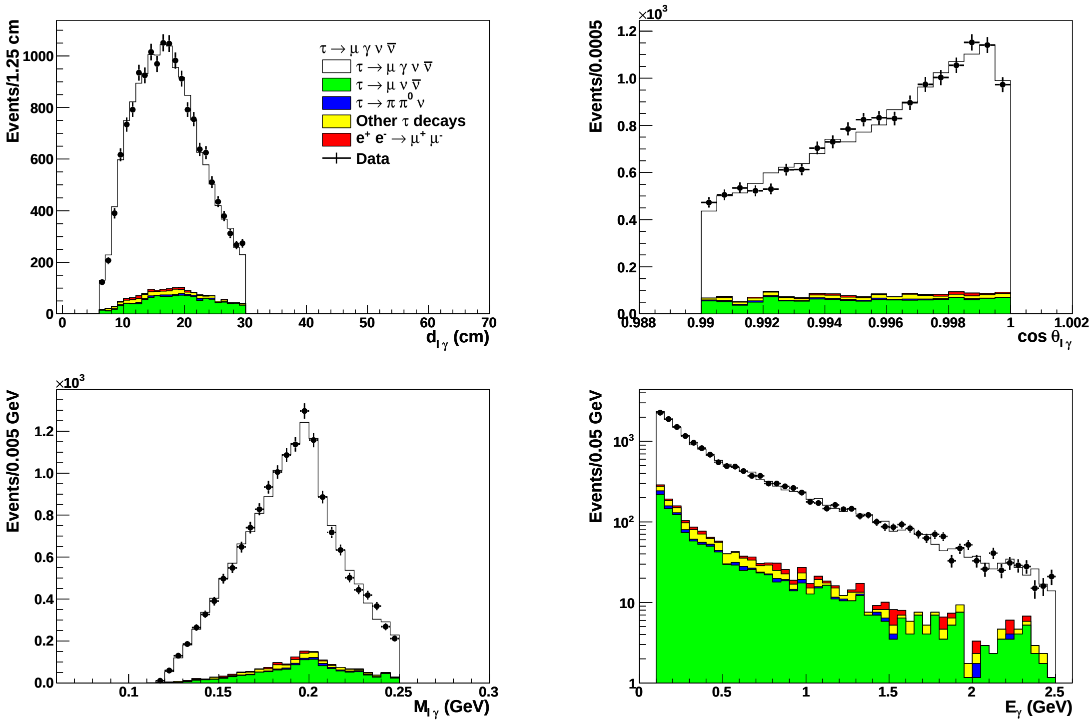

Figure 6.1: From top to bottom, left to right: distance between lepton and photon candidates on the inner EMC wall, cosine of the angle between momenta of the lepton and photon in the CM frame, invariant mass and photon candidate energy in the CM frame for radiative τ decay into a muon after applying all selection criteria of table 4.2. The green bars are $\tau \to \mu\nu\bar{\nu}$ decays, the blue bars are $\tau \to \pi\pi^0\nu$ decays, the red bars are $ee \to \mu\mu$ events, the white bars are signal $\tau \to \mu\gamma\nu\bar{\nu}$ decays while the yellow bars are other (background) τ decays and the black dots are data.

	Observed	Expected Signal	Expected Background	Expected Total
$\tau^- \to \mu^-\gamma\nu\bar{\nu}$	7859	7126	773	7899
$\tau^+ \to \mu^+\gamma\nu\bar{\nu}$	7829	6926	820	7746

Table 6.3: Observed and expected number of events for signal and background for ($\tau \to \mu\gamma\nu\bar{\nu}$) in the two charged modes.

	Observed	Expected Signal	Expected Background	Expected Total
$\tau^- \to e^-\gamma\nu\bar{\nu}$	8916	7648	1365	8959
$\tau^+ \to e^+\gamma\nu\bar{\nu}$	9233	7638	1463	9156

Table 6.4: Observed and expected number of events for signal and background for ($\tau \to e\gamma\nu\bar{\nu}$) in the two charged modes.

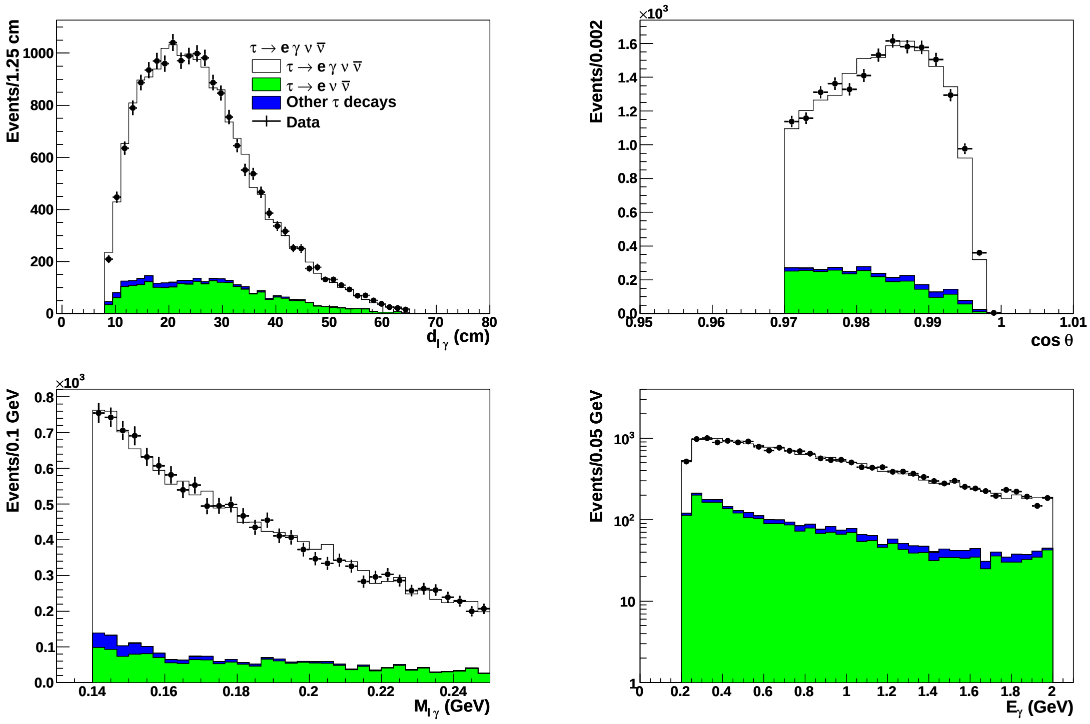

Figure 6.2: From top to bottom, left to right: distance between lepton and photon candidates on the inner EMC wall, cosine of the angle between momenta of the lepton and photon in the CM frame, invariant mass and photon candidate energy in the CM frame for radiative τ decay into an electron after applying all selection criteria of table 4.3.2. The green bars are $\tau \to e\nu\bar{\nu}$ decays, the white bars are signal $\tau \to e\gamma\nu\bar{\nu}$ decays while the blue bars are other (background) τ decays and the black dots are data.

$$BF(\tau \to \mu\gamma\nu\bar{\nu})(E^*_\gamma > 10\text{MeV}) = 0.369 \pm 0.003(\text{stat}) \pm 0.011(\text{syst})\% \tag{6.2}$$

$$BF(\tau \to e\gamma\nu\bar{\nu})(E^*_\gamma > 10\text{MeV}) = 1.847 \pm 0.015(\text{stat}) \pm 0.053(\text{syst})\%. \tag{6.3}$$

These results represent a substantial improvement with respect to existing measurements both for the statistical and the systematic error. The results are in agreement with the SM values at tree level, $\mathcal{B}(\tau \to \mu\gamma\nu\bar{\nu}) = 3.67 \times 10^{-3}$ and $\mathcal{B}(\tau \to e\gamma\nu\bar{\nu}) = 1.84 \times 10^{-2}$, as calculated in [6] including W-boson correction, as well as with measurements and, in particular, with the measurement reported by CLEO [1].

There seems to be, however, a discrepancy between the measurement and the theoretical prediction including higher order QED radiative corrections.

6.2 Cross Checks

To check for the stability of our results we performed a scan varying the selection criteria around the optimized value. The results of this scan are shown in figures 6.3 and 6.8 for $\tau \to \mu\gamma\nu\bar{\nu}$ and $\tau \to e\gamma\nu\bar{\nu}$ respectively.

6.2.1 $\tau \to \mu\gamma\nu\bar{\nu}$

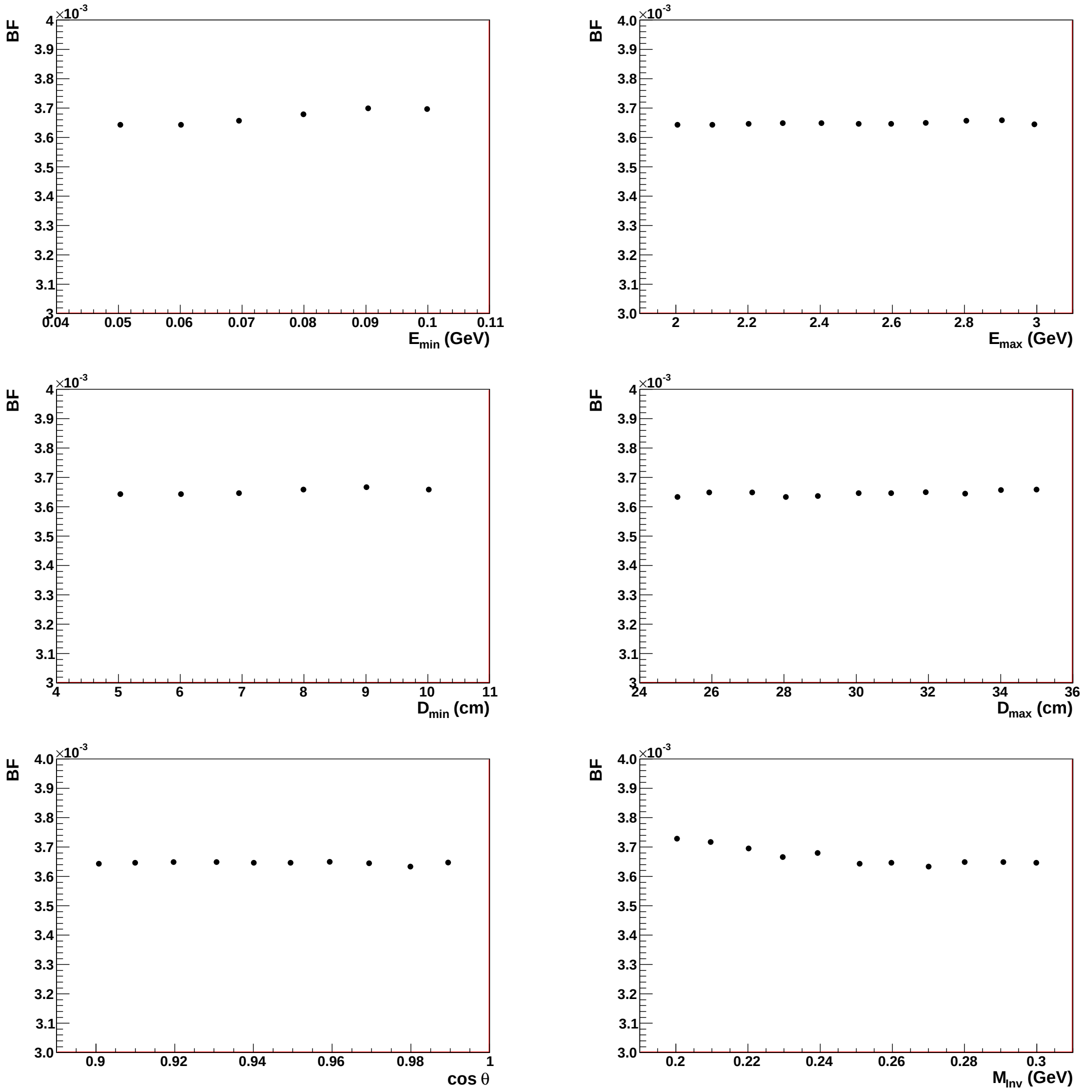

Figure 6.3: Branching fraction as function of selection criteria for radiative τ decay into a muon. From top to bottom: for the minimum (left) and maximum (right) energy of the photon in the CM frame, for the minimum (left) and maximum (right) distance between the neutral cluster and the track on the inner EMC wall and for the cosine of the angle between track and photon (left) in the CM and invariant mass (right) of the lepton-photon system. All selection criteria except the plotted one are set to their nominal value.

To check for bias in the distribution of MC/data we performed a Kolmogorov-Smirnov test on the residuals for all variables used in selection; The corresponding probability of the KS test is given in the caption of figures 6.4-6.7 for $\tau \to \mu\gamma\nu\bar{\nu}$ and 6.9-6.12 for $\tau \to e\gamma\nu\bar{\nu}$.

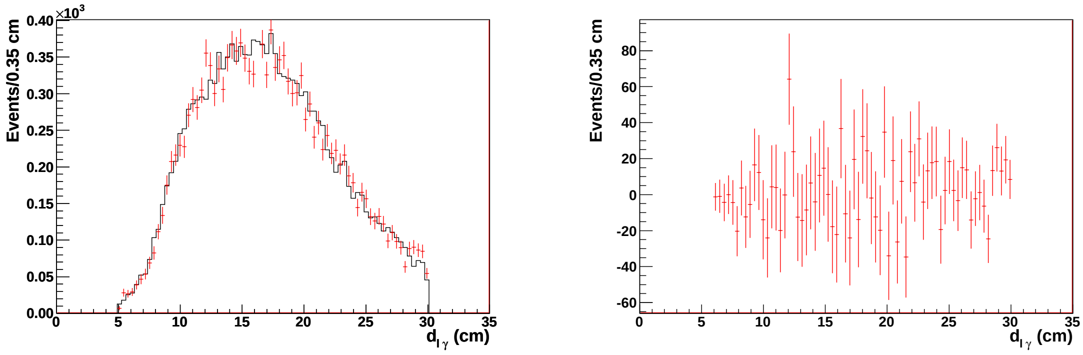

Figure 6.4: Distance between lepton and photon in the EMC (left) and residuals (right) for radiative τ decay into a muon after final selection and background subtraction. The red dots are data while the green bars are $\tau \to \mu\gamma\nu\bar{\nu}$ decays. A Kolmogorov-Smirnov hypothesis test has been performed giving an agreement probability of $P = 0.5827$.

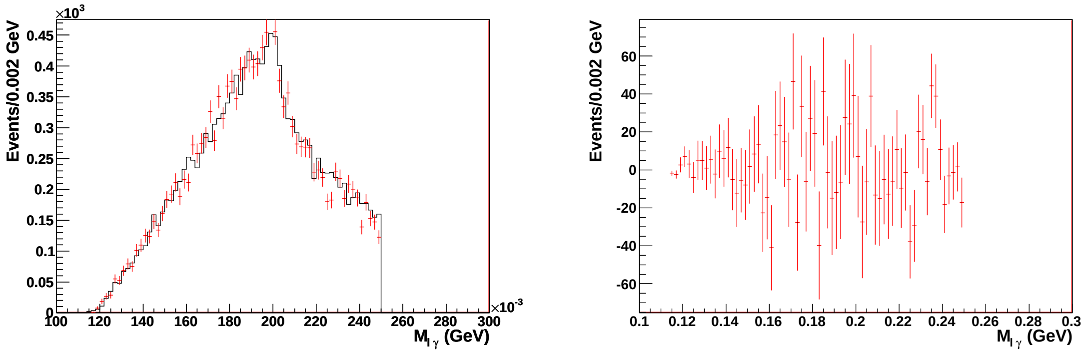

Figure 6.5: Invariant mass (left) and residuals (right) for radiative τ decay into a muon after final selection and background subtraction. The red dots are data while the green bars are $\tau \to \mu\gamma\nu\bar{\nu}$ decays. A Kolmogorov-Smirnov hypothesis test has been performed giving an agreement probability of $P = 0.0981$.

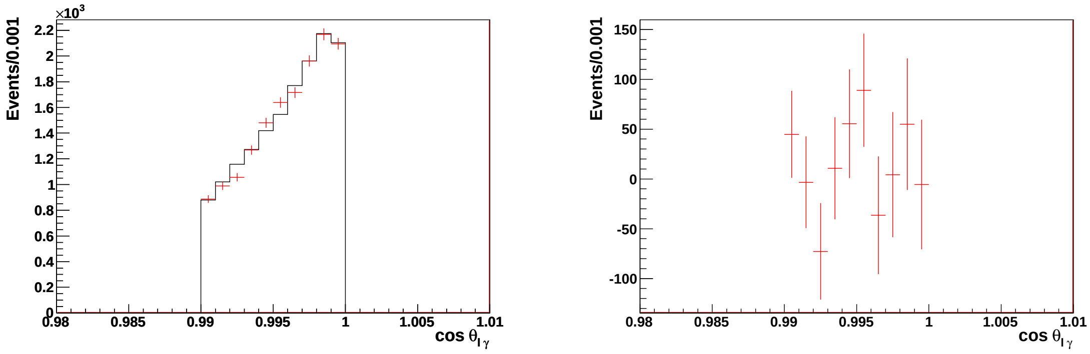

Figure 6.6: Angle between lepton candidate and photon in the CM frame (left) and residuals (right) for radiative τ decay into a muon after final selection and background subtraction. The red dots are data while the green bars are $\tau \to \mu\gamma\nu\bar{\nu}$ decays. A Kolmogorov-Smirnov hypothesis test has been performed giving an agreement probability of $P = 0.2842$.

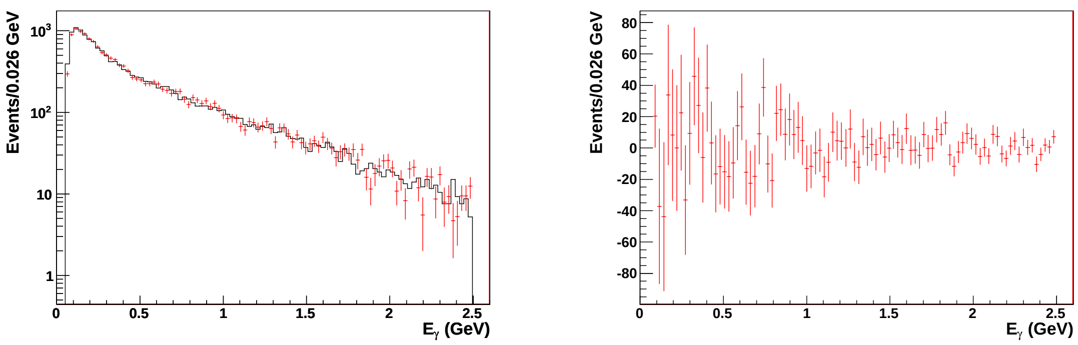

Figure 6.7: Photon energy on the CM frame (left) and residuals (right) for radiative τ decay into a muon after final selection and background subtraction. The red dots are data while the green bars are $\tau \to \mu\gamma\nu\bar{\nu}$ decays. A Kolmogorov-Smirnov hypothesis test has been performed giving an agreement probability of $P = 0.0625$.

6.2.2 $\tau \to e\gamma\nu\bar{\nu}$

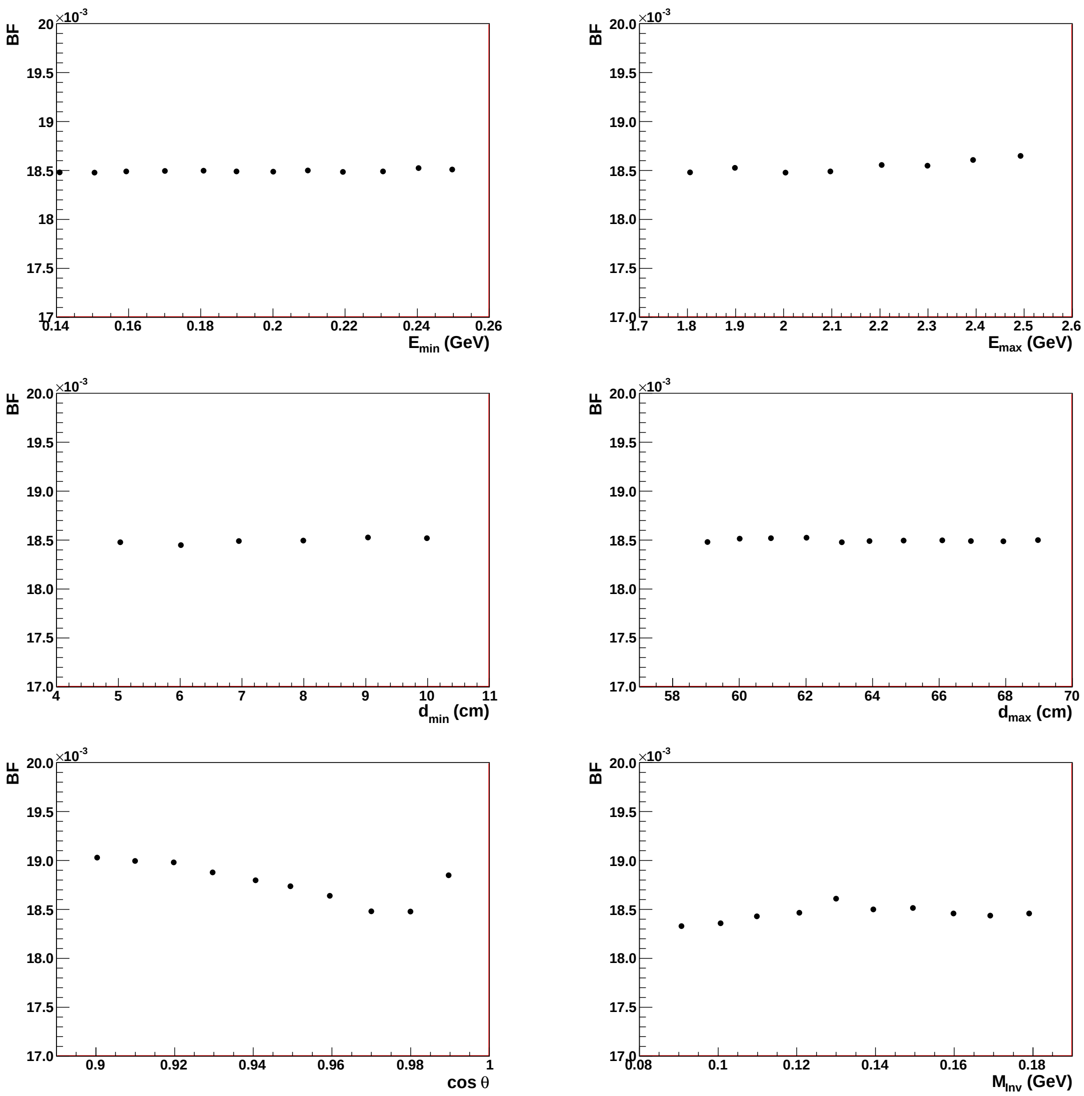

Figure 6.8: Branching fraction as function of selection criteria for radiative τ decay into an electron. From top to bottom: for the minimum (left) and maximum (right) energy of the photon in the CM frame, for the minimum (left) and maximum (right) distance between the neutral cluster and the track on the inner EMC wall and for the cosine of the angle between track and photon (left) in the CM and invariant mass (right) of the lepton-photon system. All selection criteria except the plotted one are set to their nominal value.

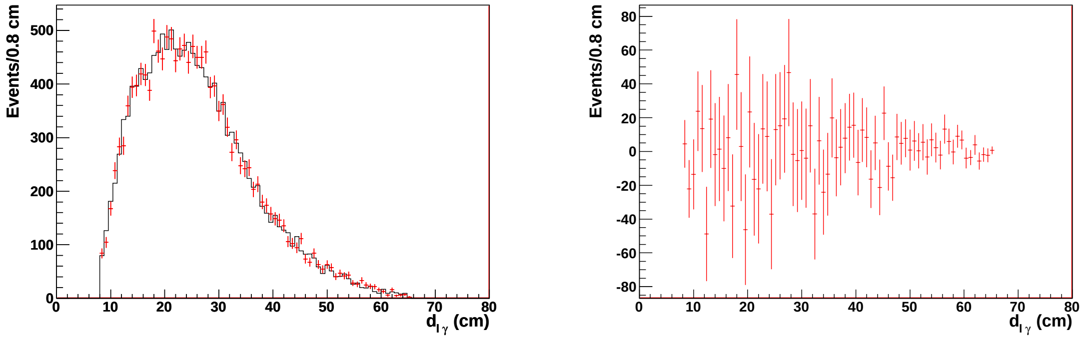

Figure 6.9: Distance between lepton and photon in the EMC (left) and residuals (right) for radiative τ decay into an electron after final selection and background subtraction. The red dots are data while the green bars are $\tau \to e\gamma\nu\bar{\nu}$ decays. A Kolmogorov-Smirnov hypothesis test has been performed giving an agreement probability of $P = 0.6356$.

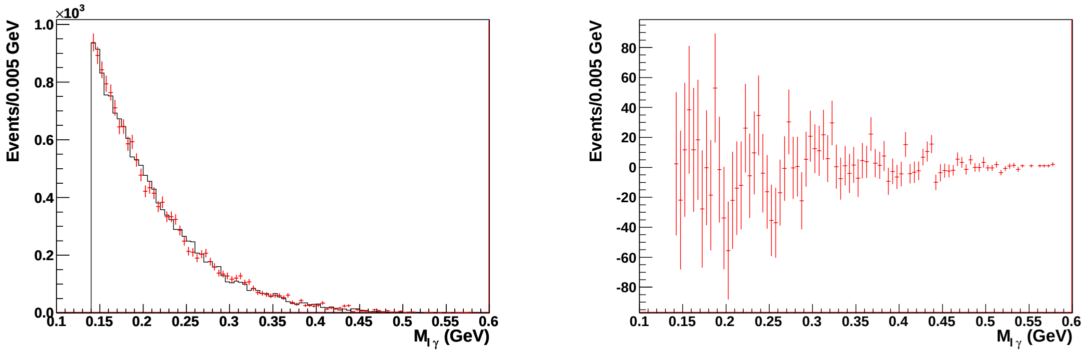

Figure 6.10: Invariant mass (left) and residuals (right) for radiative τ decay into an electron after final selection and background subtraction. The red dots are data while the green bars are $\tau \to e\gamma\nu\bar{\nu}$ decays. A Kolmogorov-Smirnov hypothesis test has been performed giving an agreement probability of $P = 0.2763$.

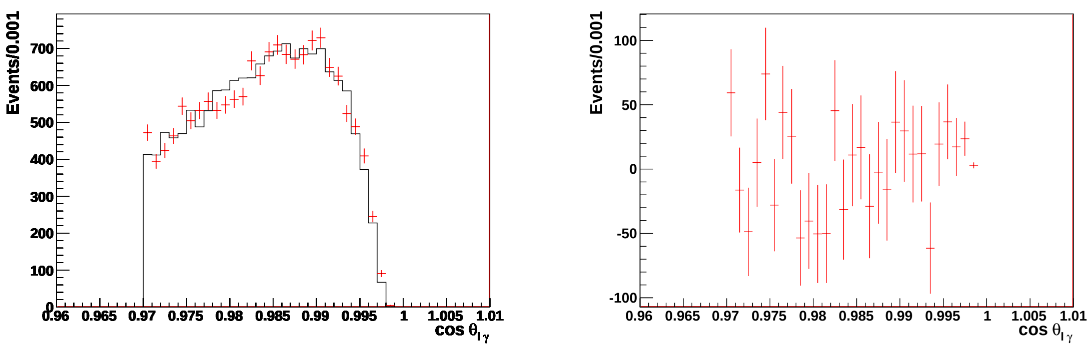

Figure 6.11: Angle between lepton candidate and photon in the CM frame (left) and residuals (right) for radiative τ decay into an electron after final selection and background subtraction. The red dots are data while the green bars are $\tau \to e\gamma\nu\bar{\nu}$ decays. A Kolmogorov-Smirnov hypothesis test has been performed giving an agreement probability of $P = 0.8985$.

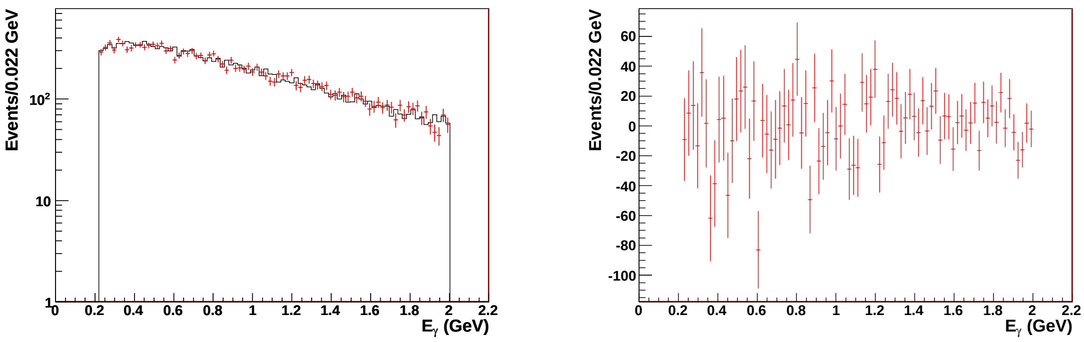

Figure 6.12: Photon energy on the CM frame (left) and residuals (right) for radiative τ decay into an electron after final selection and background subtraction. The red dots are data while the green bars are $\tau \to e\gamma\nu\bar{\nu}$ decays. A Kolmogorov-Smirnov hypothesis test has been performed giving an agreement probability of $P = 0.1187$.

6.3 The anomalous magnetic moment of the τ

Referring back to equation 1.29 the spin averaged branching fraction for $\tau \to l\gamma\nu\bar{\nu}$ decays can be written as

$$\frac{d^3}{dxdcdy} = \frac{\alpha G_F^2 m_\tau^5}{(4\pi)^6} \frac{8\pi^2 x\beta}{1+\delta_W(m_\mu, m_e)} G(x,y,c). \tag{6.4}$$

If include the contribution due to $\tilde{a}_\tau$ introduced in 1.38 the function $G(x,y,c)$ has to be substitued with

$$G(x,y,c) \longrightarrow G(x,y,c) + Re(\tilde{a}_\tau)G_a(x,y,c) + m_\tau Im(\tilde{d}_\tau)G_d(x,y,c). \tag{6.5}$$

The explicit expression of the functions $G(x,y,c)$ (at NLO) and $G_a(x,y,c)$ are given in the appendix A, and bidimensional distribution in the $\cos\theta_{l\gamma}$ versus $2E_l^+/m_\tau$ is shown in fig. 6.13. It can be clearly seen that the most sensitive region to the effect of $\tilde{a}_\tau$ is the region in which the lepton and the photon are emitted back to back in the τ rest frame. However due to the selection strategy that has been used for background reduction this analysis is not sensitive to photons emitted in opposite direction to the outgoing lepton. This an clearly be seen in figures 6.14-6.15 where we show the number of events as function of the angle between outgoing lepton-photon pair in the τ rest frame after all selection criteria have been applied.

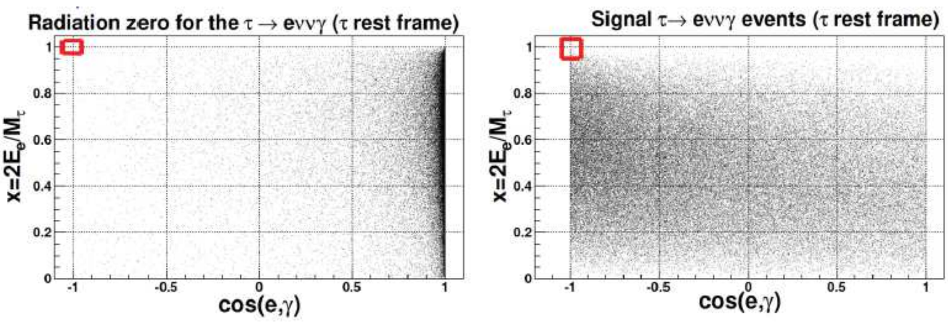

Figure 6.13: Distribution of $x = 2E_l/m_\tau$ versus $\cos\theta_{l\gamma}$ in the τ rest frame for $G(x,y,c)$ (at NLO) and $G_a(x,y,c)$ as defined in A. Figure taken from [16].

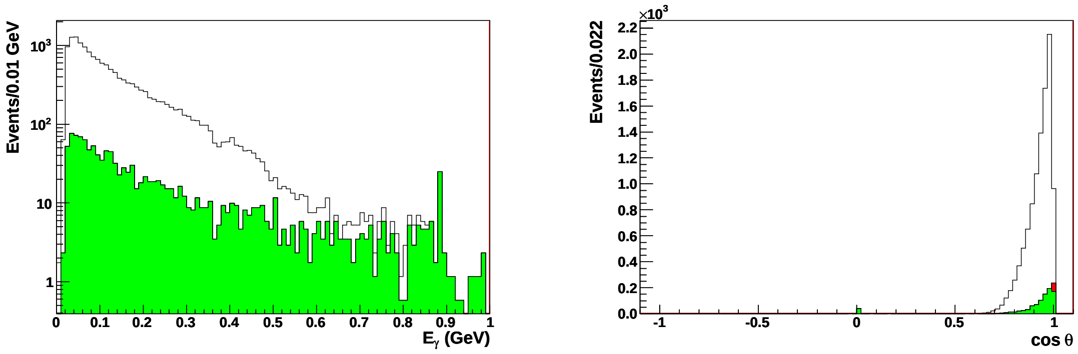

Figure 6.14: Energy spectrum of the candidate signal photon in the τ rest frame frame for $\tau \to \mu\gamma\nu\bar{\nu}$ (left) and $\tau \to e\gamma\nu\bar{\nu}$ (right) after final selection. The white bars are generic (non signal) τ MC decays while the green bars are $\tau \to l\gamma\nu\bar{\nu}$ decays.

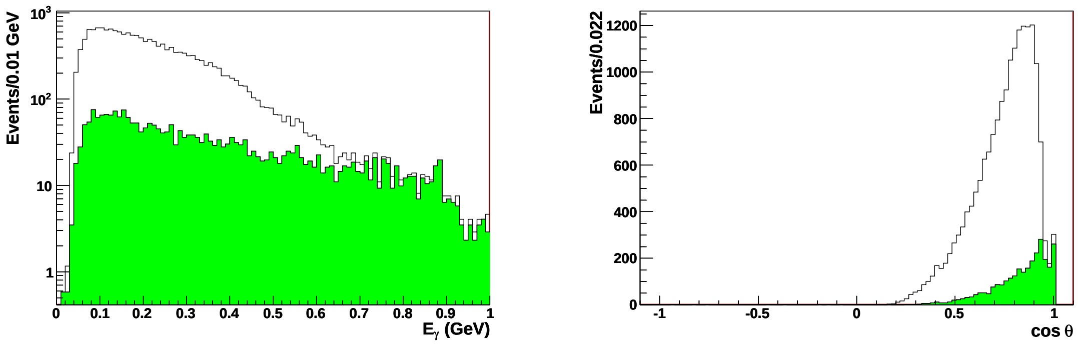

Figure 6.15: Energy spectrum of the candidate signal photon in the τ rest frame frame for $\tau \to e\gamma\nu\bar{\nu}$ (left) and $\tau \to e\gamma\nu\bar{\nu}$ (right) after final selection. The white bars are generic (non signal) τ MC decays while the green bars are $\tau \to l\gamma\nu\bar{\nu}$ decays.

Conclusion

We made a measurement of the branching fractions of the radiative leptonic τ decays $\tau \to l\gamma\nu\bar{\nu}$, $l = e, \mu$ decays for a minimum photon energy of 10 MeV in the τ rest frame using the full dataset of e^+e^- collisions collected by *BABAR* at the center-of-mass energy of the $\Upsilon(4S)$ resonance.

The data sample of $430\,\mathrm{fb}^{-1}$ was recorded by *BABAR* experiment at the PEP-II storage ring in the period between from Winter 1999 and Summer 2006. The high production cross-section of 0.919 nb^-1 allowed to record one of the largest collections of $e^+e^- \to \tau^+\tau^-$ ever produced.

The *BABAR* detector, originally designed for a physics program focusing mostly on CP violation study in the B meson system, due to its large polar and azimuthal angle coverage, the performances of tracking and PID systems, allowed to reach a good background rejection, reduce systematic contributions with increased statistics with respect to previous measurements.

The large MC statistics allowed us to study the background contributions and the signal efficiency for each channel, providing statistically significant samples for the evaluation of the background contributions. Thanks to a good understanding of the detector most discrepancies between data and MC have been corrected. Some mismatches between data and MC remained, in these cases studies were performed to evaluate systematic errors introduced by either non-simulated physics or detector effects.

After the final selection we find $\mathcal{B}(\tau \to \mu\gamma\nu\bar{\nu})(E^*_\gamma > 10\mathrm{MeV}) = (3.69 \pm 0.03 \pm 0.11) \times 10^{-3}$ and $\mathcal{B}(\tau \to e\gamma\nu\bar{\nu})(E^*_\gamma > 10\mathrm{MeV}) = (1.847 \pm 0.015 \pm 0.053) \times 10^{-2}$ where the first error is statistical and the second is systematic. These results represent an improvement of about a factor of three for both channels with respect to the previous experimental bounds [1], reducing both statistic and systematic contributions for both channels.

Our results are in agreement with the SM values at tree level, $\mathcal{B}(\tau \to \mu\gamma\nu\bar{\nu})(E^*_\gamma > 10\mathrm{MeV}) = 3.67 \times 10^{-3}$ and $\mathcal{B}(\tau \to e\gamma\nu\bar{\nu})(E^*_\gamma > 10\mathrm{MeV}) = 1.84 \times 10^{-2}$, as calculated in [6] including W-boson correction.

Our results are also in agreement with previous measurements and, in particular, with the measurement reported by CLEO [1] which, currently, is the only measurement quoted by the particle data group (PDG) [15].

There seems to be, however, a discrepancy between the measurement and the theoretical prediction including higher order QED radiative corrections. We would like to stress anyway that the theoretical values which have been reported have not yet been published and hence they may undergo a further review process.

In any case a further experimental check from the Belle or from the upcoming Belle2 experiments as well as an independent theoretical calculation would be highly desiderable.

Our analysis has also shown that the selection procedure which has been used is not suitable to set bounds on the anomalous magnetic moment of the τ at B-factories; the efficiency in the most sensible region to a_τ is close to zero, and, even if we are able to reconstruct the τ rest frame the measurement of such tiny effects with a better sensitivity than current experimental bounds would require the high statistics which will be provided only by future super-B-factories.

Appendix A

Analytic expression of the branching fraction

The differential decay rate for $\tau \to l\nu\bar{\nu}\gamma$ is given by

$$\frac{d^6_{LO}}{dxdyd\Omega_l d\Omega_\gamma} = \frac{\alpha G_F^2 m_\tau^5}{(4\pi)^8} \frac{x\beta}{1+\delta W(m_\mu, m_e)} \tag{A.1}$$
$$[G(x,y,z) + x\beta\hat{n}\cdot\hat{p}_l J(x,y,z) + y\hat{n}\cdot\hat{p}_\gamma K(x,y,z) + xy\beta\hat{p}_l\cdot(\hat{p}_{\gamma\times\hat{n})L(x,y,z)}]$$

with $r = m_l/m_\tau$, $\beta = \sqrt{1-4r^2/x^2}$, $z = xy(1-c\beta)$ and where $\hat{n}$ is the unit vector in the direction of the tau polarization. The functions G, J and K get a tree-level, a one-loop, a W-propagator, an $\tilde{a}_\tau$ and a $\tilde{d}_\tau$ contribution, while L is generated only by the effective operators. Their expressions are

$$G(x,y,z) = G_{LO} + \frac{\alpha}{\pi}G_{NLO} + r_W^2 G_W + Re(\tilde{a}_\tau)G_a + Im(\tilde{d}_\tau)G_d \tag{A.2}$$
$$J(x,y,z) = J_{LO} + \frac{\alpha}{\pi}J_{NLO} + r_W^2 J_W + Re(\tilde{a}_\tau)J_a + Im(\tilde{d}_\tau)J_d \tag{A.3}$$
$$K(x,y,z) = K_{LO} + \frac{\alpha}{\pi}K_{NLO} + r_W^2 K_W + Re(\tilde{a}_\tau)K_a + Im(\tilde{d}_\tau)K_d \tag{A.4}$$
$$L(x,y,z) = Re(\tilde{a}_\tau)L_a + Im(\tilde{d}_\tau)L_d \tag{A.5}$$

with $r_W = m_\tau/M_W$. Higher orders terms in r_W, $\tilde{a}_\tau$ and $\tilde{d}_\tau$ can be neglected. The above functions take the following form

$$\begin{aligned}
G_{LO} = -&\frac{64\pi^2}{3y^2z^2}[r^4(6xy^2+6y^3-6y^2z-8y^2)+\\
&+r^2(-4x^2y^2-6x^2yz-8xy^3+2xy^2z+6xy^2+6xyz^2+8xyz+\\
&+6xz^2-4y^4+5y^3z+6y^3-2y^2z^2-6y^2z-3yz^3+6yz^2-6z^3-8z^2)+\\
&+4x^3yz+8x^2y^2z-8x^2yz^2-6x^2yz-4x^2z^2+6xy^3z-8xy^2z^2-6xy^2z+6xyz^3-\\
&-2xyz^2+8xz^3+6xz^2+2y^4z-2y^3z^2-3y^3z+2y^2z^3-2y^2z^2-\\
&-2yz^4+5yz^3+6yz^2-4z^4-6z^3]
\end{aligned} \tag{A.6}$$

$$J_{LO} = -\frac{64\pi^2}{3y^2z^2}\{6r^4y^2 + r^2[y^2(-4x + z + 2) + 3yz(z - 2x) - 4y^3 + 6z^2] + \\ + z[4x^2y + x(6y^2 - 2y(3z + 1) - 4z) + 2y^3 - y^2(4z + 1) + yz(2z - 3) + 2z(2z + 1)]\} \tag{A.7}$$

$$K_{LO} = -\frac{64\pi^2}{3y^2z^2}\{6r^4y(y - z) + r^2[y^2(-4x + 5z + 2) + yz(x - 2(z + 1)) + 3z^2(x - z) \\ - 4y^3] - z[-2x^2(y - z) + x(-4y^2 + 4yz + y - z(4z + 1)) - \\ - 2y^3 + y^2(2z + 1) - 2y(z - 1)z + z^2(2z + 1)]\} \tag{A.8}$$

$$G_a = \frac{64\pi^2}{3yz}[r^2(y^2 - zy + 3z^2) - (x + y - z - 1)z(y + 2z)] \tag{A.9}$$

$$G_d = -\frac{128\pi^2}{3y^2z}[6y^2r^4 + (-3y^3 + (-4x + z + 2)y^2 + 3z(z - 2x)y + 6z^2)r^2 + \\ + z(y^3 - (3z + 1)y^2 + 4x^2y + 2(z - 1)zy + 2z(2z + 1) + x(5y^2 - 2(3z + 1)y - 4z))] \tag{A.10}$$

$$J_a = -\frac{64\pi^2}{3yz} \times [-2y^3 + (3r^2 + 2z + 2)y^2 \\ - 2x^2y + 3zy - 2z(3r^2 + 2z + 1) + x(3yr^2 - 4y2 + y + 2yz + 4z)] \tag{A.11}$$

$$J_d = \frac{128\pi^2}{3z}[(-3x - 3y + 4)r^2 + 2x^2 + 2y^2 - 2y + x(4y - 2z - 3) - 2yz + z] \tag{A.12}$$

$$K_a = \frac{64\pi^2}{3y^2z}[-12yr^4 + (3(x + 2)y^2 + (3x^2 + 8x - 8z - 4)y - 6z^2)r^2 - \\ - 2x^3y + x^2y(-4y + 2z + 1) - 2z(-y^2 - zy + y + 2z^2 + z) + \\ + x(-2y^3 + 2(z + 1)y^2 + zy + 4z^2)] \tag{A.13}$$

$$K_d = \frac{128\pi^2}{3y^2z}[-2yx^3 + (-4y^2 + (2z + 3)y + 4z)x^2 + (-2y^3 + 2(z + 1)y^2 + \\ + 5zy - 2z(4z + 3))x + r^2(3yx^2 + 3y^2x - 4yx - 6zx + 2y^2 + 6z^2 - 8yz + 8z) + \\ + 2z(y^2 - (3z + 1)y + z(2z + 3)] \tag{A.14}$$

$$L_a = -\frac{32\pi^2}{3yz}[(-3x-3y+4)r^2+2x^2+2y^2?-2y+x(4y-2z-3)-2yz+z] \quad \text{(A.15)}$$

$$\begin{aligned} L_d = \frac{64\pi^2}{3y^2z}&[2y^3(-3r^2+2z+2)y^2+2x^2y-3zy+2z(3r^2+2z+1)+ \\ &+x(4y^2-(3r^2+2z+1)y-4z] \end{aligned} \quad \text{(A.16)}$$

$$\begin{aligned} G_W = \frac{64\pi^2}{3y^2z^2}&[4r^6y^2-2r^4(2x^2y^2+4xy^3-4xy^2z-2xy^2+2xyz+2y^4-7y^3z-2y^3+ \\ &+2y^2z^2+2y^2z-2y^2-2z^2)+r^2(2x^3y^2+4x^3yz+6x^2y^3+2x^2y^2z-4x^2y^2- \\ &-8x^2yz^2-4x^2yz-4x^2z^2+6xy^4-12xy^3z-8xy^3-8xy^2z^2+4xy^2z+6xyz^3-4xyz^2- \\ &-4xyz+8xz^3+4xz^2+2y^5-9y^4z-4y^4+4y^3z^2+12y^3z+5y^2z^3-4y^2z^2-2yz^4+ \\ &+12yz^3+4yz^2-4z^4-4z^3+4z^2)-z(2x^4y+6x^3y^2-6x^3yz-4x^3y-2x^3z+7x^2y^3- \\ &-6xy^3-16x^2y^2z-8x^2y^2+7x^2yz^2+2x^2yz+6x^2z^2+4x^2z+4xy^4-14xy^3z+ \\ &14xy^2z^2+8xy^2z-4xyz^3+12xyz^2+8xyz-6xz^3-8xz^2+y^5-4y^4z-2y^4+6y^3z^2+ \\ &+5y^3z-4y^2z^3+4y^2z^2+4y^2z+yz^4-9yz^3-14yz^2+2z^4+4z^3)] \end{aligned} \quad \text{(A.17)}$$

$$\begin{aligned} J_W = \frac{32\pi^2}{3y^2z^2}&[-8r^4y^2(x+y-z)+r^2(4x^2y^2+8x^2yz+8xy^3+4xy^2z-12xyz^2- \\ &-8xz^2+4y^4-5y^3z-8y^2z^2+4yz^3-8yz^2+8z^3)+z(-4x^3y-10x^2y^2+ \\ &+10x^2yz+4x^2z-8xy^3+21xy^2z-8xyz^2+8xyz-8xz^2-y^4+10y^3z-y^3- \\ &-11y^2z^2+2y^2z+2yz^3-10yz^2+4z^3)] \end{aligned} \quad \text{(A.18)}$$

$$\begin{aligned} K_W = \frac{32\pi^2}{3y^2z^2}&[-4r^4y-2xy-2xz+2y^2-7yz+2z^2)+r^2(4x^2y^2-4x^2z^2+8xy^3- \\ &-19xy^2z-8xyz^2+8xz^3+4y^4-18y^3z+8y^2z^2+8y^2z+10yz^3+6yz^2-4z^4)- \\ &-z(2x^3y-2x^3z+6x^2y^2-11x^2yz+6x^2z^2+7xy^3-18xy^2z-xy^2+17xyz^2+ \\ &+2xyz-6xz^3+2y^4-8y^3z+12y^2z^2-8yz^3-2yz+2z^4)] \end{aligned} \quad \text{(A.19)}$$

Appendix B

The anomalous magnetic moment of the τ lepton

B.1 The anomalous magnetic moment

The Dirac equation predicts a magnetic moment for the τ given by

$$\vec{M} = g_\tau \frac{e}{2m_\tau} \vec{S} \tag{B.1}$$

where $g_\tau = 2$. The previous equation can be assumed valid also at loop level, but, because of quantum loop corrections, the relation $g_\tau = 2$ no longer holds, and one has to define the magnetic moment anomaly given by

$$a_\tau = \frac{g_\tau - 2}{2}. \tag{B.2}$$

The anomaly defined by B.2, in turn, can be written as sum of different terms which correspond to the different interactions at work at loop level, namely

$$a_\tau = a_\tau^{QED} + a_\tau^{EW} + a_\tau^{HAD} \tag{B.3}$$

where the first term is pure QED while the others are due to weak and strong corrections. At one-loop level the three different terms are represented in fig. B.1.

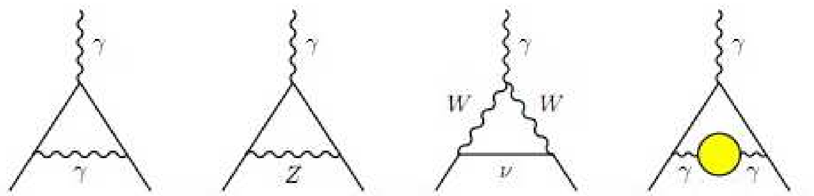

Figure B.1: One loop contributions to the anomalous magnetic moment. From left to right: QED, EW, neutral and charged, and hadronic graph.

Equation B.3 says us that we expect the magnetic moment anomaly to depend on the flavor, i.e., on the mass, of the involved leptons because this dependence is inherited from the involved interactions. More quantitatively, recent calculations [5] show that higher order QED contributions are at order of 1% of the one loop result of Schwinger, while the weak and hadronic graphs give contributions of the order of 0.04% and 0.001% respectively, which summed together give

$$a_\tau^{SM} = 1177.21(5) \times 10^{-6}. \tag{B.4}$$

Moreover, as will be explained better later, we stress that, in general, what one actually measures at an e^+e^- collider is not the parameter defined in B.2 but instead the magnetic moment form factor F_2 which depends on the CM energy of the e^+e^- system. In fact the magnetic moment is defined with all three particles which enter in the graph of B.1 on-shell, while in what we actually measure this is not respected.

B.2 a_τ in the Standard Model

In the following we review the main contributions to a_τ in the standard model.

B.2.1 QED contribution

The QED part, a_{QED}, arises from the subset of SM diagrams containing only leptons and photons. This dimensionless quantity can be cast in the general form

$$a_{QED} = A1 + A2(\frac{m_\tau}{m_e}) + A2(\frac{m_\tau}{m_\mu}) + A3(\frac{m_\tau}{m_e}, \frac{m_\tau}{m_\mu}) \tag{B.5}$$

where m_e m_μ, and m_τ are the electron, muon, and τ mass. The first term, arising from diagrams containing only photons and τ, is mass and flavour independent, while the other terms are functions of the mass ratios, generated by graphs including also electrons and muons. Each function can be expanded as power series of α and computed order by order:

$$A_i = (\frac{\alpha}{\pi})A_i^{(2)} + (\frac{\alpha}{\pi})^2 A_i^{(4)} + (\frac{\alpha}{\pi})^3 A_i^{(6)} + ... \tag{B.6}$$

At one loop only one diagram contributes, which gives the well known contribution to

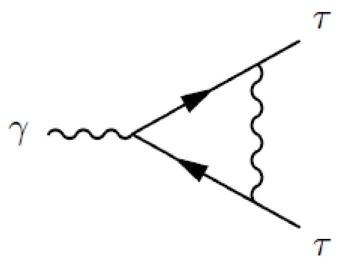

Figure B.2: One loop QED contribution to the anomalous magnetic moment.

a_τ

$$a_1^{QED} = \frac{\alpha}{2\pi} \tag{B.7}$$

already calculated by Schwinger; at two loops seven different diagrams contribute both

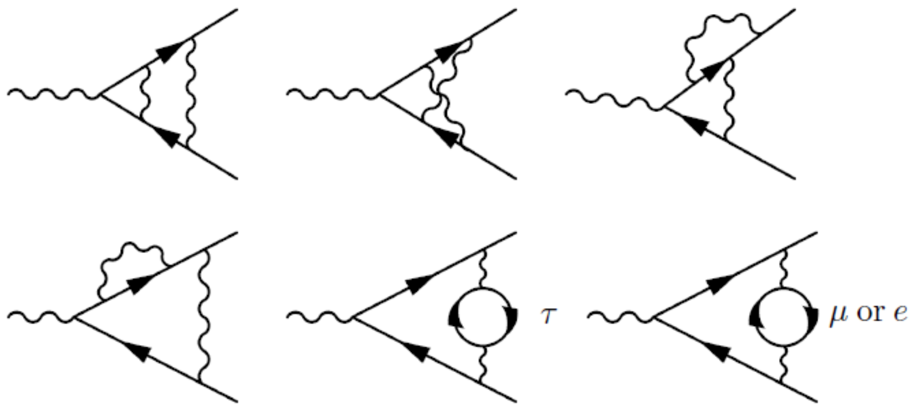

Figure B.3: Two loop QED contribution to the anomalous magnetic moment.

mass dependent ans mass independent terms; the mass independent part gives

$$A_2^{(2)} = \frac{197}{144} + \frac{\pi^2}{12} + \frac{3}{4}\zeta(3) - \frac{\pi^2}{2}\ln 2 \tag{B.8}$$

where ζ is the Riemann function, while the mass dependent part

$$A_2^{(4)}\frac{1}{x} = -\frac{25}{36} + \frac{\ln x}{3} + x^2(4 + 3\ln x) + \frac{x}{2}(1 - 5x^2)\times$$
$$[\frac{\pi^2}{2} - \ln x \ln(\frac{1-x}{1+x}) - Li_2(x) + Li_2(-x)] + x^4[\frac{\pi^2}{3} - 2\ln x \ln(\frac{1}{x} - x) - Li_2(x^2)] \tag{B.9}$$

where we used the dilogarithmic function

$$Li_2(z) = -\int_0^z \frac{\ln(1-t)}{t}dt \tag{B.10}$$

At three loop order more than 100 diagrams contribute, including light by light graphs and double vacuum polarization.

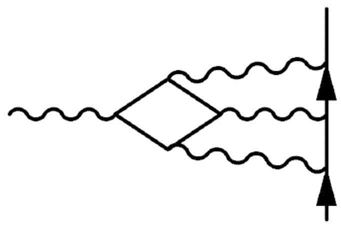

Figure B.4: Fourth order light by light contribution to the anomalous magnetic moment.

A summary of the numerical results for 2 and 3 loop contributions is given in table B.1.

We stress that up to this order the most important contribution to the total error is given by the uncertainty on the mass values m_e, m_μ and m_τ.

$A_1^{(4)}$	$-0.328478..$
$A_2^{(4)}(m_\tau/m_e)$	2.024284(55)
$A_2^{(4)}(m_\tau/m_\mu)$	0.361652(38)
$A_1^{(6)}$	1.181241456..
$A_2^{(4)}(m_\tau/m_e)$	46.3921(15)
$A_2^{(4)}(m_\tau/m_\mu)$	7.01021(76)
$A_2^{(4)}(((m_\tau/m_e), m_\tau/m_\mu))$	3.34797(41)

Table B.1: Summary of two and three loop contributions to a_{tau}. The number in parentheses is the theoretical uncertainty.

The total QED contribution to a_τ up to 4th order a_{QED} is

$$a_{QED} = 117324(2) \times 10^{-8} \tag{B.11}$$

The error on a_{QED} is the uncertainty assigned to uncalculated four-loop contributions. Compared to this one, the errors due to the uncertainties of the $\mathcal{O}(\alpha^2)$ and $\mathcal{O}(\alpha^3)$ terms are negligible.

B.2.2 Electroweak contribution

With respect to the QED one-loop term, the electroweak correction to a_W is suppressed by $(m_\tau/M_W)^2 \sim 4.8 \times 10^{-4}$, where M_W is the mass of W boson. The EW contribution is therefore of the same order of magnitude as the three-loop QED one.

A detailed calculation gives

$$a_W one - loop) = 55.2(1) \times 10^{-8} \tag{B.12}$$

The two-loop correction to a_W involves 1678 diagrams. Naively one would expect the two-loop EW terms to be of order $(\alpha/\pi)a_W$ instead they contribute quite substantially because of the appearance of terms enhanced by a factor of $\log(M_{W.Z}/m_f)$, where m_f is a fermion mass scale much smaller than M_W. The two-loop EW contribution is

$$a_W(two - loop) = -7.74 \times 10^{-8}. \tag{B.13}$$

The three-loop EW corrections to a_τ were determined to be extremely small using a renormalization-group analysis. In the end the total EW contribution is given by

$$a_W(two - loop) = 47.4(5) \times 10^{-8}. \tag{B.14}$$

B.2.3 QCD

B.2.4 Summary

Now we can add up all the discussed terms to derive the SM value of a_τ

$$a_{SM} = a_{QED} + a_W + a_{HAD} \tag{B.15}$$

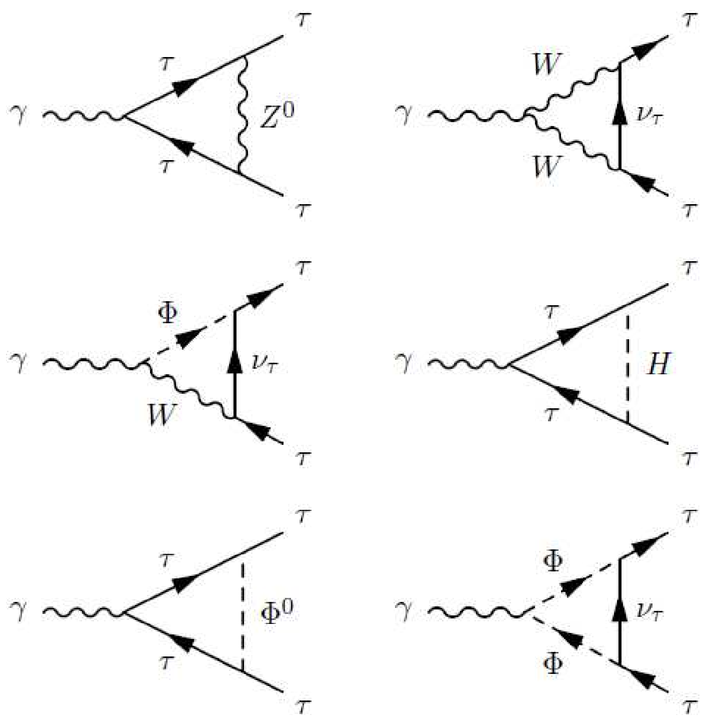

Figure B.5: One-loop electroweak contributions to the anomalous magnetic moment. The diagram with a W and a Goldstone boson must be counted twice.

where

$$a_{QED} = 117324(2) \times 10^{-8} \tag{B.16}$$
$$a_W = 47.4(5) \times 10^{-8} \tag{B.17}$$
$$a_{HAD} = 350.1(4.8) \times 10^{-8} \tag{B.18}$$

giving

$$a_{SM} = 117721(5) \times 10^{-8}. \tag{B.19}$$

New Physics associated with a scale Λ is expected to modify the SM prediction of the anomalous magnetic moment of a lepton l of mass m_l by a contribution of order m_l^2/Λ^2. Therefore, given that $(m_\tau = m_\mu)^2 \sim 283$, a_τ is much more sensitive than the one of the muon to NP effects making its measurement an interesting laboratory to unveil or constrain NP effects. Another interesting feature can be observed comparing the magnitude of EW and hadronic contributions to the muon and τ lepton g-2. The EW contribution to the τ magnetic moment is only a factor 7 smaller than the hadronic one, compared to a factor 45 in the case of the muon.

Appendix C

Radiation zeros in $\tau \to l\gamma\nu\bar{\nu}$ decays

The idea to extract the anomalous magnetic moment of the τ from radiative decays $\tau \to l\gamma\nu\bar{\nu}$ was first expressed in an older paper by Laursen *et al.* [12]. The authors suggest to take advantage of the "radiotion zero", i.e. from the fact that the amplitude for certain processes involving one real photon vanishes in a certain region of phase space called the null zone, provided that g =2 for all charged particles with spin.

For $\tau \to l\gamma\nu\bar{\nu}$ the null zone is is obtained for $l\gamma$ back-to back in the τ rest frame and and maximum energy for the outgoing lepton $E_l = m_\tau/2$.

The authors calculate the differential decay rate as

$$\frac{d^3\Gamma}{dxdyd\Omega} = \frac{\alpha}{4\pi}\Gamma_{tot}H \tag{C.1}$$

where

$$x = \frac{2E_l}{m_\tau} \tag{C.2}$$

$$y = \frac{2E_\gamma}{m_\tau} \tag{C.3}$$

Γ_{tot} is the integrated decay rate for $\tau \to l\nu\bar{\nu}$ and H is given by

$$H = A + A'\frac{a}{2} + +A''(\frac{a}{2})^2. \tag{C.4}$$

The functions A, A', A'' are given by

$$\begin{aligned} yA =& \frac{8}{\Delta}[y^2(32y) + 6xy(1y) + 2x^2(34y)4x^3] + 8[2x^3(1+2y)xy(3yy^2)x^2(3y4y^2)] \\ &+ 2\Delta[x^2y^2(65y2y^2)2x^3y(4+3y)] + 2\Delta^2x^3y^2(2+y) \end{aligned} \tag{C.5}$$

$$\frac{A'}{4} = x^3y^2\Delta^2 + x^2y\Delta(22xy) + 2xy(1xy) \tag{C.6}$$

$$\frac{A''}{2} = x^2y^2\Delta(2x+y2) + 2x^2y(32y2x) \tag{C.7}$$

with

$$\Delta = 1 - \cos\theta. \tag{C.8}$$

For $\Delta = 2$ one gets

$$A(\Delta = 2) = 4(1x)y[2x^2(1y) + (3x2y)] \tag{C.9}$$
$$A'(\Delta = 2) = 8xy(1x)(1y)(1 + 2x) \tag{C.10}$$
$$A''(\Delta = 2) = 4x^2y(1y)(32xy) \tag{C.11}$$

and hence, for $x = 1$, the first two terms vanish and a spoils the radiation zero by

$$H(\Delta = 2, x = 1) = y(y1)a^2 > 0. \tag{C.12}$$

Now, if one considers

$$F(x) = \int_0^1 dyH(\Delta = 2) = B(\Delta = 2) + B'(\Delta = 2)(\frac{a}{2}) + B''(\Delta = 2)(\frac{a}{2})^2 \tag{C.13}$$

where

$$B(\Delta = 2) = \frac{2}{3}(1x)(2x^2 3x + 5) \tag{C.14}$$
$$B'(\Delta = 2) = \frac{4}{3}x(1x)(1 + 2x) \tag{C.15}$$
$$B''(\Delta = 2) = 4x^2(-\frac{x}{3} + \frac{5}{12}) \tag{C.16}$$

one gets for the differential decay rate for back-to-back lepton-photon events, integrated over all photon energies

$$\frac{d^2\Gamma(\tau \to l\gamma\nu\bar{\nu})}{dx\Omega} = \frac{\alpha}{4\pi}\Gamma_{tot}(\tau \to \nu\bar{\nu})F(x). \tag{C.17}$$

The actual sensitivity to a_τ will depend on integration interval choosen for x and on integrated luminosity.

Bibliography

[1] T. Bergfeld, *et al. Phys.Rev.Lett.* **84**, 830-834, (2000).

[2] G. Alexander *et al.*, *Phys. Lett.* **B388**, 437 (1996).

[3] M. Fael *et al.*, arXiv:1301.5302, (2013).

[4] M. Fael, *Study of the anomalous magnetic moment of the τ lepton via its radiative leptonic decays*, M.Sc. Thesis, University of Padua (2010).

[5] M. Fael, , PhD Thesis, University of Padua (2013).

[6] M. Fael, L. Mercolli and M. Passera, Phys. Rev. D **88** (2013) 9, 093011, arXiv:1310.1081.

[7] A. Sirlin and A. Ferroglia, Rev. Mod. Phys. **85** (2013) 1, arXiv:1210.5296 [hep-ph].

[8] A. Ferroglia, C. Greub, A. Sirlin and Z. Zhang, Phys. Phys. Rev. D **88** (2013), 033012, arXiv:1307.6900 [hep-ph].

[9] A. Ferroglia, *et al.*, Phys.Rev. **D88**, 033012 (2013), 1307.6900.

[10] A. Sirlin, Phys.Rev. **D22**, 971 (1980).

[11] T. Kinoshita and A. Sirlin, Phys.Rev. 113, 1652 (1959).

[12] M. L. Laursen, M. A. Samuel, A. Sen, *Phys. Rev.* **D29**, 2652, (1984).

[13] W. Bernreuther, O. Nachtmann, and P. Overmann, *Phys. Rev.* **D48**, 78, (1993).

[14] G. A. Gonzalez-Sprinberg, A. Santamaria, and J. Vidal, *Nucl.Phys.* **B582**, 3, (2000).

[15] J. Beringer *et al.* (Particle Data Group), *Phys. Rev.* **D86**, 010001 (2012).

[16] M. Passera, TAU2012 conference contribution, 17-21 September 2012, Nagoya, Japan, http://www2.hepl.phys.nagoya-u.ac.jp.

[17] S. Jadach, B.F.L. Ward and Z. Was, *Comput. Phys. Commun.*, **130** (2000).

[18] B.F.L. Ward, S. Jadach, and Z. Was, *Nucl. Phys. Proc. Suppl.*, **116** (2003).

[19] S. Banerjee, B. Pietrzyk, M. Roney, and Z. Was., *Phys. Rev.* **D77**, 054012 (2008).

[20] S. Jadach, Z. Was, R. Decker, and J. H. Kuhn, *Comput. Phys. Commun.*, **76**, 361380, (1993).

[21] P. Golonka *et al.*, *Comput. Phys. Commun.*, **174**, 818835, (2006).

[22] E. Barberio and Z. Was, *Comput. Phys. Commun.*, **79**, 291308, (1994).

[23] D.J. Lange, *Nucl. Instrum. Meth.*, **A462** 152155, (2001).

[24] S. Agostinelli *et al.*, *Nucl. Instrum. Meth.*, **A506**, 250303 (2003).

[25] B. Aubert *et al.* [BABAR Collaboration], *Phys. Rev. Lett.* **95**041802 (2005).

[26] A. Denig *et al.*, *BABAR* Analysis Document **2235**.

[27] M. Allen *et al.*, *BABAR* Analysis Document **870**.

[28] J.P. Lees *et al.*, arXiv:1301.2703v3 (2013).

[29] L. Michel, *Proc. Phys. Soc. London* **A 63**, 514, (1950).

[30] W. Bernreuther, *et al.*, *Phys.Rev.* **D48**, 78 (1993).

[31] G. A. Gonzalez-Sprinberg, *et al.*, *Nucl.Phys.* **B582**, 3, (2000).

[32] G. Passarino, M. Veltman, *Nucl.Phys.* **B160**, 151, (1979).

[33] *BABAR* Collaboration, B. Aubert *et al.*, Nucl. Instrum. Methods Phys. Res., Sect. A **479**, 1 (2002).

[34] S. Banerjee, B. Pietrzyk, J. M. Roney, and Z. Was, Phys. Rev. D **77**, 054012 (2008).

[35] Particle Data Group, Y.-M. Yao *et al.* J. Phys. **G33**, 1 (2006).

[36] S. Jadach, Z. Was, R. Decker, and J. H. Kuhn, Comput. Phys. Commun. **76**, 361 (1993).

[37] E. Barberio and Z. Was, Comput. Phys. Commun. **79**, 291 (1994).

[38] T. Sjostrand, S. Mrenna, and P. Skands, JHEP, 05-026, (2006).

[39] D.J. Lange, Nucl. Instrum. Meth., **A462**, 152-155, (2001).

[40] S. Agostinelli *et al.*, Nucl. Instrum. Methods Phys. Res., Sect. A **506**, 250 (2003).

[41] E. Farhi, *Phys. Rev. Lett.* **39**, 1587 (1977).

[42] E. L. Allwein, R. E. Schapire and Y. Singer J. Machine Learning Res. **1**, 113 (2000).

[43] J. Gaiser *et al.*,Phys. Rev. D, **34**, 711 (1986).

[44] *PEP-II: An Asymmetric B Factory. Conceptual Design Report*, June 1993. SLAC-418, LBL-PUB-5379.

[45] Swagato Banerjee, Bolek Pietrzyk, J. Michael Roney, and Zbigniew Was. *τ and μ pair production cross-sections in electron-positron annihilations at* $\sqrt{s} = 10.58\,\mathrm{GeV}$, Phys. Rev. **D77**:054012, 2008, 0706.3235.

[46] *Results and plans of the PEP-II B Factory*, 2004. Presented at 9th European Particle Accelerator Conference (EPAC 2004), Lucerne, Switzerland, 5-9 Jul 2004.

[47] C. Bozzi *et al.*, *The BABARsilicon vertex tracker*, Nucl. Instrum. Meth. **A435**:2533, 1999.

[48] V. Re *et al.*, *Status and future plans of the BABARsilicon vertex tracker*, Nucl. Instrum. Meth. **A511**:15, 2003.

[49] V. Re *et al.*, *Performance of the BABARsilicon vertex tracker*, Nucl. Instrum. Meth. **A501**:1421, 2003.

[50] G. Sciolla *et al.*, *The BABARdrift chamber*, Nucl. Instrum. Meth., **A419**:310314, 1998.

[51] Michael H. Kelsey, *Performance and aging of the BABARdrift chamber*, Nucl. Instrum. Meth. **A535**:206211, 2004.

[52] I. Adam *et al.*, *Dirc, the internally reflecting ring imaging Čerenkov detector for BABAR*, IEEE Trans. Nucl. Sci. **45**:657664, 1998, hep-ex/9712001.

[53] *Operation of the Čerenkov detector DIRC of BABARat high luminosity*, 2000. Talk given at IEEE Nuclear Science Symposium and Medical Imaging Conference, Lyon, France, 15-20 Oct 2000.

[54] B. Lewandowski. *The BABARelectromagnetic calorimeter*, Nucl. Instrum. Meth., **A494**:303307, 2002.

[55] F. Anulli *et al.*, *The muon and neutral hadron detector for BABAR*, Nucl. Instrum. Meth., **A409**:542546, 1998.

[56] G. Battistoni, E. Iarocci, M.M. Massai, G. Nicoletti, and L. Trasatti, *Operation Of Limited Streamer Tubes*, Nucl. Instr. Meth., **164**:57, 1979.

[57] W. Menges, *The BABARmuon system upgrade*, IEEE Nucl. Sci. Symp. Conf. Rec., **5**:14701474, 2006, physics/0609039.

[58] G.D. Alekseev, N.A. Kalinina, V.V. Karpukhin, D.M. Khazins and V.V. Kruglov, *Investigation of Selfquenching Streamer discharge in a wire chamber*, Nucl. Instrum. Methods Phys. Res., Sect. C **177** (1980) 385.

[59] B. Aubert *et al*, *Improved Limits on the Lepton-Flavor Violating Decays $\tau \to \ell\ell\ell$*, Phys. Rev. Lett. **99**:251803,2007, arXiv:0708.3650v1 [hep-ex].

[60] S. Jadach, B.F.L. Ward, and Z. Was, *The precision Monte Carlo event generator KK for two-fermion final states in e^+e^- collisions*, Comput. Phys. Commun., **130**:260 325, 2000, hep-ph/9912214.

[61] B.F.L. Ward, S. Jadach, and Z. Was, *Precision calculation for $e^+e^- \to 2f$: The KK MC project*, Nucl. Phys. Proc. Suppl., **116**:7377, 2003, hep-ph/0211132.

[62] S. Jadach, Z. Was, R. Decker, and Johann H. Kuhn, *The τ decay library* TAUOLA*: Version 2.4*, Comput. Phys. Commun., **76**:361380, 1993.

[63] Elisabetta Barberio and Zbigniew Was, PHOTOS*: A Universal Monte Carlo for QED radiative corrections. Version 2.0*, Comput. Phys. Commun., **79**:291308, 1994.

[64] P. Golonka *et al.*, Comput. Phys. Commun., **174**:818-835, 2006, hep-ph/0312240.

[65] D.J. Lange, *The EvtGen particle decay simulation package*, Nucl. Instrum. Meth., **A462**:152155, 2001.

[66] Torbjorn Sjostrand, Stephen Mrenna, and Peter Skands, PYTHIA *6.4 physics and manual*, JHEP, **05**:026, 2006, hep-ph/0603175.

[67] S. Agostinelli *et al.*, GEANT4 *: A simulation toolkit*, Nucl. Instrum. Meth., **A506**:250303, 2003.

[68] Pierre Billoir, *Track Fitting With Multiple Scattering: A New Method*, Nucl. Instrum. Meth., **A225**:352366, 1984.

[69] Geoffrey C. Fox and Stephen Wolfram, *Event Shapes in e^+e^- Annihilation*, Nucl. Phys., **B149**:413, 1979.

[70] S. Brandt *et al.*, Phys. Lett. **12**, 57, 1964;
E. Fahri, Phys. Rev. Lett. **39**, 1587, 1977.

[71] Erin Allwein, Robert E. Schapire, Yoram Singer, Pack Kaelbling, *Reducing Multiclass to Binary: A Unifying Approach for Margin Classifiers*, J. Machine Learning Res., **1**, 113, 2000.

[72] T. Brandt, *Likelihood-based Electron Identification*, BABARAnalysis Document #396, 2002.

[73] I. Narsky, *StatPatternRecognition: A C++ Package for Statistical Analysis of High Energy Physics Data*, 2005, arXive:physics/0507143.

[74] J. Neyman, Philosophical Transactions of the Royal Society of London. Series A, Mathematical and Physical Sciences **236**, 333, 1937, ISSN 00804614, URL http://www.jstor.org/stable/91337.